

Synthesis and Physical Properties of 3d, 4d and 5d Transition Metal Compounds

THÈSE N° 7547 (2017)

PRÉSENTÉE LE 10 MARS 2017

À LA FACULTÉ SCIENCES DE BASE

LABORATOIRE DE PHYSIQUE DE LA MATIÈRE COMPLEXE

PROGRAMME DOCTORAL EN PHYSIQUE

ÉCOLE POLYTECHNIQUE FÉDÉRALE DE LAUSANNE

POUR L'OBTENTION DU GRADE DE DOCTEUR ÈS SCIENCES

PAR

Lin YANG

acceptée sur proposition du jury:

Prof. R. Houdré, président du jury
Prof. L. Forró, Prof. H. M. Rønnow, directeurs de thèse
Prof. J. Chang, rapporteur
Prof. K. Conder, rapporteur
Prof. O. V. Yazyev, rapporteur



ÉCOLE POLYTECHNIQUE
FÉDÉRALE DE LAUSANNE

Suisse
2017

To my parents...

Abstract

Recently, there has been considerable interest in studying transition metal oxides which exhibits a very wide variety of structure, electrical and magnetic properties. The unusual properties of transition metal oxides are due to the elements with incomplete d shells in the periodic table, the metal-oxygen bonding varying between nearly ionic to highly covalent or metallic.

In this thesis I study the synthesis and basic physical properties characterization on $3d$, $4d$ and $5d$ transition metal compounds.

Great success has been obtained in $3d$ transition metal compounds, in which the electric states are well localized due to the large on-site Coulomb repulsion U . Most stoichiometric $3d$ transition metal oxides are antiferromagnetic Mott insulators. Among them, low dimensional geometrically frustrated systems, such as $S = 1/2$ Kagome lattice antiferromagnets, are at the forefront of condensed matter research. Recently, high-quality single crystals of Cu_2OSO_4 , which are spin- $1/2$ antiferromagnets with low dimensional magnetism, have been successfully synthesized. The measurements of specific heat, susceptibility and magnetization were performed on this material. We found that the Kagome-like compound Cu_2OSO_4 shows typical signatures for a canted-AFM ground state with a weak ferromagnetic component.

On the other hand, $4d$ transition metal compounds were considered as weakly correlated systems because the electron correlation is expected to be weaker in $4d$ transition metal compounds compared with the $3d$ ones. The $4d$ ones naturally bridge two different regimes of the strongly correlated $3d$ compounds and the $5d$ compounds. Most notably, for instance, it is intriguing that seemingly similar Ca_2RuO_4 and Sr_2RuO_4 display totally different behavior: the former is a Mott insulator while the latter is metallic and becomes superconducting at low temperature. Here we report the synthesis of large single crystals of MoPO_5 , and present their magnetic and thermodynamic properties. We found that the $4d^1$ compound MoPO_5 is orbitally quenched and orders into an antiferromagnet with the moments along c axis. Spin-flop transition is observed which indicates magnetic anisotropy.

$5d$ orbitals are more extended and the Coulomb repulsion U values are expected to be further reduced compared with those of $3d$ and $4d$ transition metal compounds. Thus, insulating behaviors in $5d$ transition metal compounds have been puzzling. A possible reason is the strong spin-orbit coupling. Here we show the ambient-pressure synthesis and physical properties of

a new all-Ir⁶⁺ iridate Ba₈Al₂IrO₁₄ and a novel layered iridate Ba₂₁Ir₉O₄₃. The synthesis, crystal structure, transport, and magnetic properties of them have been reported. Ba₈Al₂IrO₁₄ is a *p*-type band insulator and shows antiferromagnetic couplings but display no order down to 2 K. Ba₂₁Ir₉O₄₃ is an insulator with antiferromagnetic Curie-Weiss behavior, where a magnetic transition is suppressed down to low temperature of 9 K despite the large Curie-Weiss temperature of −90 K. We also performed the pressure-dependent resistivity measurements of the 5*d* compound Ir_{0.95}Pt_{0.05}Te₂ and found that the charge order with $q=(1/5,0,1/5)$ dimer configuration is introduced and the superconductivity undergoes a dimensionality cross-over from 3 dimension to 2 dimension under pressure.

Key words: Iridates, transition metal compounds, spin-orbital coupling, low dimensional magnetism, superconductivity

Résumé

L'intérêt d'étudier les composés de métaux de transition est grandissant. Ces derniers présentent un large spectre de propriétés structurales, électriques et magnétiques. L'origine des propriétés peu communes de ces métaux provient de leur orbitale atomique incomplète, ainsi, la liaison métal-oxygène varie entre presque-ionique à très covalente, voire métallique.

Pendant ma thèse, j'ai fait la synthèse et la caractérisation des oxydes de métal de transition à orbitales $3d$, $4d$ et $5d$.

J'ai réussi à obtenir des métaux de transition à orbitale $3d$ dans lesquelles l'état électronique a été bien localisé grâce à la répulsion de Coulomb (U). La plupart des oxydes de métaux à transition stoichiométriques et à orbitale $3d$ sont des isolants de Mott antiferromagnétiques. Parmi eux, on retrouve des systèmes géométriquement frustrés à basse dimension, comme les aimants antiferromagnétiques à structure de Kagome de $S=1/2$, qui sont en ligne de front dans la recherche en physique de la matière condensée. Récemment, des monocristaux de Cu_2OSO_4 de haute-qualité, qui possèdent un spin- $1/2$ et sont des aimants antiferromagnétiques à une basse dimension magnétique, ont été synthétisés avec succès. De plus, les mesures de chaleur spécifique, susceptibilité et magnétisation ont été effectuées sur ces matériaux. Nous avons trouvé que le composé trihexagonal (dit de Kagome) Cu_2OSO_4 montre des signatures typiques de AFM avec une composante ferromagnétique faible.

D'un autre côté, les composés de métaux à transition à orbitale $4d$ ont été considérés comme des systèmes à large bande faiblement corrélés parce que la corrélation d'électron est suspectée d'être plus faible dans les oxydes de métaux de transition d'orbitale $4d$ que dans ceux à orbitale $3d$. Les composés de métaux à orbitale $4d$ relient naturellement deux différents régimes dans les composés $3d$ et $5d$ fortement corrélés. Particulièrement, on retrouve par exemple les composés presque similaires, Ca_2RuO_4 et Sr_2RuO_4 , qui présentent des comportements totalement différents. Le premier est un isolant de Mott tandis que le second est un métal qui devient superconducteur à basse température. Dans la présente thèse, j'expose la synthèse de monocristaux de MoPO_5 , et démontre leur propriétés magnétiques et thermodynamiques. J'ai trouvé que l'orbitale $4d^1$ du composé MoPO_5 est quenchée, et les ordres de l'aimant antiferromagnétique avec un moment dipolaire tout au long de l'axe c . Les transitions spin-flop ont été observées, ce qui indique le caractère magnétique anisotropique.

Néanmoins, les orbitales $5d$ sont spatialement plus étendues, donc on suppose que les valeurs

de la répulsion de Coulomb U devraient être réduites comparé à celles des oxydes de métaux de transition à orbitales $3d$ et $4d$. De ce fait, les comportements isolants des composés de métaux de transition ont été déconcertants. Une possible explication serait le fort couplage spin-orbite. Dans cette thèse, je présente la synthèse à pression ambiante ainsi que les propriétés physiques du nouveau $\text{Ba}_8\text{Al}_2\text{IrO}_{14}$ composé uniquement de Ir^{6+} iridate. De même pour le composé $\text{Ba}_{21}\text{Ir}_9\text{O}_{43}$ superposé en couches d'iridate. Je discuterai de la manière de synthèse de ces nouveaux composés en structure cristalline, et j'exposerai leur propriétés de transport d'électrons et magnétiques. $\text{Ba}_8\text{Al}_2\text{IrO}_{14}$ est un isolant de bande type-p, qui montre un couplage antiferromagnétique avec un ordre inférieur à 2 K. Quant à $\text{Ba}_{21}\text{Ir}_9\text{O}_{43}$, c'est un isolant avec un comportement Curie-Weiss, la transition magnétique est supprimée à basses températures (9 K) malgré la température caractéristique de Curie-Weiss de -90 K. J'ai aussi effectué des mesures de résistivité dépendantes de la pression sur les composés $5d \text{ Ir}_{0.95}\text{Pt}_{0.05}\text{Te}_2$, et trouvé que l'ordre de charge ayant une configuration dimérique avec $q=(1/5,0,1/5)$ est introduit, et que la superconductivité subit un croisement dimensionnel de la 3ème dimension à la 2ème dimension sous pression.

Mots clefs : Iridates, composés de métaux de transition, couplage spin-orbitale, magnétisme à basse dimension, superconductivité

Contents

| | |
|--|-----------|
| Abstract (English/Français/Deutsch) | i |
| List of figures | ix |
| List of tables | xv |
| 1 Introduction | 1 |
| 2 Physics of Transition Metal Compounds | 7 |
| 2.1 Single-site Interaction | 7 |
| 2.1.1 Crystal Field Effect | 7 |
| 2.1.2 Hund's Rules | 9 |
| 2.1.3 Spin-Orbit Coupling (SOC) | 10 |
| 2.2 Exchange Interaction | 12 |
| 2.2.1 Direct Exchange | 13 |
| 2.2.2 Superexchange | 13 |
| 2.2.3 RKKY | 14 |
| 2.2.4 Anisotropic Exchange | 15 |
| 2.3 Iridates | 15 |
| 2.3.1 Kitaev Model | 16 |
| 2.3.2 Ruddlesden-Popper Series of Iridates | 17 |
| 2.3.3 $6H$ Hexagonal Iridates | 18 |
| 3 Experimental Techniques | 21 |
| 3.1 Samples Synthesis | 21 |
| 3.1.1 Solid-state Reaction method | 21 |
| 3.1.2 Flux method | 23 |
| 3.2 Sample Characterization (X-ray and EDX) | 24 |
| 3.2.1 Single Crystal X-ray Diffraction (XRD) | 24 |
| 3.2.2 Energy Dispersive X-ray (EDX) spectroscopy | 27 |
| 3.3 Transport Measurement | 28 |
| 3.3.1 Electrical Resistivity Measurement | 28 |

Contents

| | | |
|----------|--|-----------|
| 3.3.2 | Seebeck Coefficient Measurement | 29 |
| 3.3.3 | Resistivity under Pressure | 31 |
| 3.4 | DC Magnetometry | 33 |
| 3.5 | Heat Capacity Measurement | 35 |
| 4 | Synthesis, Structure, Transport and Magnetic Properties of 5d Transition Metal Compounds—Iridates | 39 |
| 4.1 | Novel Ir ⁶⁺ System Ba₈Al₂IrO₁₄ | 39 |
| 4.1.1 | Motivation for This Work | 39 |
| 4.1.2 | Synthesis and Crystal Structure | 40 |
| 4.1.3 | Transport Properties | 45 |
| 4.1.4 | Magnetic Properties | 48 |
| 4.1.5 | Conclusion | 50 |
| 4.2 | Possible unusual spin state of Ir ⁴⁺ in Ba₂₁Ir₉O₄₃ single crystal | 50 |
| 4.2.1 | Motivation for This Work | 50 |
| 4.2.2 | Synthesis and Crystal Structure | 51 |
| 4.2.3 | Transport Properties | 55 |
| 4.2.4 | Magnetic Properties | 58 |
| 4.2.5 | Electron Spin Resonance | 63 |
| 4.2.6 | Conclusion | 65 |
| 4.3 | Pressure induced two-dimensional superconductivity in Ir_{0.95}Pt_{0.05}Te₂ | 65 |
| 4.3.1 | Motivation for This Work | 65 |
| 4.3.2 | Synthesis and Crystal Structure | 66 |
| 4.3.3 | Resistivity for Ir_{0.95}Pt_{0.05}Te₂ | 67 |
| 4.3.4 | Resistivity for Ir_{0.96}Pt_{0.04}Te₂ | 71 |
| 4.3.5 | Conclusion | 72 |
| 5 | Orbitally quenched $S = 1/2$ magnetic insulator MoPO₅ | 75 |
| 5.1 | Motivation for This Work | 75 |
| 5.2 | Synthesis and Crystal Structure | 76 |
| 5.3 | Speicific heat | 77 |
| 5.4 | Suscepetibility and magnetization | 78 |
| 5.5 | Electron spin resonance | 80 |
| 5.6 | Neutron diffraction | 82 |
| 5.7 | Conclusion | 84 |
| 6 | Kagome-like planar compound Cu₂OSO₄ | 87 |
| 6.1 | Motivation for This Work | 87 |
| 6.2 | Synthesis and Crystal Structure | 87 |
| 6.3 | Suscepetibility and magnetization | 89 |

| | | |
|----------|--------------------------|------------|
| 6.4 | Speicific heat | 92 |
| 6.5 | Conclusion | 95 |
| 6.6 | Future work | 95 |
| 7 | Conclusions | 97 |
| | Bibliography | 108 |
| | Acknowledgements | 109 |
| | Curriculum Vitae | 111 |

List of Figures

| | | |
|------|--|----|
| 1.1 | Transition metal elements in the periodic table. | 1 |
| 1.2 | DOS as a function of the local Coulomb interactions: (a) the case of free electrons in metals and the Fermi level is localized on the center of the band, (b) weakly correlated materials ($U < W$), (c) strongly correlated electron systems ($U \sim W$), and (d) the case of localized electrons in Mott insulator, cited from [1]. | 2 |
| 1.3 | Schematics of geometric frustration. (right:) A picture of the highly frustrated kagome lattice, cited from [2]. | 3 |
| 1.4 | The energy diagrams for the $5d^5$ (t_{2g}^5) configuration (a) without the spin-orbital coupling and Coulomb repulsion, (b) with a large Coulomb repulsion but without the spin-orbital coupling, (c) with spin-orbital coupling but without the Coulomb repulsion, and (d) with the spin-orbital coupling and Coulomb repulsion. (e) $5d$ level splittings by the crystal field and spin-orbital coupling, cited from [3]. | 4 |
| 2.1 | $3d$ -orbitals with the two subsets e_g and t_{2g} , cited from [4]. | 8 |
| 2.2 | Schematic of the spin-orbit coupling. | 10 |
| 2.3 | Values for the spin-orbit parameter for the valence shells of neutral atoms, cited from [5]. | 11 |
| 2.4 | Superexchange interaction in a magnetic oxide, cited from [6]. | 14 |
| 2.5 | The explanation of the weak ferromagnetism due to the Dzyaloshinski-Moriya interaction. The antiferromagnetic state (a) without and (b) with weak ferromagnetism. | 15 |
| 2.6 | $5d$ level splittings by the crystal field and spin-orbital coupling, cited from [3]. | 16 |
| 2.7 | The patterns of the structure unit cells and their spin-coupling. (a) Triangular and (b) hexagonal unit cells [7]. | 16 |
| 2.8 | The Ruddlesden-Popper series of $\text{Sr}_{n+1}\text{Ir}_n\text{O}_{3n+1}$, cited from [8]. | 17 |
| 2.9 | The band structure of Ruddlesden-Popper series of $\text{Sr}_{n+1}\text{Ir}_n\text{O}_{3n+1}$ ($n = 1, 2, \infty$), cited from [8] and [9]. | 18 |
| 2.10 | (a) The crystal structure of $\text{Ba}_3\text{ZnIr}_2\text{O}_9$; (b) Ir ions form triangular lattice, cited from [10]. | 19 |

List of Figures

| | | |
|------|--|----|
| 3.1 | A schematic of the self-flux method: (a) powder of starting materials and flux in the alumina crucible, (b) the formation process of the single crystals during the cooling process, (c) the resultant single crystals after the crystal growth process, and (d) the picture of the crystals in the alumina crucible. | 23 |
| 3.2 | The description of Bragg's law for X-ray Diffraction. | 24 |
| 3.3 | The appearance and scheme of a four-circle goniometer with Kappa geometry, cited from [11]. | 25 |
| 3.4 | Summary of single crystal XRD technique, cited from [12]. | 26 |
| 3.5 | The diagram of energy level for Ag, cited from [13]. | 27 |
| 3.6 | Electrical resistance measurement by four probe method. | 28 |
| 3.7 | (a) Schematic of the Seebeck effect, which explains that a temperature gradient causes a potential difference. (b) Ideal Seebeck coefficient measurement geometry, with thermocouples making small point contacts, cited from [14]. . . | 29 |
| 3.8 | Line drawing of the arrangement used in Seebeck measurements, cited from [15] | 30 |
| 3.9 | Schematic of a piston-cylinder pressure cell, cited from [16]. | 32 |
| 3.10 | Feedthrough for a typical piston-cylinder pressure cell with sample board, cited from [17]. | 33 |
| 3.11 | Schematics of SQUID magnetometer with longitudinal detection coils, cited from [18]. | 34 |
| 3.12 | Hydrostatic piston-cylinder type pressure cell for the magnetization measurements in the MPMS SQUID magnetometer, cited from [19]. | 35 |
| 3.13 | Schematics of PPMS Heat Capacity Option. (a) and (b) Thermal connection to the sample and sample platform, (c) Temperature change vs. time induced by a pulse of heat, cited from [20, 21]. | 36 |
| 4.1 | (a) A schematic of the crystal growth process with the flux method. (b) Representative single crystals of $\text{Ba}_8\text{Al}_2\text{IrO}_{14}$ | 40 |
| 4.2 | (a) X-ray EDS analysis performed on $\text{Ba}_8\text{Al}_2\text{IrO}_{14}$ | 41 |
| 4.3 | Crystal structure of $\text{Ba}_8\text{Al}_2\text{IrO}_{14}$. Red and green polyhedral indicate IrO_6 octahedra and AlO_4 tetrahedra, respectively. The black arrows mark the long axis direction of the elongated octahedra. The unit cell is outlined in red. The inset shows AlO_4 tetrahedron with the extremely large ADP ellipsoid of non-split oxygen atom with atomic displacement ellipsoids at 50% probability. Split oxygen atoms, O5a and O5b, are shown with half spheres indicating their occupation of 50%. | 43 |
| 4.4 | (a) Electrical resistivity of $\text{Ba}_8\text{Al}_2\text{IrO}_{14}$. The inset shows $d\ln\rho/d(e/k_B T)$ vs. T . The red dashed line is the guide to eyes of this fitting. $E_a \sim 0.29$ eV is estimated above 350 K in this plot. (b) The Seebeck coefficient of $\text{Ba}_8\text{Al}_2\text{IrO}_{14}$ | 46 |

| | | |
|------|--|----|
| 4.5 | (a) Transmission and reflectivity spectra as a function of photon energy for $\text{Ba}_8\text{Al}_2\text{IrO}_{14}$ at room temperature. (b) The real and imaginary part of the dielectric function. (c) The real part of optical conductivity, $\sigma_1(\omega)$, modeled from the transmission, reflectivity and ellipsometry data, shown at 300 K. | 47 |
| 4.6 | (a) Temperature dependence of M/H which approximates the magnetic susceptibility except below 10 K where $M(T)$ start to deviate from linear of $\text{Ba}_8\text{Al}_2\text{IrO}_{14}$ under various fields applied parallel to the b -axis. Both ZFC and FC data are shown. The inset shows inverse magnetic susceptibility $1/(M/H - \chi_0)$ versus temperature T in a magnetic field $H = 1$ T (ZFC). (b) Temperature dependent magnetic susceptibility of $\text{Ba}_8\text{Al}_2\text{IrO}_{14}$ under $H = 1$ T applied perpendicular and parallel to the b -axis, respectively, in ZFC. The inset shows $(M/H)_\perp(T)$ versus $(M/H)_\parallel(T)$ | 48 |
| 4.7 | Isothermal magnetization M versus magnetic field H applied parallel to the b -axis at various temperatures T . The dashed lines are fits to the Brillouin functions for $S = 3/2$, $g = 0.58$ | 49 |
| 4.8 | (a) Crystal structure of $\text{Ba}_{21}\text{Ir}_9\text{O}_{43}$ where a unit cell is drawn by solid line. (b) Two different layers of triangular lattice Ir-O polyhedra, labeled as Layer I [$\text{Ba}_9\text{Ir}_6\text{O}_{27}$] $^{-6}$ (left) and Layer II [$\text{Ba}_{12}\text{Ir}_3\text{O}_{16}$] $^{+6}$ (right). (c) The Ir-O polyhedra: blue and green IrO_6 octahedra are geometrically identical within one standard deviation; face-sharing orange octahedra form a Ir_2O_9 dimer; red polyhedron is shown as a statistical superposition of two possible IrO_4 triangular pyramid, having the same geometry but opposite in orientation along c direction, with 50 % occupancy on every oxygen sites. (d) Representative single crystals of $\text{Ba}_{21}\text{Ir}_9\text{O}_{43}$. . . | 52 |
| 4.9 | (a) In-plane (ρ_{ab}) and out-of-plane (ρ_c) resistivity as a function of temperature where solid and dotted lines represent the two-dimensional VRH model and $\rho \propto T^{-3}$ behavior. (b) $\ln \rho_{ab}$ versus $T^{1/3}$ where solid line is a fit to the VRH model. (c) Log-log plot of $\rho_{ab}(T)$ where dotted line represents T^{-3} dependence. | 55 |
| 4.10 | Seebeck coefficient S as a function of temperature. The inset shows p -type to n -type crossover with decreasing temperature around 150 K. | 56 |
| 4.11 | $\ln \rho_{ab}$ versus $T^{1/3}$ (blue curve) and $T^{1/4}$ (red curve) where black solid lines are the fits to the 2D and 3D VRH model, respectively. | 57 |
| 4.12 | A possible schematic of the electronic model. | 58 |
| 4.13 | (a) Magnetic susceptibility M/H as a function of temperature under $H = 1$ T applied perpendicular and parallel to the c axis, respectively. (b) Inverse magnetic susceptibility $1/(M/H - \chi_0)$ versus temperature in $H = 1$ T. (c) The susceptibility as a function of temperature in various applied fields. (d) The decay of thermoremanent magnetization as a function of time at 5 K. | 59 |

List of Figures

| | |
|--|----|
| 4.14 (a) Isothermal magnetization as a function of field for different temperatures. (b) Magnetization loop measurement at 5 K with barely visible hysteresis, where a zoom-in is shown in the inset. | 61 |
| 4.15 (a) Angular dependence of the g factor at room temperature. (b) Upper: ESR spectra at 6 K measured in ZFC and FC conditions for $H \parallel c$. Lower: FC ESR spectra at 6 K where the field has been either applied along c axis then rotated toward ab plane, or applied from the beginning into the ab plane. | 64 |
| 4.16 (a) The comparison of the resistivity as a function of temperature between single crystals and polycrystal of IrTe_2 . (b) The structure of IrTe_2 at room temperature and low temperature. The high temperature and low temperature unit cells are drawn by blue and black solid lines, respectively, cited from [22, 23]. | 65 |
| 4.17 Phase diagram of $\text{Ir}_{1-x}\text{Pt}_x\text{Te}_2$ [24]. | 66 |
| 4.18 Representative single crystals of $\text{Ir}_{0.95}\text{Pt}_{0.05}\text{Te}_2$ | 67 |
| 4.19 (a) Temperature dependence of resistivity for $\text{Ir}_{0.95}\text{Pt}_{0.05}\text{Te}_2$ at various pressures. (a) The pressures are below the critical pressure for structure phase transition. (b) The pressures are above the critical pressure. The insets show the superconducting transition part of each corresponding figure. | 68 |
| 4.20 (Color online) (a) Residual resistivity $\rho_0 = \rho(0)$ versus applied pressure. (b) Inelastic component of the resistivity versus applied pressure. | 69 |
| 4.21 (Color online) The superconducting transition as a function of temperature under different pressures. The black dashed lines correspond to fits to Eq. 4.14. | 70 |
| 4.22 (Color online) Pressure - temperature phase diagrams of the (a) Ir-dimerization and (b) superconductivity. | 71 |
| 4.23 (Color online) The resistivity as a function of temperature for $\text{Ir}_{0.96}\text{Pt}_{0.04}\text{Te}_2$ and $\text{Ir}_{0.95}\text{Pt}_{0.05}\text{Te}_2$ under ambient pressure. | 72 |
| 4.24 (Color online) Three dimensional phase diagrams of the (a) Ir-dimerization and (b) superconductivity. | 73 |
| 5.1 (a) Crystal structure projected onto the ac planes showing a chain-like arrangement of MoO_6 octahedra (yellow) and (b) onto the ab planes showing the coupling between the chains via PO_4 tetrahedra (blue). Dashed lines represent the unit cells. (c) Photograph of a representative single crystal. | 76 |
| 5.2 (a) Specific heat C_p as a function of temperature in zero field (circle) and in 14 T (square). Solid line represents the best fit of the simulated lattice contribution using the Debye (dash-dotted line) and Einstein (dashed line) terms. Inset provides an enlarged view of the low temperature region. (b) Left axis: magnetic part of the specific heat, C_{mag} , divided by temperature (circle). Right axis: solid line is the entropy calculated from the C_{mag} | 77 |

| | | |
|-----|--|----|
| 5.3 | (a) Magnetic susceptibility $\chi(T)$ in a field $H = 0.1$ T applied in parallel (circle) and perpendicular (square) to the c axis. Inset shows the inverse susceptibility $1/(\chi - \chi_0)$ against temperature where solid line is a fit to the Curie-Weiss formula. (b) Isothermal magnetization $M(H)$ for $H \parallel c$ (filled symbol) and $H \perp c$ (open symbol) at various temperatures. Inset plots the field derivative dM/dH for $H \parallel c$. (c) M/H as a function of temperature in different magnetic fields applied along c axis. (d) Magnetic phase diagram from the susceptibility (square), specific heat (diamond), and magnetization (circle) data. Lines are guides to the eye. | 79 |
| 5.4 | Angular dependence of the g factor at room temperature, where filled symbols are for the field varied on the ac plane while open symbols on the ab plane. . . | 81 |
| 5.5 | (a) Resonance field shift B_0 (circle, right axis) and line width (square, left axis) of the spectrum as a function of temperature. Inset plots normalized spin susceptibility $\chi(T)/\chi(300\text{ K})$ as a function of temperature. (b) Temperature evolution of the spectrum for $H \parallel c$ across the transition (black filled circles). Solid line is a sum of two contributions from intrinsic (dotted line) and defect (dashed line) susceptibility. At 5 K, the data for $H \perp c$ (pink filled circles) are overlaid. | 82 |
| 5.6 | Neutron diffraction measurements of rotation scans through (a): (100) and (b): (001) reflections recorded at 5 and 25 K. (c) Temperature evolution of the Bragg peak intensity. The solid line is a power-law fit $I(T) \propto (T_N - T)^{2\beta}$ with the parameters $\beta = 0.23$ and $T_N = 16.17 \pm 0.06$ K. (d) (010) peak intensity as a function of magnetic field. | 83 |
| 6.1 | (a) crystal structure of Cu_2OSO_4 ; (b) a single layer of copper ions forming a kagome-like structure where only Cu^{2+} ions are shown for simplicity in the ab plane; (c) perpendicular view of the copper layer, showing two Cu2 sites between Cu1 chains. | 88 |
| 6.2 | Photograph of a representative single crystal of Cu_2OSO_4 | 89 |
| 6.3 | Susceptibility as a function of temperature in different magnetic fields applied perpendicular to the ab plane of the crystal. (a) Under low field $H \leq 0.1$ T; (b) under high field $0.1\text{ T} \leq H \leq 5$ T. | 90 |
| 6.4 | Isothermal magnetization as a function of magnetic field applied perpendicular to the ab plane of the crystal for different temperatures. Inset: magnetization loop measurement at 5 K where a zoom-in is shown. | 90 |
| 6.5 | Inverse magnetic susceptibility $1/(M/H - \chi_0)$ versus temperature in $H = 0.1$ T for $H \parallel ab$ and $H \perp ab$ | 91 |
| 6.6 | (a) Magnetic susceptibility versus temperature in $H = 50$ oe for $H \parallel ab$ and $H \perp ab$. (b) Magnetic isotherm at 5 K with the field applied for $H \parallel ab$ and $H \perp ab$ | 92 |

List of Figures


- 6.7 (a) Magnetic susceptibility versus temperature in the FCC and FCW protocols. Thermal hysteresis observed in the susceptibility of Cu_2OSO_4 indicating the first order transition in $H = 50$ oe for $H \parallel ab$. (b) Magnetic isotherm at 5 K with the field applied for $H \parallel ab$ and $H \perp ab$ 92
- 6.8 (a) Specific heat C_p as a function of temperature in zero field (black circle). Red solid line represents the best fit of the simulated lattice contribution using the Debye (blue dashed line) and Einstein (green dashed line) terms. Inset provides an enlarged view of the low temperature region in zero field, 1 T, 5 T and in 14 T. (b) Left axis: magnetic part of the specific heat, C_{mag} , divided by temperature (black circle). Right axis: solid line is the entropy calculated from the C_{mag} 93
- 6.9 The temperature versus time relaxation at $T \sim 20$ K. (a) Time scan below T_c ; (b) time scan across T_c 94

List of Tables

| | | |
|------|--|----|
| 3.1 | Classification of crystal growth processes, cited from [25]. | 22 |
| 4.1 | Details of the data collection and structure refinement for $\text{Ba}_8\text{Al}_2\text{IrO}_{14}$. The diffraction study is performed at 293(2) and 90(2) K using Mo $K\alpha$ radiation with $\lambda = 0.71073 \text{ \AA}$. The lattice is monoclinic, $C2/m$ space group, with $Z = 2$. A full-matrix least-squares method was employed to optimize F^2 | 42 |
| 4.2 | Atomic coordinates and equivalent isotropic displacement parameters [$\text{\AA}^2 \cdot 1000$] for $\text{Ba}_8\text{Al}_2\text{IrO}_{14}$ | 42 |
| 4.3 | ADP atomic parameters in $\text{Ba}_8\text{Al}_2\text{IrO}_{14}$ | 44 |
| 4.4 | Selected interatomic distances (\AA) for $\text{Ba}_8\text{Al}_2\text{IrO}_{14}$ | 44 |
| 4.5 | Atomic occupancy for $\text{Ba}_8\text{Al}_2\text{IrO}_{14}$ | 44 |
| 4.6 | Details of the data collection and structure refinement for $\text{Ba}_{21}\text{Ir}_9\text{O}_{43}$ obtained at room temperature using Mo $K\alpha$ radiation with $\lambda = 0.71073 \text{ \AA}$ | 53 |
| 4.7 | Atomic coordinates and equivalent isotropic displacement parameters for $\text{Ba}_{21}\text{Ir}_9\text{O}_{43}$ | 53 |
| 4.8 | ADP atomic parameters in $\text{Ba}_{21}\text{Ir}_9\text{O}_{43}$ | 54 |
| 4.9 | Selected interatomic distances (\AA) for $\text{Ba}_{21}\text{Ir}_9\text{O}_{43}$ | 54 |
| 4.10 | Calculation of valence state of Ir ions. | 62 |
| 4.11 | Valence states in octahedral and triangular pyramid environment for the different Ir ions. | 62 |
| 5.1 | Basis functions of irreducible representation Γ_v separated into real and imaginary components and resolved along the crystallographic axes. The two equivalent Mo ions are related by an inversion through the origin. | 84 |

1 Introduction

Transition metal compounds based on transition metals probably are one of the most fascinating class of materials, which show a very wide variety of structure, magnetic and electronic properties. A variety of complex structures exhibited by transition metal compounds are worthy to study, including perovskite, pyrochlore and low dimensional structure. Transition metal compounds also presented many interesting phenomena of electronic and magnetic properties, such as the discovery of high temperature superconducting oxides, colossal magnetoresistance and multiferroicity. The unusual properties are clearly due to the elements



PERIODIC TABLE

Representative Elements

← s-block →

Representative Elements

← p-block →

Noble gases

18

| | | | | | | | | | | | | | | | | | | | | |
|---|----|----|----|----|----|----|----|----|----|----|----|----|----|----|----|----|----|----|--|--|
| 1 | 2 | | | | | | | | | | | 13 | 14 | 15 | 16 | 17 | 18 | | | |
| 1 | H | | | | | | | | | | | | | | | | He | | | |
| 2 | Li | Be | | | | | | | | | | | B | C | N | O | F | Ne | | |
| 3 | Na | Mg | | | | | | | | | | | Al | Si | P | S | Cl | Ar | | |
| 4 | K | Ca | Sc | Ti | V | Cr | Mn | Fe | Co | Ni | Cu | Zn | Ga | Ge | As | Se | Br | Kr | | |
| 5 | Rb | Sr | Y | Zr | Nb | Mo | Tc | Ru | Rh | Pd | Ag | Cd | In | Sn | Sb | Te | I | Xe | | |
| 6 | Cs | Ba | | Hf | Ta | W | Re | Os | Ir | Pt | Au | Hg | Tl | Pb | Bi | Po | At | Rn | | |
| 7 | Fr | Ra | | Rf | Db | Sg | Bh | Hs | Mt | | | | | | | | | | | |

Transition Elements

d-block

Inner Transition Elements

f-block

| | | | | | | | | | | | | | | |
|----|----|----|----|----|----|----|----|----|----|----|----|----|----|----|
| La | Ce | Pr | Nd | Pm | Sm | Eu | Gd | Tb | Dy | Ho | Er | Tm | Yb | Lu |
| Ac | Th | Pa | U | Np | Pu | Am | Cm | Bk | Cf | Es | Fm | Md | No | Lr |

Figure 1.1: Transition metal elements in the periodic table.

with incomplete d shells in the periodic table. Elements from 3rd to 12th group are commonly known as d-block elements or transition elements, as shown in Figure 1.1.

To understand the link between the structure and the unusual physical behaviors of transition metal compounds, it is necessary to find a proper description of the binding between valence electrons and atoms. The band theory and the localized electron theory are two descriptions [26]. The density of states (DOS) of electrons in a material varies as a function of the local Coulomb interactions as described in Figure 1.2 [1].

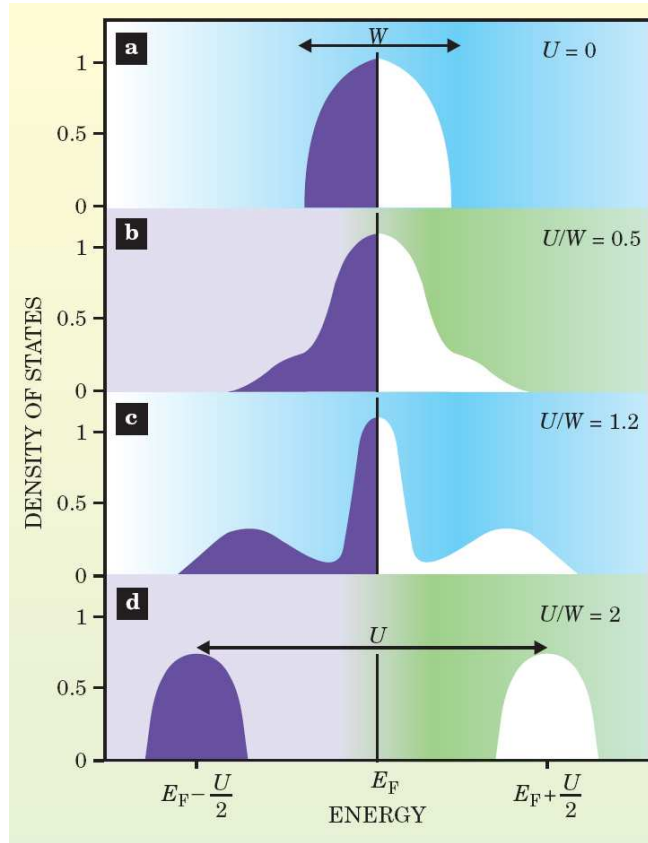


Figure 1.2: DOS as a function of the local Coulomb interactions: (a) the case of free electrons in metals and the Fermi level is localized on the center of the band, (b) weakly correlated materials ($U < W$), (c) strongly correlated electron systems ($U \sim W$), and (d) the case of localized electrons in Mott insulator, cited from [1].

When the electron-electron Coulomb repulsion is fairly strong (shown by a large energy U value and a small kinetic energy of electrons called band width energy W ($U \gg W$)), the localized electron theory can be used, which is the situation in Mott insulator. On the other hand, when $U \sim 0$ which is corresponding to the situation of the metals ($U \ll W$), the DOS is assumed to have the Fermi level located in the middle of the band, and the band theory is applicable. When $U < W$ which is the case for weakly correlated materials, DOS still resembles

free electrons which are described as quasiparticles. When the scale of the correlation between electrons is similar to that of the band width ($U \sim W$), this case is referred to strong correlated electron systems.

$3d$ transition metal compounds have drawn intensive attention and the electric states are well localized due to the large Coulomb repulsion U . Most stoichiometric $3d$ transition metal compounds are antiferromagnetic Mott insulators [27]. Among them, many low dimensional magnetic transition metal compounds have been investigated because of the discovery of high temperature superconductivity in layered cuprates. To understand the low dimensional magnetism of materials, it is important to consider not only the dimensionality of the lattice but also that of the spin. When the antiferromagnetic interactions and the triangular lattice are combined, as shown in Figure 1.3, two adjacent and anti-parallel spins are placed and the system cannot reach an energy minimum. As a result, the effects of metastability and time-dependent relaxation occur in the frustrated systems [6].

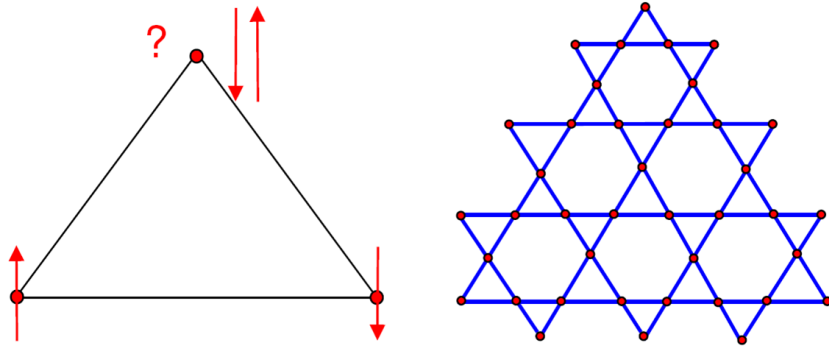


Figure 1.3: Schematics of geometric frustration. (right:) A picture of the highly frustrated kagome lattice, cited from [2].

Low dimensional geometrically frustrated systems, based on triangles of interacting spins with antiferromagnetic (AFM) interaction, for example $S = 1/2$ kagome lattice antiferromagnets [28, 29, 30], are at the forefront of condensed matter field.

On the other hand, $4d$ transition metal compounds are systems with weakly correlated wide band because of the weaker electron correlation in $4d$ transition metal compounds compared to the $3d$ case. The $4d$ transition metal compounds naturally bridge two different regimes of the strongly correlated $3d$ compounds and $5d$ compounds. Most notably, for instance, it is intriguing that Ca_2RuO_4 and Sr_2RuO_4 that seem similarly with each other display totally different behaviors. The former is a Mott insulator [31, 32, 33] while the latter is metallic and becomes superconducting at low temperature [33, 34].

For $5d$ transition metal compounds, $5d$ orbitals are expected to be more extended and the

Coulomb repulsion U values are further reduced compared to the $3d$ and $4d$ cases. Therefore, a tendency to metallic behavior is expected. However, experiments have shown that some compounds such as $\text{Sr}_3\text{Ir}_2\text{O}_7$ and Na_2IrO_3 show insulating behavior [35, 36, 37]. The correlation effects are expected to be important in $5d$ insulating transition metal compounds [38, 39, 40]. A possible reason is the strong spin-orbit coupling of the heavy transition metal elements.

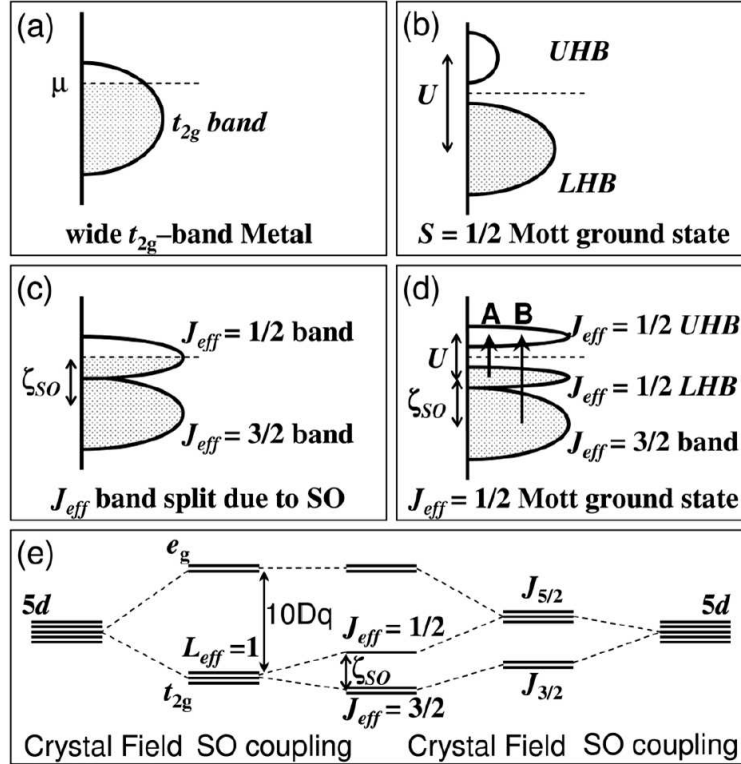


Figure 1.4: The energy diagrams for the $5d^5$ (t_{2g}^5) configuration (a) without the spin-orbital coupling and Coulomb repulsion, (b) with a large Coulomb repulsion but without the spin-orbital coupling, (c) with spin-orbital coupling but without the Coulomb repulsion, and (d) with the spin-orbital coupling and Coulomb repulsion. (e) $5d$ level splittings by the crystal field and spin-orbital coupling, cited from [3].

The energy diagrams for the $5d^5$ (t_{2g}^5) configuration were described in Figure 1.4, which explained that large spin-orbital coupling energy induced the emergence of a novel Mott ground state. For $3d$ and $4d$ compounds, a $S=1/2$ Mott insulating state is shown due to the large U (Figure 1.4(a) and (b)). For $5d$ transition metal compounds, the t_{2g} orbital states were split into $J_{eff}=1/2$ doublet and $J_{eff}=3/2$ quartet bands due to the strong spin-orbital coupling, in which J_{eff} is the effective total angular momentum (Figure 1.4(c)). The $J_{eff}=1/2$ bands can be very narrow and the small U opens a gap, resulting in a $J_{eff}=1/2$ Mott insulator (Figure 1.4(d)).

My results obtained in the past four years studying $3d$, $4d$ and $5d$ transition metal compounds are organized in seven chapters. Chapter 2 provides an overview of the physics of heavy transition metal compounds. Chapter 3 is devoted to the experimental techniques for synthesizing and characterizing these systems. In chapter 4 (the most important one), two novel iridates $\text{Ba}_8\text{Al}_2\text{IrO}_{14}$ and $\text{Ba}_8\text{Al}_2\text{IrO}_{14}$ were synthesized and the pressure-dependent resistivity measurements were performed on the Ir-based compound $\text{Ir}_{0.95}\text{Pt}_{0.05}\text{Te}_2$. In Chapter 5, the synthesis, magnetic and thermodynamic properties of $4d$ transition metal oxides MoPO_5 were presented. Chapter 6 describes the low dimensional magnetism of spin-1/2 $3d$ antiferromagnet. Chapter 7 gives the conclusions.

2 Physics of Transition Metal Compounds

Transition metal compounds exhibit very wide variety of magnetic and electrical behaviors due to their incomplete d shells. The electrons in transition metal compounds interact with each other strongly. In this chapter, we will describe the basic physical properties of the electronic structure of transition metal compounds.

2.1 Single-site Interaction

2.1.1 Crystal Field Effect

The crystal field effect (CFE) describes the breaking of the degeneracies of the d electron orbital states.

For a free d -ion, the orbital angular momentum is $l=2$. The d -orbital configurations are five-fold degenerate in a spherical polar coordinates due to $2l+1=5$. In a crystal of transition metal oxides, however, the ions are surrounded by oxygen ions, so the octahedral and tetrahedral coordinations are the most common environmental symmetries. Considering a crystal field of octahedron, d -ion is placed in the center with same distances from six oxygen ions. The five

eigen-functions of the d electron are given by:

$$d(x^2 - y^2) \propto \sqrt{\frac{2\pi}{5}}(Y_2^2 + Y_2^{-2}) = \frac{\sqrt{3}}{2} \frac{x^2 - y^2}{r^2} \quad (2.1)$$

$$d(3z^2 - r^2) \propto \sqrt{\frac{4\pi}{5}}Y_2^0 = \frac{1}{2} \frac{3z^2 - r^2}{r^2} \quad (2.2)$$

$$d(xy) \propto \frac{1}{i} \sqrt{\frac{2\pi}{5}}(Y_2^2 - Y_2^{-2}) = \sqrt{3} \frac{xy}{r^2} \quad (2.3)$$

$$d(yz) \propto \sqrt{\frac{2\pi}{5}}(Y_2^{-1} + Y_2^1) = \sqrt{3} \frac{yz}{r^2} \quad (2.4)$$

$$d(zx) \propto \frac{1}{i} \sqrt{\frac{2\pi}{5}}(Y_2^{-1} - Y_2^1) = \sqrt{3} \frac{zx}{r^2} \quad (2.5)$$

where $d(x^2 - y^2)$ and $d(3z^2 - r^2)$ are two higher energy states characterized by e_g orbitals. $d(xy)$, $d(yz)$ and $d(zx)$ are three lower energy states characterized by t_{2g} orbitals, because the latter group is farther from the ligands than the former and therefore experience less repulsion [41]. The radial distribution is shown in Figure 2.1.

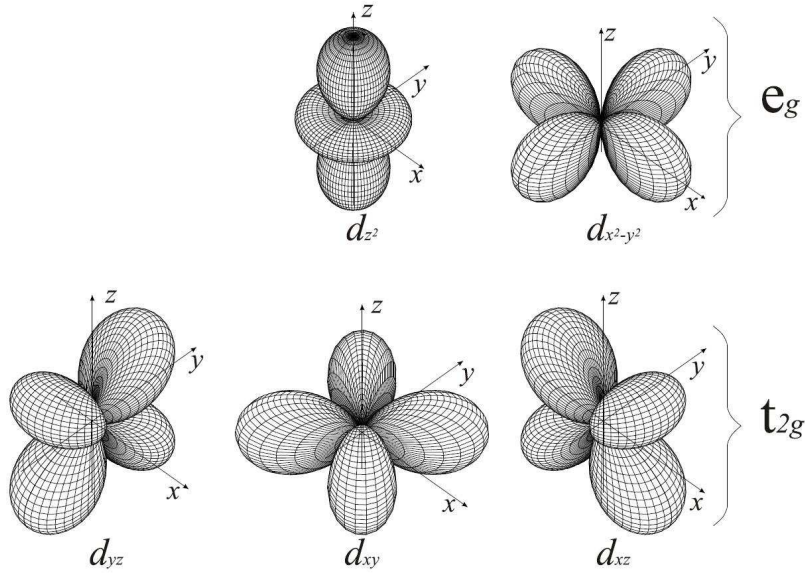


Figure 2.1: 3d-orbitals with the two subsets e_g and t_{2g} , cited from [4].

2.1.2 Hund's Rules

The orbital angular momentum \mathbf{L} generates a circular current, which produces a magnetic dipole moment of [42]

$$\mu_L = \mu_B \mathbf{L}, \quad (2.6)$$

in which μ_B is Bohr magneton, expressed by

$$\mu_B = \frac{\hbar e}{2m_e} = 9.274 \times 10^{-24} \text{ J/T} \quad (2.7)$$

The spin of electron produces a magnetic dipole moment of

$$\mu_s = g\mu_B \mathbf{S}. \quad (2.8)$$

The total angular momentum can be expressed by $\mathbf{J} = \mathbf{L} + \mathbf{S}$, in which $\mathbf{L} = \sum \mathbf{L}_i$ is orbital angular momentum and $\mathbf{S} = \sum \mathbf{S}_i$ is spin angular momentum. The combination of angular momentum quantum numbers for minimizing the energy is described by Hund's rules [6].

1. Maximize S .

Pauli exclusion principle has electrons with parallel spins staying in the different positions. The Coulomb repulsion between electrons are reduced, therefore minimizes the Coulomb energy.

2. Maximize L .

The electrons are orbiting in the same direction to prevent them from approaching each other, which minimizes the energy.

3. Minimize J for the shells that are less than half full and maximize J for ones that are more than half full shells.

$J = |L - S|$ is expressed for the less than half full shells and $J = |L + S|$ for the more than half full shells. The third rule is applicable in certain environment where the spin-orbit coupling becomes significant as other energy terms.

2.1.3 Spin-Orbit Coupling (SOC)

Spin-Orbit coupling describes the interaction between the spin s and the orbital angular momentum l . As shown in Figure 2.2, the magnetostatic energy can be expressed by

$$E = -\mathbf{m}_s \cdot \mathbf{H}_{orb} = -m_s H_{orb} \cos \theta, \quad (2.9)$$

The spin momentum can be expressed by

$$\langle m_s^z \rangle = -2 \frac{\mu_B}{\hbar} \langle s_z \rangle, \quad (2.10)$$

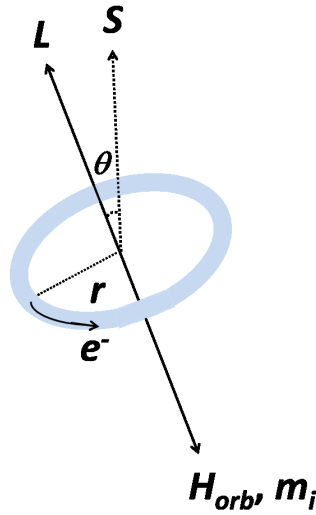


Figure 2.2: Schematic of the spin-orbit coupling.

At the center of the loop, the field is expressed by

$$H_{orb} = \frac{m_l}{2\pi\mu_0 r^3} = -\frac{eL}{4\pi m_e r^3}, \quad (2.11)$$

then the spin-orbit energy is obtained

$$E = -\mathbf{m}_s \cdot \mathbf{H}_{orb} = -\frac{e^2}{4\pi\epsilon_0 m_e^2 c^2 r^3} \mathbf{L} \cdot \mathbf{S}. \quad (2.12)$$

The quantum mechanical spin-orbit Hamiltonian corresponding to the above equation follows the Pauli equation. For an electron orbiting an atom, if we consider the nucleus orbiting the

electron, the magnetic field generated by a current can be expressed by [6]

$$\mathbf{B} = \frac{\boldsymbol{\varepsilon} \times \mathbf{v}}{c^2}, \quad (2.13)$$

in which

$$\boldsymbol{\varepsilon} = -\nabla V(r) = -\frac{\mathbf{r}}{r} \frac{dV(r)}{dr} \quad (2.14)$$

is the electron field and $V(r)$ is the potential energy. Then we can obtain the spin-orbit interaction Hamiltonian

$$H_{so} = -\frac{1}{2} \mathbf{m} \cdot \mathbf{B} = \frac{e\hbar^2}{2m_e c^2 r} \frac{dV(r)}{dr} \mathbf{S} \cdot \mathbf{L}, \quad (2.15)$$

in which the orbital angular momentum is

$$\hbar \mathbf{L} = m_e \mathbf{r} \times \mathbf{v}, \quad (2.16)$$

and the magnetic moment is

$$\mathbf{m} = \left(\frac{ge\hbar}{2m} \right) \mathbf{S}. \quad (2.17)$$

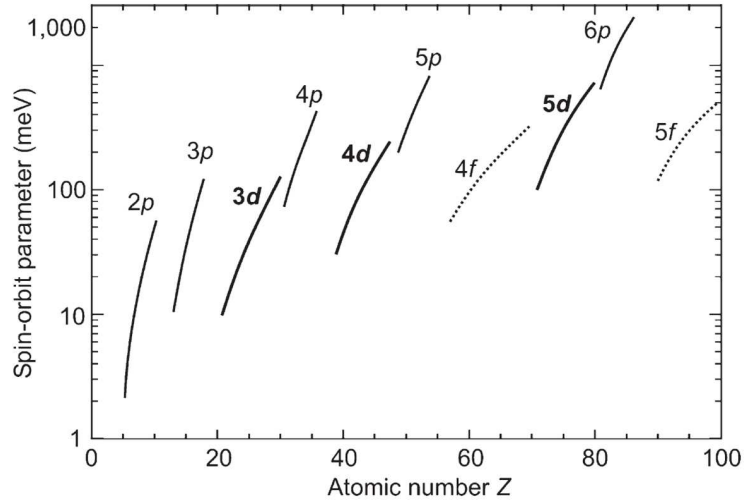


Figure 2.3: Values for the spin-orbit parameter for the valence shells of neutral atoms, cited from [5].

In a hydrogen-like atom the Coulomb can be expressed by

$$\frac{1}{r} \frac{dV(r)}{dr} = \frac{Ze}{4\pi\epsilon_0 r^3}, \quad (2.18)$$

and the electronic states can be given

$$\langle r^{-3} \rangle = \frac{Z^3}{a_0^3 n^3 l(l + \frac{1}{2})(l + 1)}, \quad (2.19)$$

in which, l and n are the quantum numbers of electronic states, so that the spin-orbit splitting is

$$\frac{Z^4 e^2 \hbar^2 \langle \mathbf{S} \cdot \mathbf{L} \rangle}{4\pi\epsilon_0 a_0^3 n^3 l(l + \frac{1}{2})(l + 1)}, \quad (2.20)$$

For Equation 2.15, we can express it by

$$H_{so} = \zeta_{nl}(r) \mathbf{S} \cdot \mathbf{L}, \quad (2.21)$$

where $\zeta_{nl}(r)$ is called the spin-orbit parameter. The theoretical values of the spin-orbit parameter are shown in Figure 2.3. We found the spin-orbit coupling becomes important for the 5d transition metals.

2.2 Exchange Interaction

The above section described the case of single-site interaction. In this sub-section we will describe the exchange interaction between sites.

Considering two electrons with the spatial coordinates \mathbf{r}_1 and \mathbf{r}_2 respectively, the wave function are given by $\psi_a(\mathbf{r}_1)$ and $\psi_b(\mathbf{r}_2)$. To obey exchange symmetry, the only states allowed are symmetrized or antisymmetrized product states [6]. The wave functions for the singlet state and the triplet state are Ψ_S ($S=0$) and Ψ_T ($S=1$), respectively.

The corresponding energy of the two possible states are

$$E_S = \int \Psi_S^* \hat{H} \Psi_S d\mathbf{r}_1 d\mathbf{r}_2 \quad (2.22)$$

$$E_T = \int \Psi_T^* \hat{H} \Psi_T d\mathbf{r}_1 d\mathbf{r}_2 \quad (2.23)$$

For a singlet state $\mathbf{S}_1 \cdot \mathbf{S}_2 = -3/4$ is obtained and $\mathbf{S}_1 \cdot \mathbf{S}_2 = 1/4$ for a triplet state. The effective Hamiltonian can be expressed by

$$\hat{H} = \frac{1}{4}(E_S + 3E_T) - (E_S - E_T)\mathbf{S}_1 \cdot \mathbf{S}_2, \quad (2.24)$$

The exchange constant J is defined as

$$J = \frac{E_S - E_T}{2} = \int \Psi_a^*(r_1) \Psi_b^*(r_2) \hat{H} \Psi_a(r_2) \Psi_b(r_1) dr_1 dr_2, \quad (2.25)$$

then we can express the spin-dependent term Hamiltonian as

$$\hat{H}^{spin} = -2J\mathbf{S}_1 \cdot \mathbf{S}_2. \quad (2.26)$$

For $J > 0$, the triplet state (high spin state $S=1$) is favored, corresponding to the ferromagnetic coupling. For $J < 0$, the singlet state (low spin state $S=0$) is favored, corresponding to the antiferromagnetic coupling [6].

For a many-body system, the above equation can be used for the interactions between atoms. The Hamiltonian can be expressed by

$$\hat{H} = -\sum J_{ij} \mathbf{S}_i \cdot \mathbf{S}_j, \quad (2.27)$$

2.2.1 Direct Exchange

Direct exchange interaction reflects the direct ion-ion exchange interaction. The electronic orbitals of the two ions overlap directly. Very often this interaction is too weak to create long-range order. In transition metals, it is difficult to justify the magnetic transitions are from direct exchange because the conduction electrons must be considered. So it is important to consider the indirect exchange interaction.

2.2.2 Superexchange

In many magnetic materials, there is no direct interaction between the magnetic ions. The electron orbitals are bridged by a non-magnetic ion, such as O^{2-} . The exchange mechanism is known as superexchange. Superexchange in a magnetic oxide is shown in Figure 2.4, where two transition metal ions M are separated by an O^{2-} ion. For the antiferromagnetic transition

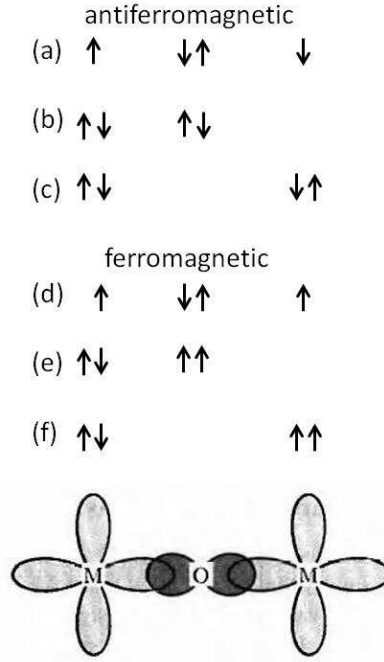


Figure 2.4: Superexchange interaction in a magnetic oxide, cited from [6].

metal oxides, Hubbard Hamiltonian can be expressed by [41]

$$H = -t \sum_{\langle ij \rangle \sigma} (c_{i\sigma}^\dagger c_{j\sigma} + h.c.) + U \sum_i n_{i\uparrow} n_{i\downarrow}, \quad (2.28)$$

in which t is the hopping integral and U is the Coulomb energy. Superexchange is a second-order process because it involves the O^{-2} orbitals and the M atom.

2.2.3 RKKY

RKKY interaction describes an interaction of conduction electron mediated exchange [6]. When the spins of the electrons at the Fermi surface pass by the localized electrons, the interaction occurs. The exchange interaction is indirect and the r -dependent exchange interaction $J_{RKKY}(r)$ can be expressed by [42]

$$J_{RKKY}(r) \propto \frac{\cos(2k_F r)}{r^3}, \quad (2.29)$$

in which r is the distance and k_F is the assumed spherical Fermi surface.

2.2.4 Anisotropic Exchange

In some low crystal symmetry cases, the antiferromagnetic material shows weak ferromagnetism because of the spins canting. Dzyaloshinski has discussed the anti-symmetric interaction can be given by

$$D \cdot (M_A \times M_B), \quad (2.30)$$

in which M_A and M_B are the sub-lattice magnetizations. As shown in Figure 2.5, the antiferromagnetic and anti-symmetric interaction can explain the existence of weak ferromagnetism. Moriya showed that the microscopic mechanism of the anti-symmetric interaction is because of the spin-orbit coupling, which plays a similar role as the O^{-2} ion in superexchange interaction. The Hamiltonian can be described by

$$H = \sum_{ij} J_{ij} S_i \cdot S_j + \sum_{ij} D_{ij} \cdot (S_i \times S_j) + \sum_{ij} S_i \Gamma_{ij} S_j, \quad (2.31)$$

in which $\sum_{ij} J_{ij} S_i \cdot S_j$ describes the isotropic superexchange interaction and the latter two terms describe the anisotropic superexchange interaction. $\sum_{ij} S_i \Gamma_{ij} S_j$ is symmetric and $\sum_{ij} D_{ij} \cdot (S_i \times S_j)$ is anti-symmetric, so called Dzyaloshinski-Moriya interaction.

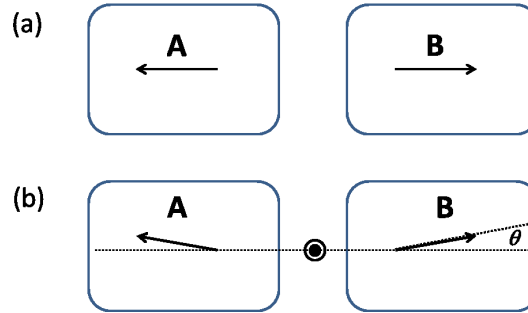


Figure 2.5: The explanation of the weak ferromagnetism due to the Dzyaloshinski-Moriya interaction. The antiferromagnetic state (a) without and (b) with weak ferromagnetism.

2.3 Iridates

Compared with the $3d$ and $4d$ transition metals, the $5d$ orbitals of Ir-based compounds are further extended and the Coulomb repulsion U values correspondingly reduced. A tendency to metallic behavior is expected. However, some iridates compounds show insulating behavior [35, 36, 37] and the correlation effects are important in iridates [38, 39, 40]. A possible reason is the strong spin-orbit coupling of the heavy transition metal elements. Figure 2.6 explains a large spin-orbit coupling energy resulting in the emergence of a novel Mott ground state.

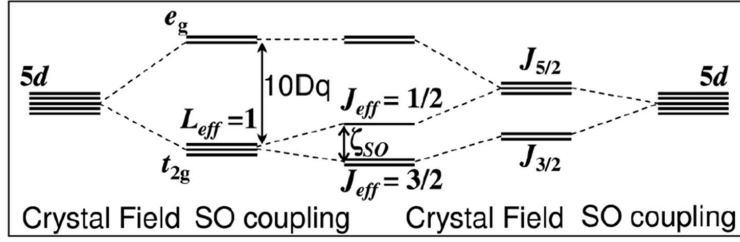


Figure 2.6: 5d level splittings by the crystal field and spin-orbital coupling, cited from [3].

Sr_2IrO_4 is a typical example of Ir-based compounds with the layered perovskite structure, showing insulating behavior with weak ferromagnetism. The electronic configuration of Ir^{4+} is $(1s)^2(2s)^2(2p)^6(3s)^2(3p)^6(3d)^{10}(4s)^2(4p)^6(4d)^{10}(5s)^2(5p)^6(4f)^{14}(5d)^5$. There are 5 electrons in the d orbitals. As shown in Figure 2.6, 4 d electrons stay into the lower $J_{eff} = 3/2$ states and the other d electron remains into the upper lying $J_{eff} = 1/2$ state. The very narrow $J_{eff} = 1/2$ band results in the Mott insulating behavior.

2.3.1 Kitaev Model

Recently Kitaev described an interesting two dimensional frustrated spin-1/2 model, so called Kitaev model [43]. The Hamiltonian can be expressed as

$$H = J_x \sum_{(ij)_x} S_i^x S_j^x + J_y \sum_{(ij)_y} S_i^y S_j^y + J_z \sum_{(ij)_z} S_i^z S_j^z, \quad (2.32)$$

Figure 2.7(a) shows the triangular unit cell and its corresponding spin coupling, representing ABO_2 layered compounds. On the other hand, figure 2.7(b) shows the hexagonal unit cell and its corresponding spin coupling, representing A_2BO_3 layered compounds. As shown in the above equation, the $S_i^x S_j^x$ ($S_i^y S_j^y$ or $S_i^z S_j^z$) term describes the spin coupling as in the Kitaev model [7].

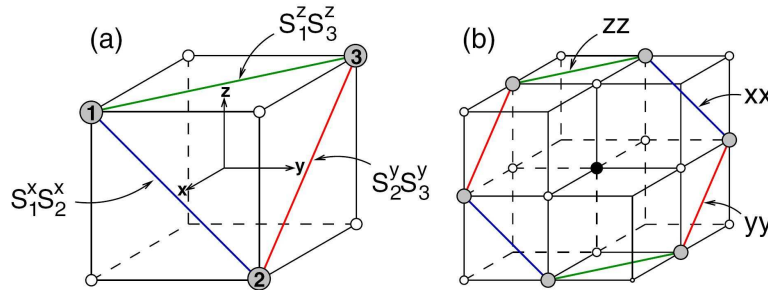


Figure 2.7: The patterns of the structure unit cells and their spin-coupling. (a) Triangular and (b) hexagonal unit cells [7].

Honeycomb iridates Na_2IrO_3 and Li_2IrO_3 are the best candidates of the Kitaev model. Such as for Na_2IrO_3 , the spin-orbit coupling can result in the anisotropic exchange interaction, i.e., the Kitaev coupling. However the existence of other interaction of the real materials can lead to the competition between the Heisenberg term (isotropy) and the Kitaev term (anisotropy). The Heisenberg-Kitaev model can be expressed as,

$$H = (1 - \alpha) \sum_{ij} \sigma_i \cdot \sigma_j - 2\alpha \sum_{\gamma} \sigma_i^{\gamma} \sigma_j^{\gamma}, \quad (2.33)$$

where α is the relative coupling between the Heisenberg term and the Kitaev term. $0 \leq \alpha \leq 0.4$ is the case for antiferromagnet, $0.4 \leq \alpha \leq 0.8$ is for stripy antiferromagnetism, and $0.8 \leq \alpha \leq 1$ is for the spin-liquid state.

2.3.2 Ruddlesden-Popper Series of Iridates

Perovskites have drawn more attention due to their unusual physical phenomena. $3d$ Ruddlesden-Popper series show many interesting behaviors such as superconductivity and ferroelectricity. Recently more attention is focused on $5d$ Ruddlesden-Popper series due to their similar structure. The general formula is ABO_3 , such as SrIrO_3 , in which the Ir^{4+} ions are surrounded by 6

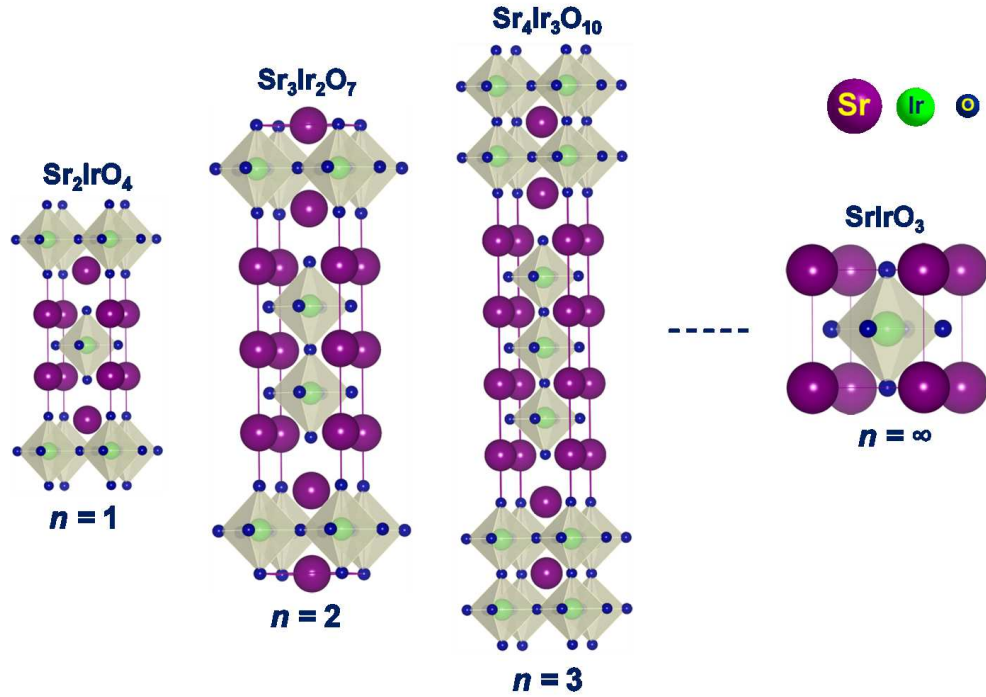


Figure 2.8: The Ruddlesden-Popper series of $\text{Sr}_{n+1}\text{Ir}_n\text{O}_{3n+1}$, cited from [8].

O^{2-} ions forming IrO_6 octahedra. On the other hand, stacked ABO_3 layers form the layered

Chapter 2. Physics of Transition Metal Compounds

perovskites, so called Ruddlesden-Popper series. The general formula is $A_{n+1}B_nO_{3n+1}$, in which n is the number of the octahedral layers. Ruddlesden-Popper series describe the change of dimensionality from 2D to 3D in the structure, as shown in Figure 2.8.

As described before, Sr_2IrO_4 ($n=1$) is an Ir-based compounds with the layered perovskite structure, showing insulating behavior with weak ferromagnetism [40, 3, 44, 45]. The strong spin-orbit coupling explained the novel $J_{eff} = 1/2$ Mott insulating ground state. Sr_2IrO_4 shows canted AFM behavior below 240 K with a small FM moment. For $Sr_3Ir_2O_7$ ($n=2$), the crystal structure is tetragonal with the space group $I4/mmm$ [35, 46]. Instead of the single layer of Ir-O octahedra in Sr_2IrO_4 , $Sr_3Ir_2O_7$ consists of Ir-O octahedra bilayers separated by Sr-O layer. The weak ferromagnetic behavior of $Sr_3Ir_2O_7$ was observed below 285 K and had strong octahedra rotation dependence. The insulating state could be changed easily by doping, physical pressure and magnetic field. $Sr_3Ir_2O_7$ is a very typical example to study the novel Mott states near the insulator-to-metal transition boundary. $SrIrO_3$ is the $n = \infty$ compound. It is a three dimensional system and shows semi-metallic behavior with a narrow band, which is different from Sr_2IrO_4 and $Sr_3Ir_2O_7$. Figure 2.9 shows the evolution of the band gap of $Sr_{n+1}Ir_nO_{3n+1}$ ($n = 1, 2, \infty$), which explains their rich physical behaviors, such as the insulating behavior, insulator-to-metal transition or correlated metallic behavior.

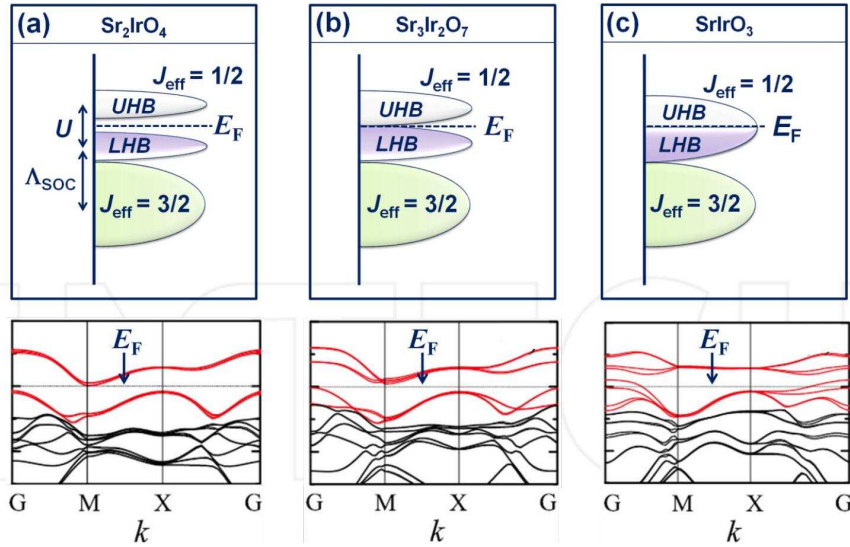


Figure 2.9: The band structure of Ruddlesden-Popper series of $Sr_{n+1}Ir_nO_{3n+1}$ ($n = 1, 2, \infty$), cited from [8] and [9].

2.3.3 6H Hexagonal Iridates

Doi et al. reported a series of 6H hexagonal Iridates $Ba_3MIr_2O_9$ ($M = Y, Mg, Ca, Sc, Ti, Zn, Sr, Zr$ and In) which adopt the 6H hexagonal perovskite type structure with space group

$P6_3/mmc$ [47]. Two IrO_6 octahedra share the face and form Ir_2O_9 dimers. On the other hand, Ir ions form triangular lattice, as shown in Figure 2.10. This series of iridates show interesting phenomenon.

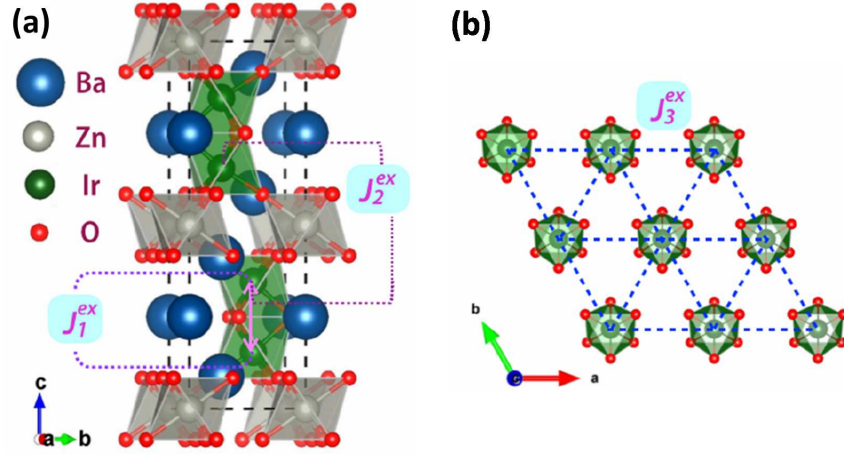


Figure 2.10: (a) The crystal structure of $\text{Ba}_3\text{ZnIr}_2\text{O}_9$; (b) Ir ions form triangular lattice, cited from [10].

One example is $\text{Ba}_3\text{YIr}_2\text{O}_9$ [48], which crystallizes in a hexagonal structure and transforms into a cubic structure under 8 GPa at 1273 K, strong spin orbit coupling (SOC) plays an important role in determining the magnetic and insulating behaviors in both phases. The ambient pressure sample shows magnetic transition around 4 K and the high pressure sample shows no magnetic order. The high pressure cubic phase of $\text{Ba}_3\text{YIr}_2\text{O}_9$ is suggested to be a spin-liquid iridate.

Recent studies also have been focused on new iridate compounds where experimental discoveries have strongly challenged theoretical predictions. For example, in pentavalent (Ir^{5+}) $5d^4$ iridates a strong SOC is predicted to realize a nonmagnetic $J = 0$ state [49], but substantial magnetic moments have been found in Ba_2YIrO_6 [50] and especially in Sr_2YIrO_6 [51], where structural distortion of the octahedral environment leads to $0.91 \mu_B/\text{Ir}$. Furthermore, a possible realization of a spin-orbital liquid with Ir^{5+} has been discussed for $6H$ hexagonal $\text{Ba}_3\text{ZnIr}_2\text{O}_9$ powder [10].

3 Experimental Techniques

3.1 Samples Synthesis

In material science field, it is very important to synthesize new materials and high quality crystals. Crystal growth is a crystallization process following homogeneous or heterogeneous nucleation to form a solid material whose atoms are orderly arranged in all three dimensions. Considering the involved phase, crystal growth processes are divided into four categories:

1. Solid growth. The process involves solid-solid phase transition and is controlled by atomic diffusion.
2. Melt growth. Liquid-solid phase transition is related into this category, which is the most popular synthesis method for large single crystals.
3. Solution growth. The liquid-solid phase transition is also related into this category, in which the crystals are grown from solvents, generally using a molten metal called the flux for high temperature processes.
4. Vapor growth. The process is involving vapor-solid phase transition.

In this study the solid-state reaction method is used for polycrystalline sample growth and the flux method is used for single crystal sample synthesis. Flux growth is widely used to produce single crystals of superconductors like $\text{YBa}_2\text{Cu}_3\text{O}_{7-x}$ [52], BaFe_2As_2 [53] and Iridates [54].

3.1.1 Solid-state Reaction method

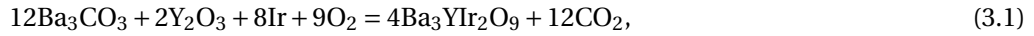
The solid-state reaction method is the most widely used method for the synthesis of polycrystalline samples. The reaction starts from a mixture of raw materials and occurs at higher temperatures. In the case of $\text{Ba}_3\text{YIr}_2\text{O}_9$, the samples were synthesized by solid-state reaction.

Chapter 3. Experimental Techniques

Table 3.1: Classification of crystal growth processes, cited from [25].

| | | | |
|--------------------------|-----------------------|------------------------------|--|
| 1. Solid-Solid | Solid | \xrightarrow{T} | Solid Devitrification Strain annealing Polymorphic phase change Precipitation from solid Solution |
| 2. Liquid-Solid | | | |
| (i) Melt Growth | Molten Material | $\xrightarrow{dec.T}$ | Crystal Bridgman-Stockbarger Kyropoulos Czochralski Zoning Verneuil |
| (ii) Flux Growth | Solid + Flux Agent | $\xrightarrow{dec.T}$ | Crystal |
| (iii) Solution Growth | Solid + Solvent | \xrightarrow{lowT} | Crystal Evaporation Slow cooling Boiling solutions |
| (iv) Hydrothermal Growth | Solid + Solvents | $\xrightarrow{high.T,highP}$ | Crystal Hydrothermal sintering Hydrothermal reactions Normal temperature gradient Reversed temperature gradient |
| (v) Gel growth | Solution + Gel medium | \xrightarrow{lowT} | Crystal Reaction Complex decomplex Chemical reduction Solubility reduction Counter-flow diffusion Crystal + products |
| 3. Gas-Solid | | | |
| | Vapour | \longrightarrow | Solid Sublimation-condensation Sputtering Epitaxial processes Ion-implantation |

The chemical reaction equation is that:



BaCO_3 , Y_2O_3 and Ir powders were used as raw materials. The mixture of the powders with the ratio of $\text{BaCO}_3 : \text{Ir} : \text{Y}_2\text{O}_3 = 12 : 9 : 2$ was pressed into pellets and heated for 12 h at 900 °C. After the reaction, the calcined materials were heated at 1100–1300 °C for 72–144 h in air atmosphere with several repeated grinding and pelleting processes [47]. Polycrystalline samples were also synthesized as starting materials for the single crystal growth experiments.

3.1.2 Flux method

The flux method is a high temperature solution growth method which is widely used in the single crystal growth field. The desired substances are dissolved in a solvent (flux). It

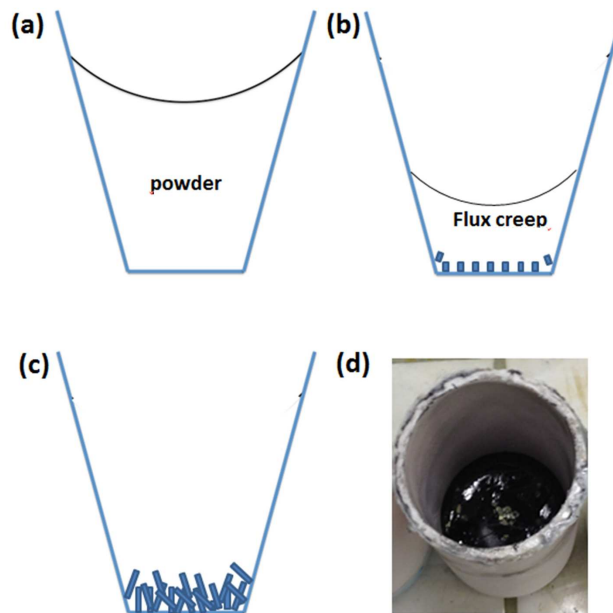


Figure 3.1: A schematic of the self-flux method: (a) powder of starting materials and flux in the alumina crucible, (b) the formation process of the single crystals during the cooling process, (c) the resultant single crystals after the crystal growth process, and (d) the picture of the crystals in the alumina crucible.

is important to choose a suitable flux which must not react with the solute to prevent from forming solid compounds. In flux method slow cooling of the solvent from homogeneous mass is employed and the crystallization occurs by spontaneous nucleation. The advantage of using a solvent is that the temperature for crystal growth is lower than that required for pure

melt growth. The growth process in the flux starts from forming the seeds which is used to grow single crystals. The resultant single crystals from flux method show a high quality.

In the case of Gd-doped Sr_2IrO_4 , the single crystals were synthesized by the flux method. $\text{SrCl}_2 \cdot 6\text{H}_2\text{O}$ was used as the flux and the raw materials Gd_2O_3 , IrO_2 and Sr_2O_3 were used as the solute. A mixture with the mass ratio of solute : solvent = 1:6 was heated for 24 h at 1300°C and cooled down to 1100°C at 8°C/h and then more slowly cooled down (2°C/h) to 900°C . The distilled water was used to separate the crystals from the solvent. [55]

3.2 Sample Characterization (X-ray and EDX)

After the single crystals synthesis, the first analyses should be the sample quality examinations. The x-ray diffraction and the energy dispersive x-ray (EDX) spectroscopy are used widely for structure determination and chemical composition determination, respectively.

3.2.1 Single Crystal X-ray Diffraction (XRD)

X-ray diffraction is a widely used technique for structure determination of crystalline materials. When an X-ray beam propagates through a crystal, the coherent scattering is the main source

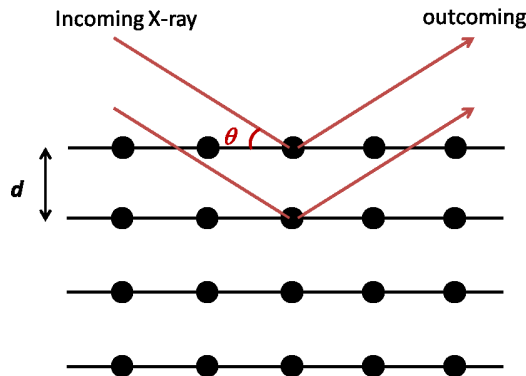


Figure 3.2: The description of Bragg's law for X-ray Diffraction.

for X-ray beam scattered from the periodically arranged lattices of crystal. X-rays can be represented as electromagnetic radiation waves, and crystals can be considered as regular arrays of atoms. Periodically arrayed scatterers produce a periodic array of spherical waves. Such waves cancel each other out through destructive interference in most directions and add constructively in several specific directions, which are expressed by Bragg's law:

$$2d \sin \theta = n\lambda, \quad (3.2)$$

3.2. Sample Characterization (X-ray and EDX)

where d is the interplanar spacing of the diffracting planes, θ is the angle between the incident and the diffracted beam, n is the order of diffraction which is an integer and λ is the wavelength. The representation of Bragg's law is shown in Figure 3.2 [56].

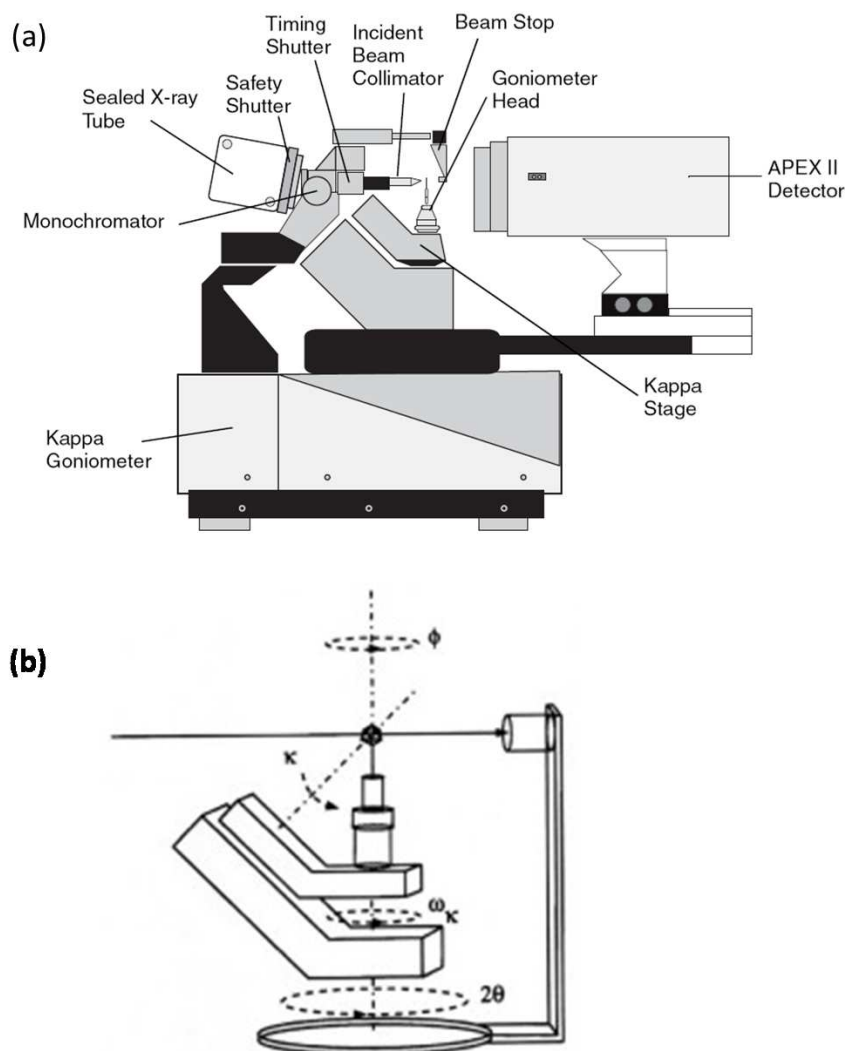


Figure 3.3: The appearance and scheme of a four-circle goniometer with Kappa geometry, cited from [11].

In this work, single crystal x-ray diffraction data were measured at room temperature and at low temperature (90 K) using Mo $K\alpha$ radiation on a Bruker APEX II CCD diffractometer equipped with a kappa goniometer. X-ray diffractometers are composed of an X-ray tube, a sample holder and a detector. In a cathode ray tube the electrons are generated by heating a filament. The electrons can be accelerated towards the target material and interact with the electrons of the target material. When the inner shell electrons of the target materials are ejected by the accelerated electrons with high energy, the characteristic X-rays are generated. $K\alpha$ is the most

common X-ray spectrum and Mo is widely used target material for single-crystal diffraction using Mo $K\alpha$ radiation with $\lambda = 0.71073 \text{ \AA}$. The selection of crystals for single crystal XRD can be performed by viewing the samples under crossed polars on a spectrographic microscope. The size of the crystals should be between 0.2 and 0.4 mm and equant crystals are preferred. The crystal with proper shape and size is mounted on the thin glass fiber using a grease. For our measurements, apiezon grease N was used. The crystal is centered by adjusting the orthogonal directions. Once the crystal centering is finished, the X-ray beams make a diffraction pattern of spots to the specific directions when they land on a detector. Single-crystal diffractometer uses a four circle Kappa goniometer which refers to the four angles (2θ , κ , ϕ and ω_κ), as shown in Figure 3.3. The goniometer axes rotate and a rotational image is often taken to check the

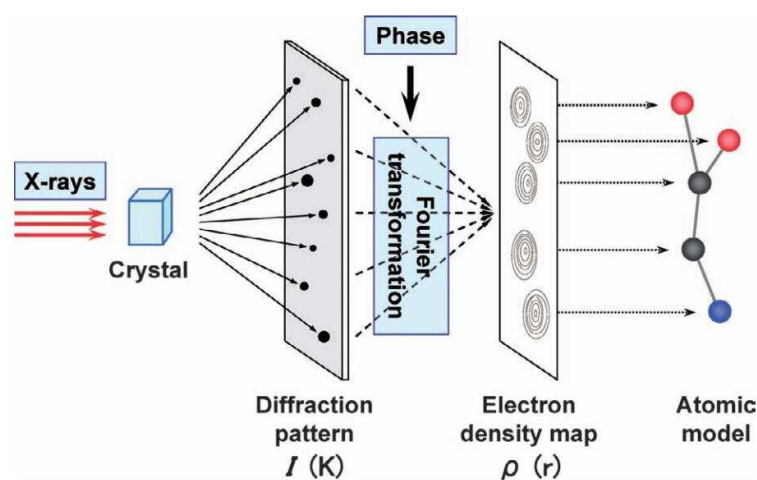


Figure 3.4: Summary of single crystal XRD technique, cited from [12].

sample quality and lattice parameters. The different X-ray reflection patterns from the crystals are captured by the Charge-Coupled Device (CCD) image sensor. Afterwards, the dataset was firstly reduced by EvalCCD and then rectified for absorption [57, 58]. The reflection pattern can be used to extract the information about the atomic coordinates and composition to perform structure analysis. After the data have been collected, the solution of the phase problem should be the main task for later step. The solution and refinement were performed by SHELX [59], using full-matrix least-squares based on F^2 [12]. The initial electron density map is produced from the solution of the phase problem. During refinement calculation and from the initial electron density map, many of the crystal structure information such as atomic coordinates, sites occupancy, types of chemical bonds and atomic distances can be determined to result in a structure model [60]. Solution quality is evaluated by the values of R_1 , wR_2 and Goodness-of-fit, in which, R_1 is the agreement between the observed and the calculated results and wR_2 refers to squared F -values. The summary of single crystal X-ray diffraction technique is described in Figure 3.4.

3.2.2 Energy Dispersive X-ray (EDX) spectroscopy

As an analytical methodology, scanning electron microscope (SEM) and energy-dispersive x-ray (EDX) spectroscopy can be used to perform the elemental analysis or to characterize the chemical property of a sample. The SEM can be used to determine the shape information of the crystals. The mechanism of EDX relies on the detection of characteristic x-rays from an excited spot of the samples using a high energy beam of charged particles such as a beam of electrons.

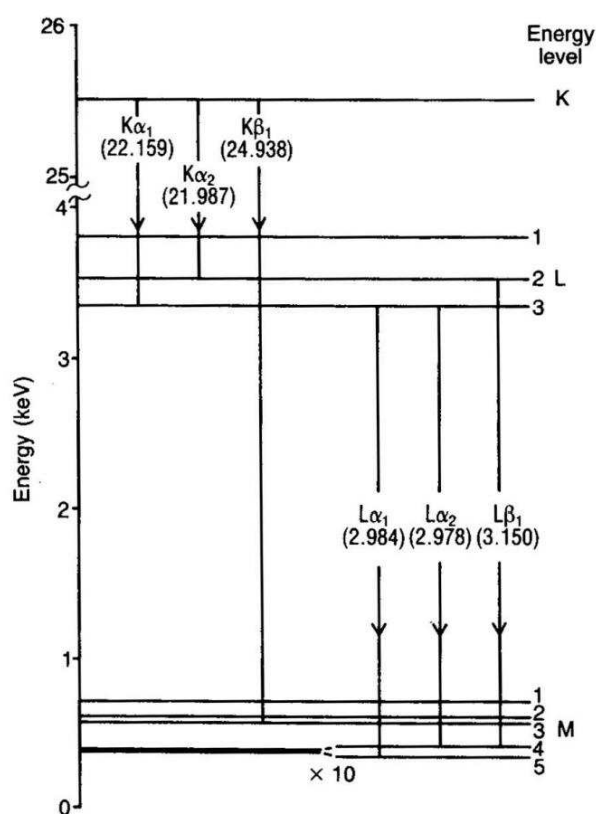


Figure 3.5: The diagram of energy level for Ag, cited from [13].

The lines in the spectrum will be identified in the analysis which is quite simple because of the simplicity of X-ray spectrum. Generally, most of the elements in the periodic table can be identified except the ones lighter than boron. A beam of electrons may eject an electron from an atom of the sample, where then a vacancy is created. After that the electron shells are reconfigured to minimize the energy. During this process the energy difference between the higher and lower energy shell can be released as an X-ray, as shown in Figure 3.5. The X-ray has an energy characterizing a specific atom that generated it. The number and energy of these fingerprint X-rays can be measured by an EDX detector. As most of elements have characteristic X-ray fingerprints with unique energy, EDX allows the measurement of the

elemental composition.

For example, the chemical composition of the resulting compound $\text{Ba}_8\text{Al}_2\text{IrO}_{14}$ was determined using an Energy Dispersive X-Ray detector (EDX, Oxford Instruments EDX X-MAX). The EDX analysis revealed the presence of Ba, Ir, and Al.

3.3 Transport Measurement

3.3.1 Electrical Resistivity Measurement

Electrical conductivity is the measurement of the ability of a material to allow charges to flow after applying an electric field on the material. It could be expressed by:

$$\sigma = j/E \quad (3.3)$$

$$j = nqv \quad (3.4)$$

where σ is the electrical conductivity, j is the flux of charge carriers, E is the applied electric field or the potential gradient, n is the number density of the charges, v is the drift velocity of the charges and q is the charge on each of the carriers [61].

Experimentally, the electrical resistivity ρ is usually measured to obtain the electrical conductivity. Electrical resistivity is the reciprocal of electrical conductivity and defined by

$$\rho = 1/\sigma = E/j \quad (3.5)$$

Various methods have been used to measure the electrical resistivity. Among them two-probe method can be used for higher resistivity samples and four-probe method for the lower resistivity samples and single crystals. In this study, four-probe method is used (Figure 3.6). Comparing to the two-probe method, four-probe method can ignore the contact resistance

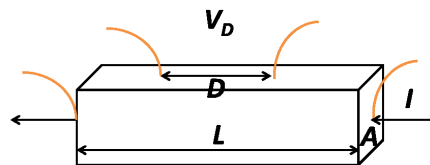


Figure 3.6: Electrical resistance measurement by four probe method.

effects and therefore is used for lower resistivity measurements. The instrumentation includes a DC current source, a sensitive voltmeter, and a four point collinear probe. A controlled

DC current I is forced between the outer two probes and can be sourced by the Keithley model 2400 or Keithley model 6221. A voltmeter Keithley model 2182 measures the voltage difference V_D between the inner two probes. The resistivity is determined from geometric factors of the sample, the source current and the voltage measurement [62]. For this method the voltage drop is measured across two probes D instead of the sample length L , and the value of electrical resistivity is determined by:

$$\rho = \frac{V_D A}{DI} \quad (3.6)$$

in which A is the cross sectional area.

3.3.2 Seebeck Coefficient Measurement

The Seebeck effect or the thermoelectric effect describes a phenomenon that a temperature difference between two electrical conductors or semiconductors produces a voltage difference between the two substances. Therefore, a thermoelectric material possesses the ability to transfer thermal energy into electrical energy.

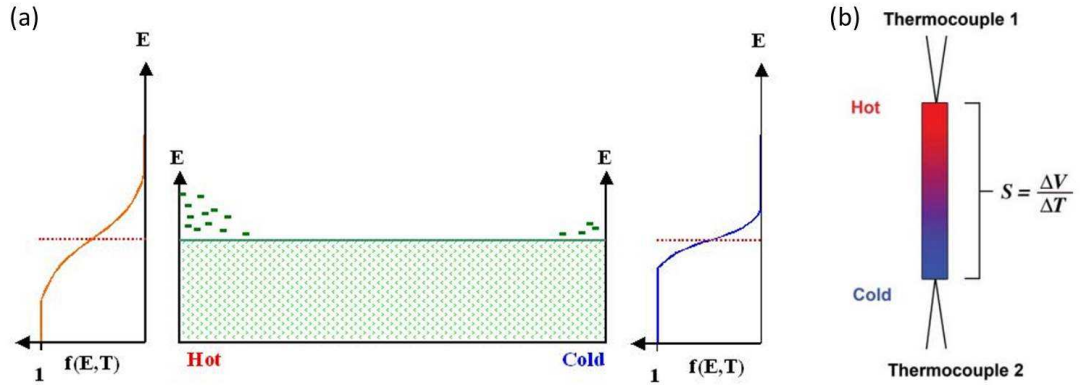


Figure 3.7: (a) Schematic of the Seebeck effect, which explains that a temperature gradient causes a potential difference. (b) Ideal Seebeck coefficient measurement geometry, with thermocouples making small point contacts, cited from [14].

As shown in Figure 3.7, when one end of a thermoelectric material was heated, the electrons start moving away from the hot toward the cold end. The electrons at the hot end acquire increased energy and tend to flow to the cold end. Consequently, an electrical potential difference ΔV is therefore developed. The potential difference ΔV across a material caused by a temperature difference ΔT is called the Seebeck effect. The Seebeck coefficient represents

Chapter 3. Experimental Techniques

the magnitude of an induced thermoelectric voltage caused by a temperature difference, i.e.

$$S = \frac{\Delta V}{\Delta T} \quad (3.7)$$

The unit of the Seebeck coefficient S is $\mu\text{V/K}$ with positive or negative values depending on the charge carrier type of holes or electrons.

The average energy E_{av} per electron is given by

$$E_{av}(T) = \frac{3}{5}E_{FO} \left[1 + \frac{5\pi^2}{12} \left(\frac{kT}{E_{FO}} \right)^2 \right] \quad (3.8)$$

where E_{FO} is the Fermi energy at 0 K. The Fermi-Dirac distribution extends to much higher energies at hot end, as shown in Figure 3.7(a), so that more electrons in the hot end diffuse toward the cold end until a potential difference ΔV is produced to prevent further diffusion.

The electrons are dominant charge carriers in a n -type semiconductor. The internal built electrical field is opposite to the temperature gradient, and a negative sign of S is assigned for Seebeck coefficient. In a p -type semiconductor, on the other hand, the holes are dominant charge carriers which would make S a positive quantity [63].

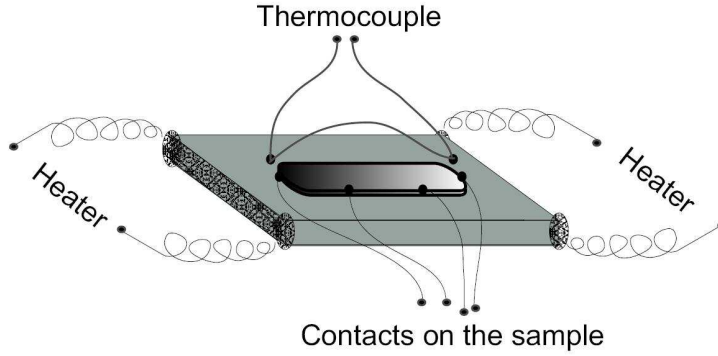


Figure 3.8: Line drawing of the arrangement used in Seebeck measurements, cited from [15]

To measure thermoelectric power S the sample was placed on a ceramic bar, at one end of which a small heater was anchored in order to generate heat which was sent through the crystal, i.e., one end is heated while the other end acts as a heat sink, cooling that side. The temperature gradient ΔT was measured by a differential Chromel-Constantan (type E) thermocouple, which is placed on the ceramic bar. The temperature difference was kept at 1 K for all temperatures. This change in temperature produces a detectable voltage drop. The thermal voltage ΔV of the sample was measured by two gold wires glued to the sample,

essentially in a differential thermocouple configuration Au-sample-Au. Seebeck coefficient can be evaluated in the 5–600 K temperature range.

3.3.3 Resistivity under Pressure

External pressure is used to tune the interaction of different energy scales of the strongly correlated materials, making it possible to continuously increase a material's bandwidths through decreasing its lattice constant. While the overlap integral depends exponentially on the distance of the neighboring atoms, the on-site electron-electron interaction is insensitive of it. As a result, the systems are usually driven towards a more delocalized state by the application of pressure. The most common pressure cells in use now are the piston cylinder cells which can generate and sustain pressures up to 3 GPa and the diamond anvil cells with a maximum pressure in the range of hundreds of GPa. In this study, we use the piston cylinder cells.

The cross-sectional view of a piston-cylinder pressure cell can be seen in Figure 3.9. The piston cylinder cell uses a piston to compress a Teflon cup, which is fully filled with kerosene as the pressure medium and is used to cover the sample. The preparation of the feedthrough is very important. It is used for connecting closely with the Teflon cup to prevent the flowing over of the pressure medium in the Teflon cup. The feedthrough is sealed with black Stycast (2850 FT) which serves as pressure proof insulation of the pressurized cell. The outer shell of the cell body is made of a non-magnetic, hard alloy, such as Be-Cu and the inner shell is made of MP35N. The anti-extrusion sealing rings, made of steel or Be-Cu, are placed above and below the Teflon cup. While under pressure, this prevents the Teflon from flowing through the interstices and causing breaks in the liquid-tight seal. Pressure is increased by applying a load to the piston. The piston touches the teflon cap directly and can be pressed by a rod which is put into the hole of the upper locking nut. Then, the pressure is locked into place by tightening the upper locking nut. The feedthrough provides an access for the electrical leads that connect the sample and other components within the sample space to the outside.

A piston-cylinder pressure cell enables a few samples to be measured at the same time. Figure 3.10 presents a general setup for two samples and lead. To estimate the pressure inside the pressure cell requires more precise pressure gauges such as lead to be installed close to the sample since its rough estimation with applied pressure is not accurate enough. The pressure at low temperatures can be determined by a widely applied technique using some metals such as lead, tin, and indium which are strong pressure dependence of the superconducting transition temperatures (T_c) of [64, 65].

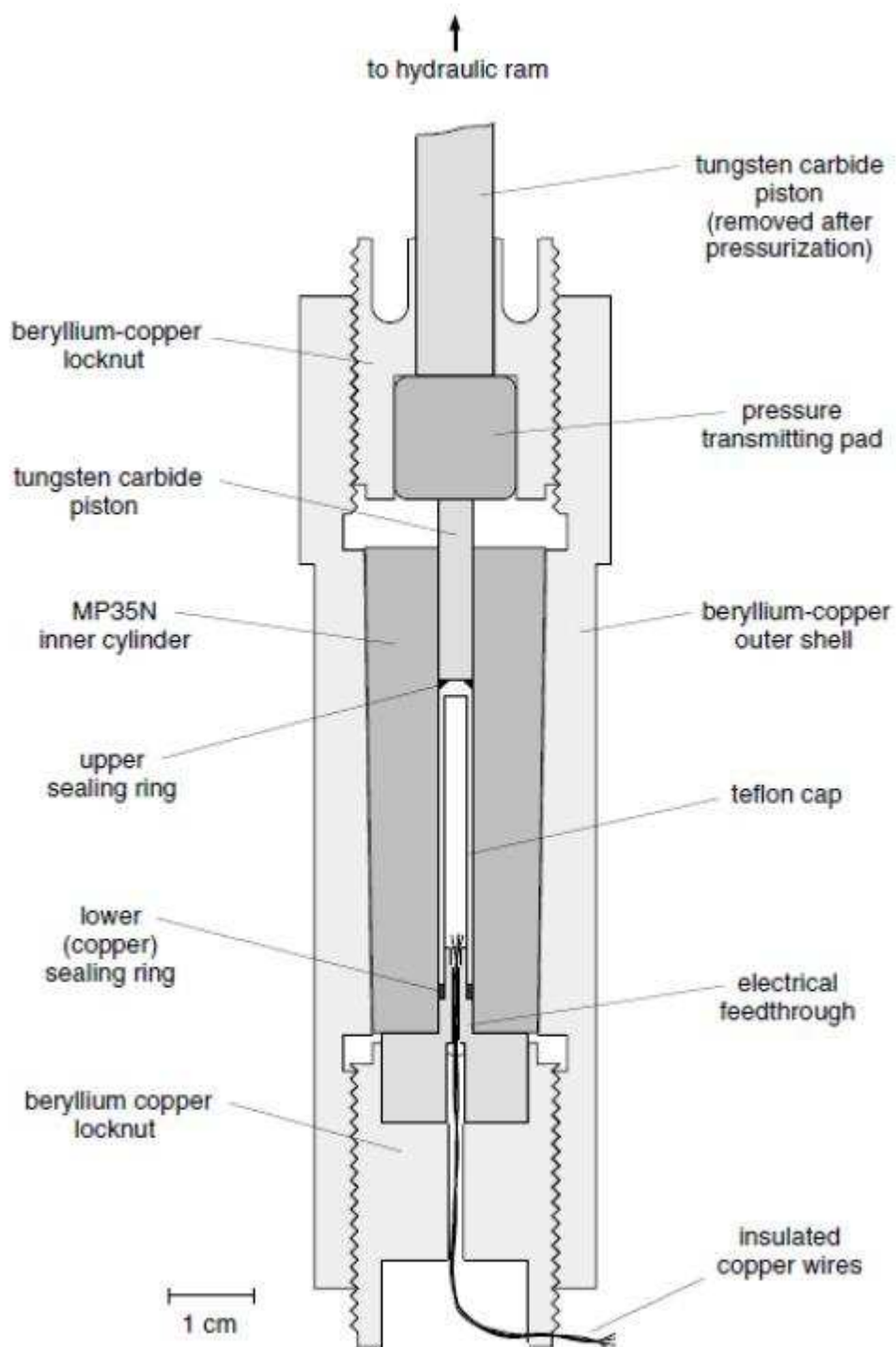


Figure 3.9: Schematic of a piston-cylinder pressure cell, cited from [16].



Figure 3.10: Feedthrough for a typical piston-cylinder pressure cell with sample board, cited from [17].

3.4 DC Magnetometry

A Superconducting Quantum Interference Device (SQUID) is the most sensitive device for magnetic fields measurement. In this work the bulk magnetic measurement were performed with Quantum Design's Magnetic Property Measurement System (MPMS). The designation of MPMS uses the flux magnetometer method, in which SQUID is used for the detection of the magnetic field lines "flux" and its change when magnetic sample is pulled through the coils. The schematics of SQUID magnetometer are described in Figure 3.11 [18, 66].

A change of the magnetic flux through the SQUID loop causes a change in the voltage which is sensed by electronics. The voltage provides a feedback current which is applied to the feedback coil to maintain a constant flux in the SQUID. This feedback current, determined by the feedback resistor, is a direct measurement of the changes in the magnetic flux. By coupling the feedback signal to input coil, the flux could be obtained from a sample to the SQUID inside the shielded environment.

According to the Faraday's law of induction, one can obtain

$$V_{ind} \propto \partial\Phi/\partial t, \quad (3.9)$$

in which, V_{ind} is the voltage induced and Φ is the magnetic flux. By applying a magnetic field,

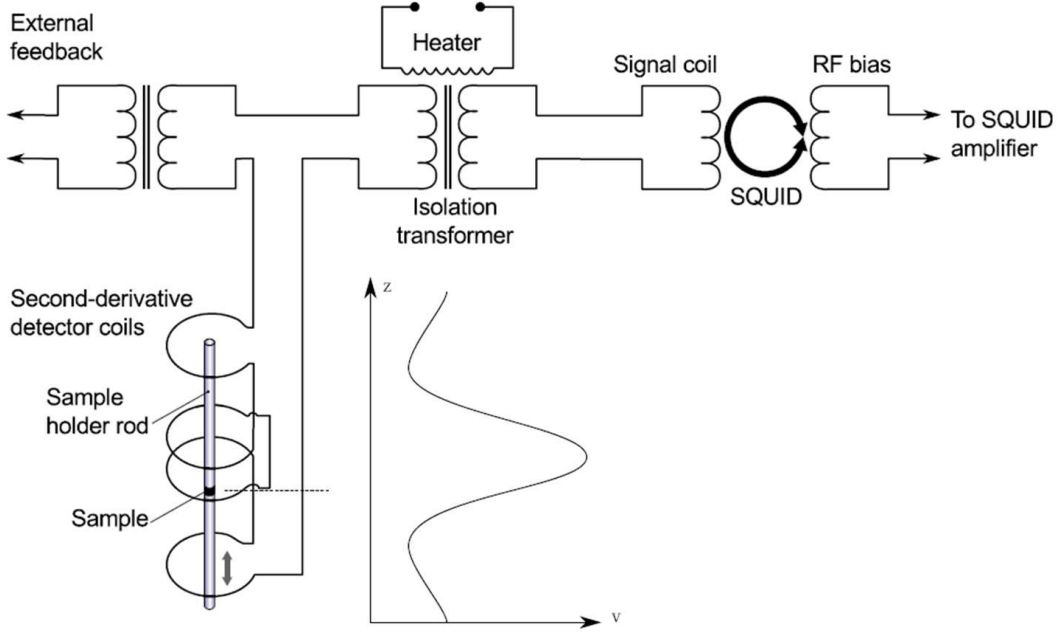


Figure 3.11: Schematics of SQUID magnetometer with longitudinal detection coils, cited from [18].

dc susceptibility can be expressed by

$$\chi_{dc} = M/H, \quad (3.10)$$

where χ_{dc} is the dc susceptibility, M is the magnetization and H is an external magnetic field.

Similar as the hydrostatic piston-cylinder type pressure cell for the resistivity measurements, the piston-cylinder of pressure cell for the magnetization measurements is shown in Figure 3.12. The size of the Cu-Be cell for magnetization measurements depends on the sample space of the SQUID magnetometer. The maximum pressure that can be safely generated is about 1.2 GPa. Pressure is determined at low temperature by the shift of the superconducting transition temperature T_c of Sn or Pb [67], which is placed at the bottom of the cell. More details of the construction together with functional and destruction tests can be found in [68].

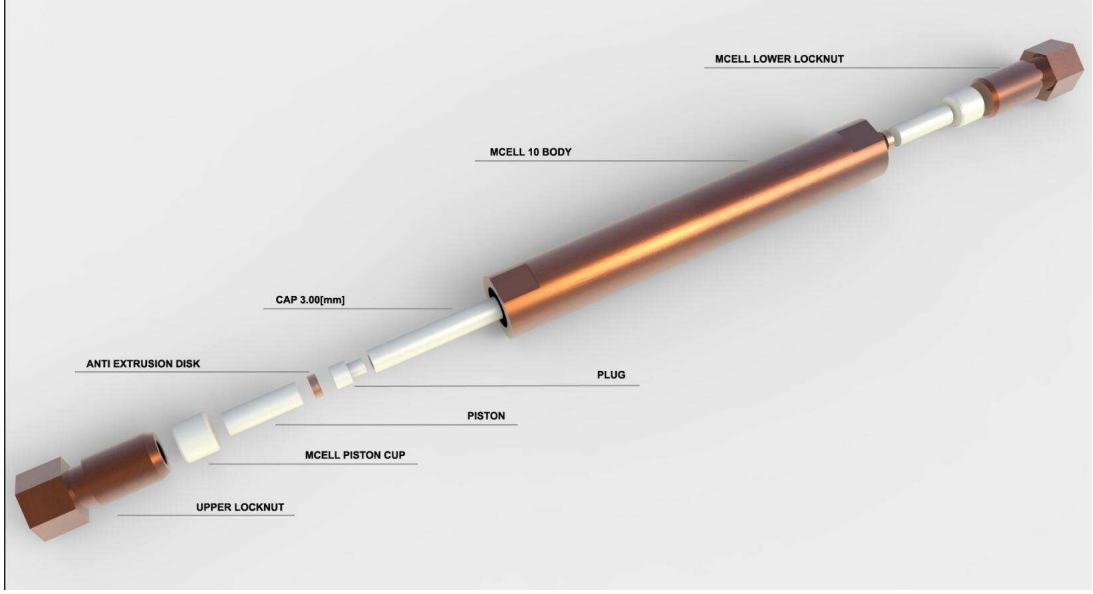


Figure 3.12: Hydrostatic piston-cylinder type pressure cell for the magnetization measurements in the MPMS SQUID magnetometer, cited from [19].

3.5 Heat Capacity Measurement

Many important informations such as the lattice, magnetic and electronic states of materials are obtained from the heat capacity measurement, in which heat pulse method and AC heat capacity measurement are the most common methods. The total specific heat can be expressed by

$$C_p = C_{el} + C_{ph} + C_{mag} + \dots, \quad (3.11)$$

In this work, we are using the Quantum Design (QD) PPMS (heat pulse method) to measure the heat capacity, which is in practice measured as a change of heat dQ by changing the temperature of dT at a constant pressure p

$$C_p = (dQ/dT)_p, \quad (3.12)$$

Schematics of PPMS Heat Capacity Option are described in Figure 3.13. The sample is mounted onto the platform by using Apiezon Grease. At the bottom of the platform, a thermometer and heater are attached, as shown in Figure 3.13 (a) and (b). During the measurement process, the change of sample temperature vs. time is shown in Figure 3.13 (c). A known quantity of heat

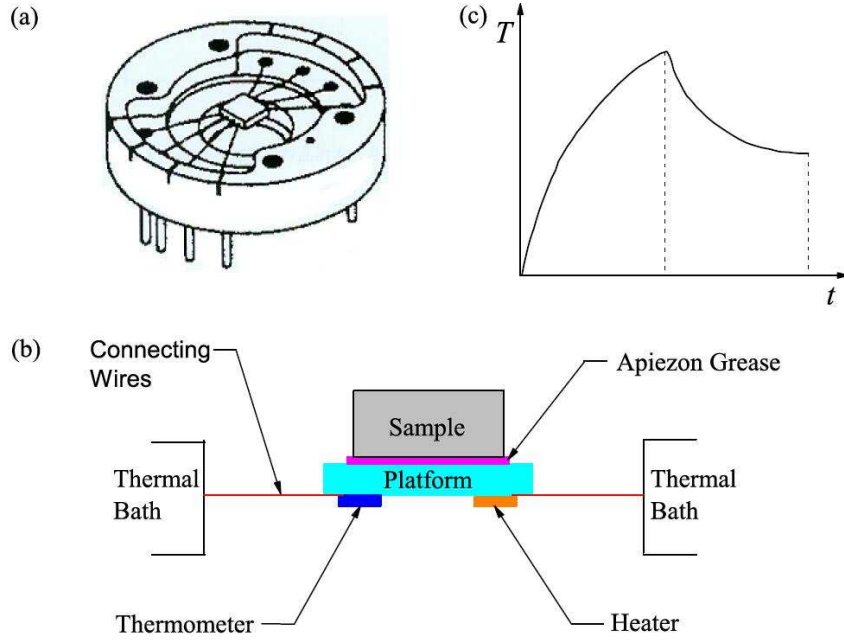


Figure 3.13: Schematics of PPMS Heat Capacity Option. (a) and (b) Thermal connection to the sample and sample platform, (c) Temperature change vs. time induced by a pulse of heat, cited from [20, 21].

is first applied to the sample through the heater which is corresponding to the temperature increasing process. After this heat pulse, the temperature decreases exponentially. For the whole heating-cooling cycle, the heat conduction process can be expressed by the simple model, in which an ideal thermal contact between the sample and the platform is assumed,

$$C_{tot} \frac{dT}{dt} = -\lambda_w(T - T_b) + P(t), \quad (3.13)$$

in which C_{tot} is the total heat capacity of the sample and platform, λ_w is the thermal conductance of the wires connecting platform, T is the temperature of sample and platform, T_b is the temperature of holder frame and $P(t)$ is the power of heater. However in practice, it is difficult to achieve an ideal thermal contact between the platform and sample therefore the thermal conductivity between the platform and the sample due to the grease λ_g has to be considered. The above process can be expressed as two parts, the so called Two-Tau model,

$$C_{pl} \frac{dT_{pl}}{dt} = -\lambda_w(T_{pl}(t) - T_b) + \lambda_g(T_s(t) - T_{pl}(t)) + P(t), \quad (3.14)$$

$$C_s \frac{dT_s}{dt} = \lambda_g (T_s(t) - T_{pl}(t)), \quad (3.15)$$

in which C_{pl} is the heat capacity of the platform, C_s is the heat capacity of the sample, T_{pl} is the temperature of the platform, T_s is the temperature of the sample.

Based on the above equations, one can obtain

$$\tau_1 = \frac{1}{\alpha - \beta}, \quad (3.16)$$

$$\tau_2 = \frac{1}{\alpha + \beta}, \quad (3.17)$$

$$\alpha = \frac{\lambda_w}{2C_{pl}} + \frac{\lambda_g}{2C_{pl}} + \frac{\lambda_g}{2C_s}, \quad (3.18)$$

$$\beta = \frac{\sqrt{C_s^2(\lambda_w + \lambda_g)^2 + 2C_s C_{pl}(\lambda_g^2 - \lambda_w \lambda_g) + C_{pl}^2 \lambda_g^2}}{2C_{pl} C_s}, \quad (3.19)$$

The heat capacity option of the QD PPMS is based on the above Two-Tau model. The measurement can be carried out within the temperature range of 1.8 to 400 K and in applied magnetic field up to 9 T.

4 Synthesis, Structure, Transport and Magnetic Properties of 5d Transition Metal Compounds—Iridates

The results of this chapter are partly copies from the three papers below [69, 70]: Lin Yang, Andrea Pisoni, Arnaud Magrez, et al, Crystal Structure, Transport, and Magnetic Properties of an Ir⁶⁺ Compound Ba₈Al₂IrO₁₄, Inorg. Chem., 2015, 54 (9), pp 4371–4376

L. Yang, M. Jeong, A. Arakcheeva, et al, Possible unusual spin state of Ir⁴⁺ in Ba₂₁Ir₉O₄₃ single crystal, Phys. Rev. B 2016, 94, pp 104403

L. Yang, O. Ivashko, D. Destraz, et al, Pressure induced two-dimensional superconductivity and Ir-dimerization in Ir_{0.95}Pt_{0.05}Te₂, in preparation.

4.1 Novel Ir⁶⁺ System Ba₈Al₂IrO₁₄

4.1.1 Motivation for This Work

Recently, there has been more and more interest in studying correlated 5*d*-electron transition metal compounds. Compared to 3*d* transition metal compounds, 5*d* materials were expected to be less correlated due to their extended orbitals. Therefore, a tendency to metallic behavior was expected. However, experiments have shown that some compounds, such as Sr₃Ir₂O₇ and Na₂IrO₃, show insulating behavior [35, 36, 37]. Some recent reports show that correlation effects become more important for the 5*d* transition metal oxides [38, 39, 40]. One example is Ba₃YIr₂O₉ [48], which crystallizes in a hexagonal structure and transforms into a cubic structure under 8 GPa at 1273 K, strong spin orbit coupling (SOC) plays a crucial role in determining the magnetic and insulating states of this system in both phases. Iridium-based oxides are relatively unexplored. In the majority of Iridium-based compounds Ir⁴⁺ is stabilized and recently most of theoretical and experimental work have focused on the tetravalent iridates (Ir⁴⁺). On the other hand, Ir⁵⁺ and Ir⁶⁺ can also be obtained under high oxygen pressure conditions but little attention has been drawn to them [71, 72, 73, 74, 75]. In this work we show the ambient-pressure synthesis and physical properties of a new all-Ir⁶⁺ iridate Ba₈Al₂IrO₁₄.

Chapter 4. Synthesis, Structure, Transport and Magnetic Properties of 5d Transition Metal Compounds—Iridates

The preparation of all- Ir^{6+} iridate without using traditional high-pressure techniques has to our knowledge previously only been reported in $\text{Nd}_2\text{K}_2\text{O}_7$ and $\text{Sm}_2\text{K}_2\text{O}_7$ [76].

4.1.2 Synthesis and Crystal Structure

Single crystals of $\text{Ba}_8\text{Al}_2\text{IrO}_{14}$ were grown as unexpected byproducts in our attempt to synthesize $\text{Ba}_3\text{YIr}_2\text{O}_9$ single crystals. In this process, single crystals of $\text{Ba}_8\text{Al}_2\text{IrO}_{14}$ were produced by reacting BaCO_3 , IrO_2 and Y_2O_3 powder by self-flux method in Al_2O_3 crucible. The mixture of the powders with the ratio of $\text{BaCO}_3 : \text{IrO}_2 : \text{Y}_2\text{O}_3 = 26 : 4 : 1$ was heated for 2 h at 1250°C , and rapidly cooled down to room temperature. After the reaction, small black single crystals were found with a needle like shape. The maximum dimensions were 0.5 mm in length and 0.1 mm in width (Figure 4.1). The needle axes coincide with the crystallographic b -axis. Grinding the black crystals produced brown power. The crystals are very sensitive to moisture. The chemical composition of the resulting compound was determined using EDX. The EDX analysis revealed the presence of Ba, Ir, and Al. We conclude that the raw materials reacted with the Al_2O_3 crucible to acquire Al. This conclusion was supported by inspection of the crucible after reaction, where the crystals could be seen to grow in needles away from the crucible wall. The EDX analysis suggested molar ratios Ba:Al:Ir of 79.87(64):10.47(98):9.66(46), but for these numbers the low EDX efficiency for the light element Al must be taken into account, as shown in Figure 4.2.

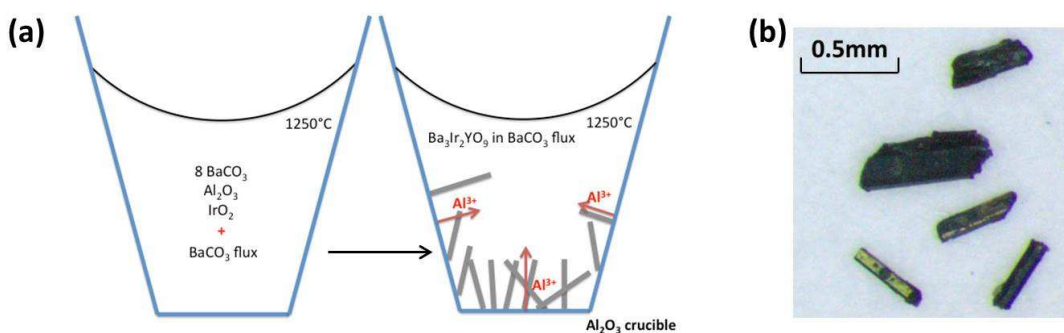
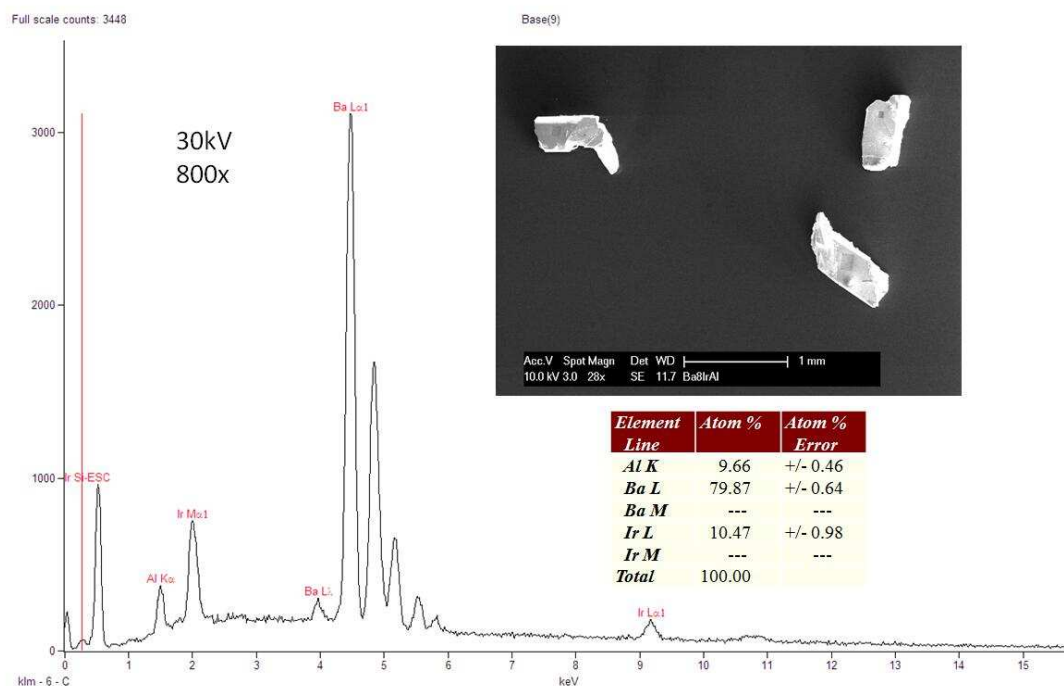


Figure 4.1: (a) A schematic of the crystal growth process with the flux method. (b) Representative single crystals of $\text{Ba}_8\text{Al}_2\text{IrO}_{14}$.

S. Katrych and A. Arakcheeva had determined the crystal structure of the novel iridate $\text{Ba}_8\text{Al}_2\text{IrO}_{14}$ [69]. Single-crystal x-ray diffraction (XRD) data were measured at room temperature and low temperature (90 K).

According to the systematic absences of the XRD reflections, the space groups $C2/m$, Cm and $C2$ can be suggested. The structure refinements have been performed for all these space groups and finalized with nearly the same reliability factor $R1 \sim 0.04$. Therefore, the highest

Figure 4.2: (a) X-ray EDS analysis performed on Ba₈Al₂IrO₁₄.

symmetric space group, $C2/m$ (No.12) has been selected.

The lattice parameters were determined as $a = 19.8367(14)$, $b = 5.9709(6)$, $c = 7.6138(7)$ Å, $\alpha = \gamma = 90^\circ$ and $\beta = 109.785(5)^\circ$. The longest size of the needle like crystals coincides with the b -axis. Further details of the data collection, structure determination and refinement are listed in Tables 4.1-4.4. The crystal structure of Ba₈Al₂IrO₁₄ is shown in Figure 4.2, where the IrO₆ octahedra and AlO₄ tetrahedra are outlined. The crystal structure of Ba₈Al₂IrO₁₄ is related to Sr₈Si₂PtO₁₄, reported in Ref. [77] with asymmetric space group $C2$ (No.5), $a = 18.830(2)$, $b = 5.744(1)$, $c = 7.172(1)$ Å, $\beta = 110.72(1)^\circ$. Both structures contain identical number, 50, of atoms per similar unit cell, and they can be described with the same type of cationic polyhedra (Figure 4.2). Isolated AlO₄ tetrahedra and IrO₆ octahedra are separated by Ba ions. The IrO₆ octahedra are slightly distorted with two 2.041(7) Å long and four 1.970(5) Å short Ir-O distances (Table 4.2). The structure refinement yields very large anisotropic displacement parameters (ADP) for one oxygen atom, O5a, in the AlO₄ tetrahedra (Inset of Figure 4.3). A reduced occupancy of the O5a site is unreasonable because the Al-tetrahedron is a strong unit from which it is highly unlikely that an oxygen can be removed. Furthermore allowing reduced occupancy on this site in the refinement does not remove the large elongation of the ADP ellipsoid. Anharmonic atomic displacement of O5a has been also excluded because no reduction of its atomic displacements can be observed in the structure obtained at 90 K. We therefore conclude that rather than thermal motion, this oxygen is split between two nearby

Chapter 4. Synthesis, Structure, Transport and Magnetic Properties of 5d Transition Metal Compounds—Iridates

Table 4.1: Details of the data collection and structure refinement for $\text{Ba}_8\text{Al}_2\text{IrO}_{14}$. The diffraction study is performed at 293(2) and 90(2) K using Mo $K\alpha$ radiation with $\lambda = 0.71073 \text{ \AA}$. The lattice is monoclinic, $C2/m$ space group, with $Z = 2$. A full-matrix least-squares method was employed to optimize $F2$.

| Empirical formula | $\text{Ba}_8\text{Al}_2\text{IrO}_{14}$ | |
|---|--|----------------------|
| Formula weight (g/mol) | 1568.88 | |
| Temperature (K) | 293(2) | 90(2) |
| Unit cell dimensions (\AA ,deg) | $a = 19.8367(14)$ | $a = 19.8283(15)$ |
| | $b = 5.9709(6)$ | $b = 5.9591(5)$ |
| | $c = 7.6138(7)$ | $c = 7.6013(5)$ |
| | $\beta = 109.785(5)$ | $\beta = 109.656(5)$ |
| Volume (\AA^3) | 848.57(13) | 845.82(11) |
| Calculated density (g/cm^3) | 6.140 | 6.160 |
| Absorption coefficient (mm^{-1}) | 26.212 | 26.297 |
| $F(000)$ | 1326 | |
| θ range for data collection (deg) | 3.58 - 34.98 | 3.59 - 35.00 |
| Index ranges | $-32 \leq h \leq 30, -9 \leq k \leq 9, -12 \leq l \leq 12$ | |
| Reflections collected/unique | 10716/2019 | 12095/2014 |
| | $R_{int} = 0.0564$ | $R_{int} = 0.0537$ |
| Completeness to 2θ | 99.6% | 99.7% |
| Data/restraints/parameters | 2019/0/64 | 2014/0/64 |
| Final R indices [$I > 2\sigma(I)$] | $R_1 = 0.0390$ | $R_1 = 0.0392$ |
| | $wR_2 = 0.0918$ | $wR_2 = 0.0791$ |
| R indices (all data) | $R_1 = 0.0442$ | $R_1 = 0.0455$ |
| | $wR_2 = 0.0949$ | $wR_2 = 0.0821$ |
| Goodness-of-fit | 1.133 | 1.110 |

Table 4.2: Atomic coordinates and equivalent isotropic displacement parameters [$\text{\AA}^2 \times 1000$] for $\text{Ba}_8\text{Al}_2\text{IrO}_{14}$.

| Atom | Site | x | y | z | U_{iso} |
|------|------|-----------|-----------|------------|-----------|
| Ir1 | 2a | 0 | 0 | 0 | 10(1) |
| Ba1 | 4i | 0.0251(1) | 1/2 | 0.7925(1) | 15(1) |
| Ba2 | 4i | 0.3149(1) | 0 | 0.7067(1) | 16(1) |
| Ba3 | 4i | 0.1726(1) | 0 | 0.9887(1) | 23(1) |
| Ba4 | 4i | 0.0973(1) | 0 | 0.4615(1) | 30(1) |
| Al1 | 4i | 0.1735(2) | 1/2 | 0.7034(5) | 31(1) |
| O1 | 4i | 0.4079(7) | 0 | 0.4700(12) | 45(3) |
| O2 | 4i | 0.4664(4) | 1/2 | 0.2254(10) | 17(1) |
| O3 | 8j | 0.0726(3) | 0.2277(8) | 0.1222(7) | 16(1) |
| O4 | 4i | 0.3279(6) | 0 | 0.0701(14) | 53(3) |
| O5a | 8j | 0.3005 | 0.2977 | 0.2873 | 65(4) |
| O5b | 8j | 0.2867 | 0.2124 | 0.3463 | 65(4) |

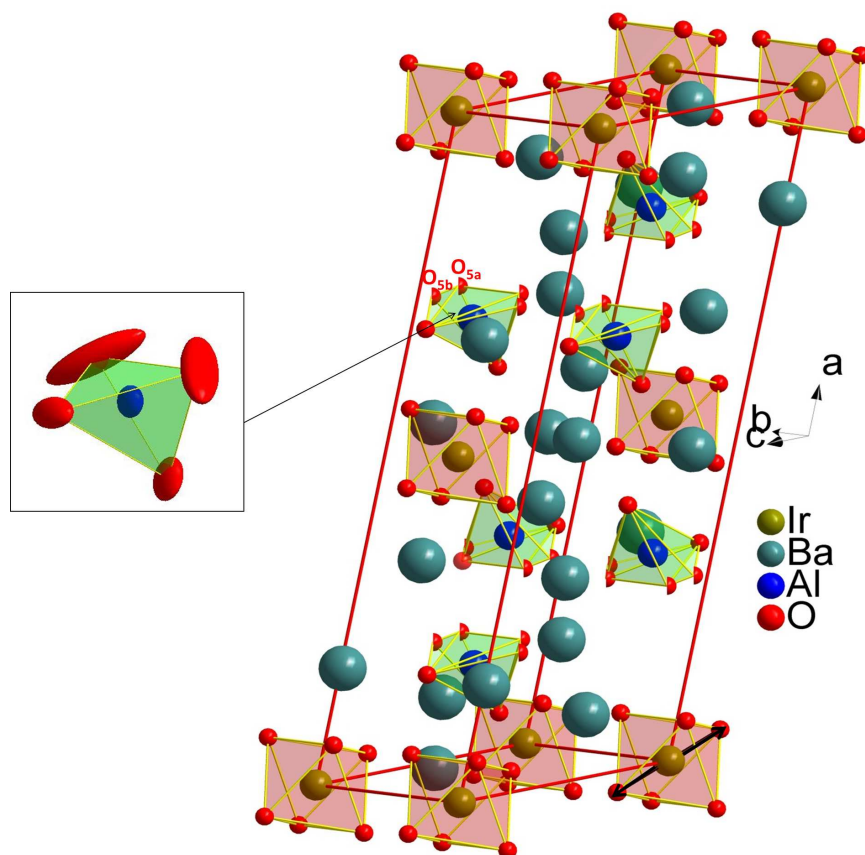


Figure 4.3: Crystal structure of Ba₈Al₂IrO₁₄. Red and green polyhedral indicate IrO₆ octahedra and AlO₄ tetrahedra, respectively. The black arrows mark the long axis direction of the elongated octahedra. The unit cell is outlined in red. The inset shows AlO₄ tetrahedron with the extremely large ADP ellipsoid of non-split oxygen atom with atomic displacement ellipsoids at 50% probability. Split atoms, O5a and O5b, are shown with half spheres indicating their occupation of 50%.

positions, O5a and O5b (Figure 4.3). The splitting of O5a and O5b can also be explained from the consideration of the first coordination spheres of Ba3 and Al1 (Table 4.4). Two positions of O5a are necessary to form Ba3-octahedron with 2.5755(6) Å short distances between Ba3 and O5a, while the O5b positions cannot compensate a charge Ba due to the 3.1308(7) Å long distances between Ba3 and O5b. On the other hand, two O5b positions are necessary to form Al1-tetrahedron with 1.628(3) Å short distances between Al1 and O5b, while the O5a is too far from Al1 (with 1.8740(13) Å long distances between Al1 and O5a). Therefore, statistical occupation of O5a and O5b is a solution of the situation. Refinements allowing a variable occupancy on O2 and O3 in the IrO₆ octahedra yielded 100 % (Table 4.5).

The oxidation state of metal ions in solids may be estimated using an empirical quantity, known as the bond valence sum (BVS), which is based on statistics of crystallographically

Chapter 4. Synthesis, Structure, Transport and Magnetic Properties of 5d Transition Metal Compounds—Iridates

Table 4.3: ADP atomic parameters in Ba₈Al₂IrO₁₄.

| Atom | U_{11} | U_{22} | U_{33} | U_{23} | U_{13} | U_{12} |
|------|----------|----------|----------|----------|----------|----------|
| Ir1 | 8(1) | 9(1) | 12(1) | 0 | 2(1) | 0 |
| Ba1 | 17(1) | 14(1) | 15(1) | 0 | 5(1) | 0 |
| Ba2 | 11(1) | 18(1) | 18(1) | 0 | 4(1) | 0 |
| Ba3 | 13(1) | 29(1) | 26(1) | 0 | 8(1) | 0 |
| Ba4 | 30(1) | 29(1) | 20(1) | 0 | -7(1) | 0 |
| Al1 | 36(2) | 40(2) | 16(1) | 0 | 10(1) | 0 |
| O1 | 66(8) | 45(6) | 15(3) | 0 | 3(4) | 0 |
| O2 | 15(3) | 19(3) | 19(3) | 0 | 8(2) | 0 |
| O3 | 13(2) | 12(2) | 21(2) | -1(2) | 2(2) | -3(2) |
| O4 | 25(5) | 103(11) | 23(4) | 0 | -2(4) | 0 |

Table 4.4: Selected interatomic distances (Å) for Ba₈Al₂IrO₁₄.

| Atom1 | atom2 | Count | <i>d</i> 1,2 (Å) | Atom1 | atom2 | Count | <i>d</i> 1,2 (Å) | |
|-------|-------|-------|------------------|-------|-------|-----------|------------------|-----------|
| Ir1 | O3 | 4× | 1.970(5) | Ba3 | O4 | 1× | 2.924(12) | |
| | O2 | 2× | 2.041(7) | | O4 | 2× | 3.0196(18) | |
| Ba1 | O1 | 1× | 2.739(13) | Ba4 | O5b | 2× | 3.1308(7) | |
| | O4 | 1× | 2.750(11) | | O5a | 2× | 2.5755(7) | |
| Ba2 | O1 | 1× | 2.750(11) | O2 | 1× | 2.610(8) | | |
| | O3 | 2× | 2.767(5) | O3 | 2× | 2.813(5) | | |
| | O3 | 2× | 2.868(5) | O5b | 2× | 2.8676(6) | | |
| | O2 | 2× | 2.9960(7) | O1 | 2× | 3.040(2) | | |
| | O5b | 2× | 2.5396(5) | O2 | 1× | 3.052(7) | | |
| | O5a | 2× | 2.6044(5) | Al1 | O5b | 2× | 1.628(3) | |
| | O4 | 1× | 2.698(12) | | O4 | 1× | 1.724(12) | |
| | O3 | 2× | 2.712(5) | O1 | 1× | 1.707(13) | | |
| Ba3 | O5b | 2× | 2.9292(6) | O5a | O5a | 2× | 1.8740(13) | |
| | O1 | 1× | 2.995(13) | | O5b | 1× | 0.8292(1) | |
| | O5a | 2× | 2.5755(6) | | Ir1 | Ba4 | 2× | 3.3884(8) |
| | O2 | 1× | 2.686(8) | | | Ba3 | 2× | 3.4534(7) |
| | O3 | 2× | 2.863(5) | | | Ba1 | 2× | 3.4913(4) |

Table 4.5: Atomic occupancy for Ba₈Al₂IrO₁₄.

| Ir1 | Ba1 | Ba2 | Ba3 | Ba4 | Al1 |
|---------|----------|-----------|----------|----------|-----------|
| 1 | 1.006(2) | 1.007(2) | 1.011(2) | 1.001(3) | 0.974(11) |
| O1 | O2 | O3 | O4 | O5a | O5b |
| 0.99(2) | 1.03(2) | 1.031(14) | 1.02(3) | 0.46(2) | 0.51(2) |

determined metal-ligand bond distance. V_i , the effective valence or bond valence sum of the i th atom, is determined by

$$V_i = \sum_j S_{ij} = \sum_j \exp[(r_0 - r_{ij})/0.37], \quad (4.1)$$

where r_0 is empirically determined for each $i-j$ atomic pair and r_{ij} is the observed interatomic distance between the i th and j th atom in the material under consideration. S_{ij} can be considered to be the effective charge in the r_{ij} bond. V_i is then obtained as the sum over j of all of the S_{ij} . Ref. [76] reported two all-Ir⁶⁺ containing oxides, Nd₂K₂O₇ (Ir-O distance 1.982Å) and Sm₂K₂O₇ (Ir-O distance 1.972Å), prepared under ambient pressure. Using these two compounds the average r_0 for Ir⁶⁺ is 1.977Å. For Ba₈Al₂IrO₁₄, the four 1.970Å bonds and the two 2.041Å bonds (Table 4.4) give a BVS of 5.76(9) for Ir, suggesting that Ir(VI) is the most likely oxidation state – in agreement with the stoichiometry obtained from crystallography.

4.1.3 Transport Properties

The electrical resistivity ρ of Ba₈Al₂IrO₁₄ measured in the 180-600 K temperature range is shown in Figure 4.4(a). The resistivity value is 7.3 kΩcm at room temperature, and ρ increases monotonically with temperature decreasing ($d\rho/dT < 0$), revealing the insulating nature of this compound. In the inset of Figure 4.4(a), we show $d\ln\rho/d(e/k_B T)$ vs. T . Thermally activated behavior is observed above 350 K. In this temperature range $\rho(T)$ is fitted by:

$$\rho(T) = \rho_0 \exp(E_a/k_B T), \quad (4.2)$$

where ρ_0 is a parameter depending on the sample characteristics, k_B is Boltzmann's constant, T is absolute temperature and E_a is the thermal activation energy of electrical conduction. It yielded the activation energy $E_a = 0.290 \text{ eV} \pm 0.005 \text{ eV}$. In this case, a rough estimate of band gap energy $E_g = 2E_a$ is $0.58 \text{ eV} \pm 0.01 \text{ eV}$ above 350 K. At lower temperature, the resistivity deviates from activated behavior.

As shown in Figure 4.4(b), the Seebeck coefficient S of Ba₈Al₂IrO₁₄ is positive in the whole temperature range, suggesting hole dominated conduction. At room temperature, $S = 7500 \mu\text{V/K}$. S further decreases with temperature increasing as expected for insulators, and changes gradually with no clear transition temperature in the temperature range 300-500 K and 620-680 K.

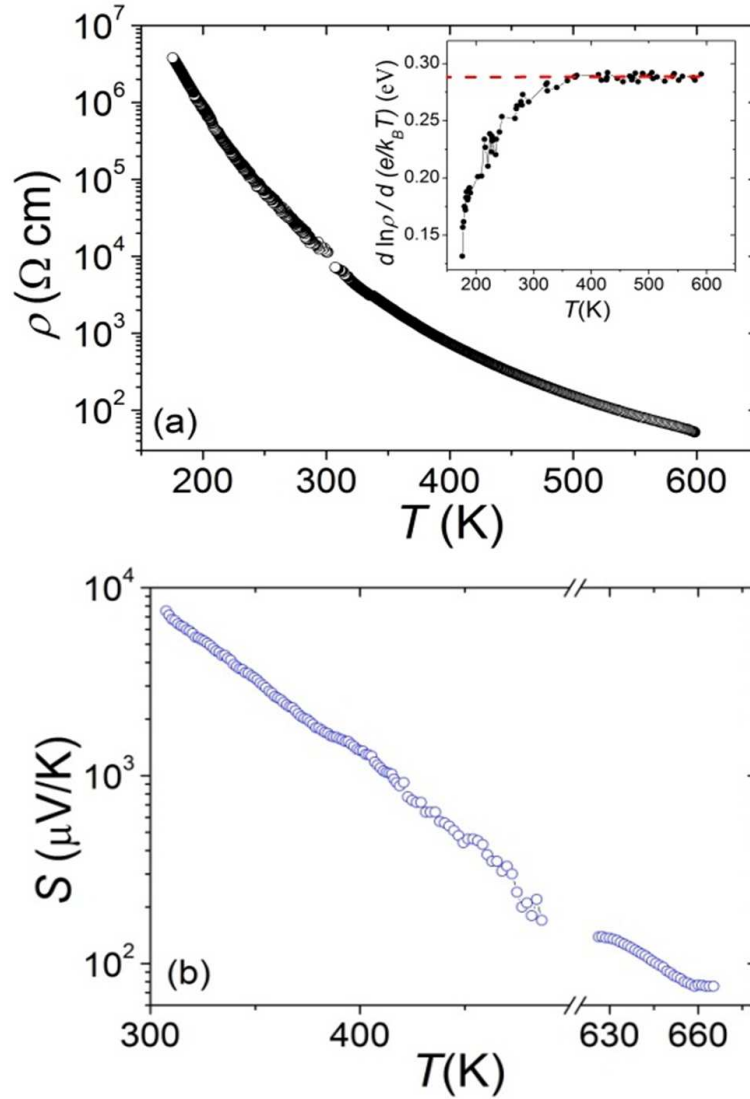


Figure 4.4: (a) Electrical resistivity of $\text{Ba}_8\text{Al}_2\text{IrO}_{14}$. The inset shows $d \ln \rho / d(e/k_B T)$ vs. T . The red dashed line is the guide to eyes of this fitting. $E_a \sim 0.29$ eV is estimated above 350 K in this plot. (b) The Seebeck coefficient of $\text{Ba}_8\text{Al}_2\text{IrO}_{14}$.

To confirm that $\text{Ba}_8\text{Al}_2\text{IrO}_{14}$ is a p-type band insulator with a narrow band gap of 0.58 eV, A. Akrap and J. Teyssier performed the optical measurements at room temperature [69]. Transmission and reflectivity were measured in the range from 0.15 to 0.5 eV, and complemented by spectroscopic ellipsometry from 0.5 to 2.6 eV. The optical transmission and reflectivity are shown in Figure 4.5(a) from 0.15 to 0.5 eV at room temperature. The low reflectivity and the high transmission indicate the insulating behavior in this material. These two quantities are

related to the dielectric function,

$$\epsilon = \epsilon_1 + \epsilon_2. \quad (4.3)$$

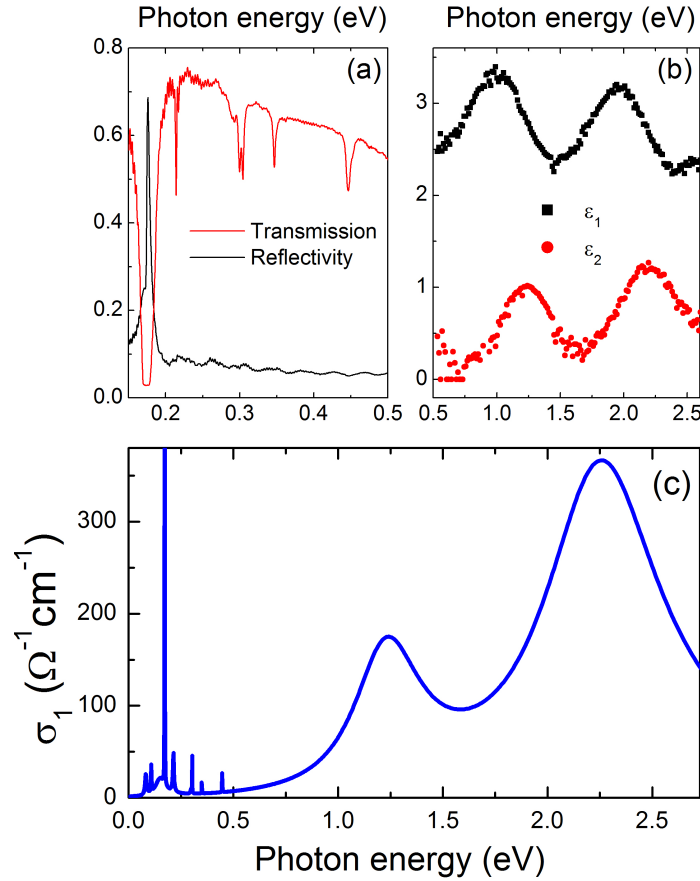


Figure 4.5: (a) Transmission and reflectivity spectra as a function of photon energy for Ba₈Al₂IrO₁₄ at room temperature. (b) The real and imaginary part of the dielectric function. (c) The real part of optical conductivity, $\sigma_1(w)$, modeled from the transmission, reflectivity and ellipsometry data, shown at 300 K.

Figure 4.5(b) shows the real and imaginary part of the dielectric function, ϵ_1 and ϵ_2 , as determined by the ellipsometry from 0.5 to 2.6 eV. By simultaneously fitting the above optical quantities, one obtains an estimate of the complex dielectric function ϵ , and from it the real part of the optical conductivity, $\sigma_1(w)$, is shown in Figure 4.5(c). The conductivity $\sigma_1(w)$ is gapped below ~ 0.7 eV, indicating the insulating behavior of this material, which are in accordance with the results of resistivity. Below the gap, several sharp oscillations are seen,

which can be attributed to vibrational phonon modes. Two strong absorptions can be seen above the gap, centered at 1.2 and 2.2 eV, which are likely intraband transitions.

4.1.4 Magnetic Properties

The temperature dependence of magnetic susceptibility parallel to the b -axis of $\text{Ba}_8\text{Al}_2\text{IrO}_{14}$, measured in applied magnetic fields of 0.1 T, 1 T and 5 T, is shown in Figure 4.6(a). The susceptibility increases monotonically with decreasing temperature and displays no order down to 2 K. The zero-field cooling (ZFC) and field cooling (FC) data completely overlay at all temperatures down to 2 K. The susceptibility respectively parallel and perpendicular to the b -axis are compared in Figure 4.6(b), showing the magnetic anisotropy of $\text{Ba}_8\text{Al}_2\text{IrO}_{14}$.

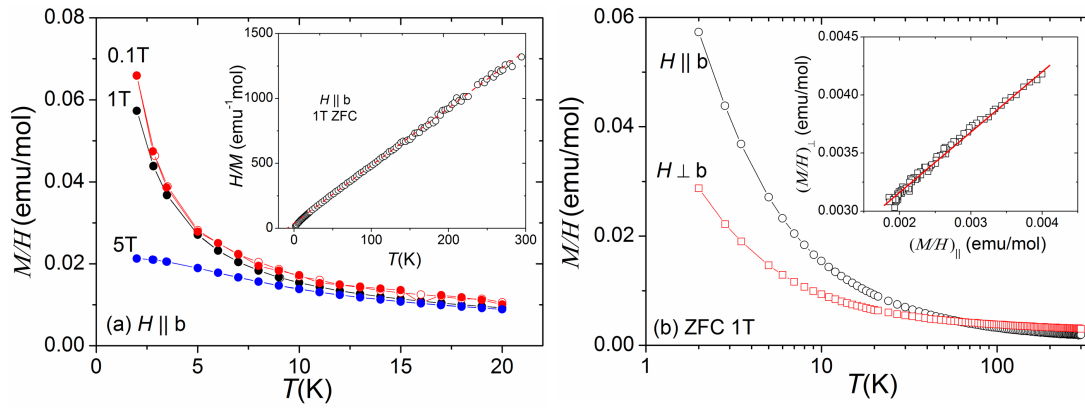


Figure 4.6: (a) Temperature dependence of M/H which approximates the magnetic susceptibility except below 10 K where $M(T)$ start to deviate from linear of $\text{Ba}_8\text{Al}_2\text{IrO}_{14}$ under various fields applied parallel to the b -axis. Both ZFC and FC data are shown. The inset shows inverse magnetic susceptibility $1/(M/H - \chi_0)$ versus temperature T in a magnetic field $H = 1$ T (ZFC). (b) Temperature dependent magnetic susceptibility of $\text{Ba}_8\text{Al}_2\text{IrO}_{14}$ under $H = 1$ T applied perpendicular and parallel to the b -axis, respectively, in ZFC. The inset shows $(M/H)_\perp(T)$ versus $(M/H)_\parallel(T)$.

On the other hand, we plotted $(M/H)_\perp(T)$ versus $(M/H)_\parallel(T)$ in the inset of Figure 4.6(b) to quantitatively analyze the anisotropic susceptibility. The analysis described in Ref. [78] causes the relation between $\chi_\parallel(T)$ and $\chi_\perp(T)$:

$$\chi_\perp(T) = (g_\perp/g_\parallel)^2 \chi_\parallel(T) + [\chi_0^\perp - (g_\perp/g_\parallel)^2 \chi_0^\parallel], \quad (4.4)$$

where the ratio $(g_\perp/g_\parallel)^2$ can be obtained from the fitted slope. $\text{Ba}_8\text{Al}_2\text{IrO}_{14}$ has the anisotropy of $(g_\perp/g_\parallel)^2 = 0.50(5)$.

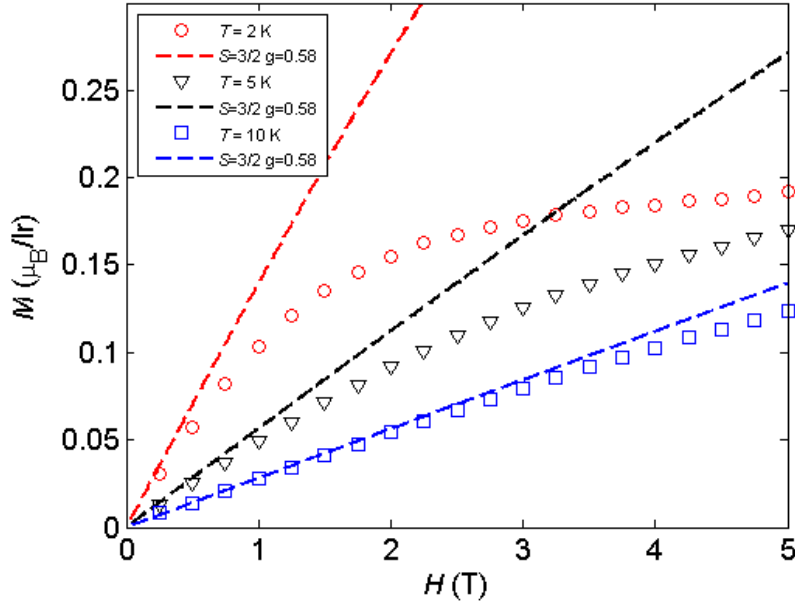


Figure 4.7: Isothermal magnetization M versus magnetic field H applied parallel to the b -axis at various temperatures T . The dashed lines are fits to the Brillouin functions for $S = 3/2$, $g = 0.58$.

Further fitting the data above 50 K to a modified Curie-Weiss (CW) law

$$\chi(T) = C/(T - \theta_{\text{CW}}) + \chi_0, \quad (4.5)$$

yielded a Curie-Weiss constant $C = 0.23(1)$ emu/mol K, an effective moment $\mu_{\text{eff}} = 1.36(3)\mu_B$ per formula unit, a Curie temperature $\theta = -10(1)$ K and a temperature independent term $\chi_0 = 1.15 \times 10^{-3}$ emu/mol for $H \parallel b$ (parallel to the needle direction) and $C = 0.16(1)$ emu/mol K, $\mu_{\text{eff}} = 1.13(4)\mu_B$ per formula unit, $\theta = -32(2)$ K and $\chi_0 = 2.59 \times 10^{-3}$ emu/mol for $H \perp b$ (perpendicular to the needle direction).

The negative Curie temperature θ indicates antiferromagnetic (AFM) coupling. The anisotropy obtained from Curie-Weiss fitting is $\mu_{\text{eff}\perp}/\mu_{\text{eff}\parallel} = 0.69(8)$, which is in same direction but numerically different from the $(g_{\perp}/g_{\parallel})^2 = 0.50(5)$ in the plot of $(M/H)_{\perp}(T)$ versus $(M/H)_{\parallel}(T)$. This is because the latter assumes same functional form for $(M/H)_{\perp}(T)$ and $(M/H)_{\parallel}(T)$, which is not the case if θ is anisotropic. The anisotropic Curie-Weiss constant C indicates the magnetic anisotropy of this compound, which can be understood from an anisotropic g -factor, as we discussed before. The temperature independent term χ_0 is rather large and anisotropic, but similar large and anisotropic value has been reported for other compounds, such as NaIrO₃, Pr₂Ir₂O₇ and Na_xCoO₂·yH₂O [78, 79, 80].

Chapter 4. Synthesis, Structure, Transport and Magnetic Properties of 5d Transition Metal Compounds—Iridates

The Ir^{6+} ions sit in an octahedral crystal field generated by the neighboring O^{2-} ions splitting the $5d$ orbitals into higher e_g and lower t_{2g} levels. The electronic configuration of the Ir^{6+} being $5d^3$ the t_{2g} crystal field levels are half occupied and the Hund coupling selects the high-spin $S = 3/2$ state. However the effective moment for a spin-3/2 isotropic paramagnet is $\mu_{eff} = 3.87\mu_B$ far larger than the observed $\mu_{eff} = 1.36\mu_B$. The strong spin-orbit coupling present in the Ir $5d$ orbitals ($\lambda_{SO} \sim 400$ meV) has been shown to lead to such a reduction of the $5d^3$ effective magnetic moment while the tetragonal distortion of the octahedron will further reduce it [3, 81, 82]. Comparing the measured effective moment with the one for an isotropic $S = 3/2$ paramagnet, we have for $H \parallel b$

$$\mu_{eff} = g\sqrt{S(S+1)}\mu_B, \quad (4.6)$$

yielding a reduced g -factor $g_{\parallel} = 0.58$.

The magnetic field dependence H applied parallel to the b -axis of the magnetization of $\text{Ba}_8\text{Al}_2\text{IrO}_{14}$, measured at different temperatures, is shown in Figure 4.7. The dashed lines are Brillouin functions for $S = 3/2$, $g = 0.58$. The $M(H)$ data above $T = 10$ K follow the Brillouin function, showing the absence of ferromagnetic impurities. At lower T $M(H)$ become gradually smaller than the Brillouin function, indicating dominant antiferromagnetic coupling.

4.1.5 Conclusion

We synthesized a new compound $\text{Ba}_8\text{Al}_2\text{IrO}_{14}$ and systematically studied its crystal structure, transport, optical and magnetic properties. It has been synthesized as single crystal which provides a rare example of a full-Ir(VI) compound that can be grown under ambient pressure conditions. Our experiment shows $\text{Ba}_8\text{Al}_2\text{IrO}_{14}$ has monoclinic crystal structure with the space group of $C2/m(12)$. It is a p -type band insulator with a narrow band gap of approximately 0.6 eV, and these are confirmed by the optical measurements. Furthermore, $\text{Ba}_8\text{Al}_2\text{IrO}_{14}$ shows antiferromagnetic couplings but display no order down to 2 K. We hope this work will stimulate more investigations on Ir-based compounds that offer a wide window into the research of spin-orbit interactions and the strength of electronic correlations.

4.2 Possible unusual spin state of Ir^{4+} in $\text{Ba}_{21}\text{Ir}_9\text{O}_{43}$ single crystal

4.2.1 Motivation for This Work

There is considerable interest in studying correlated $5d$ -electron transition metal oxides with strong spin-orbit coupling (SOC) [83, 39, 84]. Recent focus has been on new iridate compounds where experimental discoveries have strongly challenged theoretical predictions. For example,

4.2. Possible unusual spin state of Ir⁴⁺ in Ba₂₁Ir₉O₄₃ single crystal

in pentavalent (Ir⁵⁺) 5d⁴ iridates a strong SOC is predicted to realize a nonmagnetic $J = 0$ state [49], but substantial magnetic moments have been found in Ba₂YIrO₆ [50] and especially in Sr₂YIrO₆ [51], where structural distortion of the octahedral environment leads to 0.91 μ_B /Ir. Furthermore, a possible realization of a spin-orbital liquid with Ir⁵⁺ has been discussed for 6H hexagonal Ba₃ZnIr₂O₉ powder [10].

In tetravalent (Ir⁴⁺) 5d⁵ iridates, such as Sr₂IrO₄ [44, 3, 45], a complex spin-orbit entangled $J_{\text{eff}} = 1/2$ state is realized, with a reduced bandwidth due to the splitting from the $J_{\text{eff}} = 3/2$ states, which leads to the localization of electrons even by a relatively small Coulomb interaction compared to their 3d counterparts. Additional effects of SOC include XY anisotropy [85, 86], locking of the magnetic moment to the correlated rotation of oxygen octahedra in Sr₂IrO₄ [87], anisotropic dimer excitations in Sr₃Ir₂O₇ [46], and Kitaev type of magnetic interactions in Na₂IrO₃ [88]. Structural distortions from the ideal octahedral environment have been observed in the pyrochlore family of the type $R_2\text{Ir}_2\text{O}_7$ (R =rare-earth) where trigonal compression induces a reconstruction of energy levels [89, 90].

So far, to the best of our knowledge, there have been very few reports [91] of oxides containing Ir⁴⁺ or Ir⁵⁺ ions in an environment different from octahedral. Following the observations of profound influence of structural effects onto the energy scheme of iridium ions and consequently the resulting spin-orbital state, it can be expected that non-octahedral ligand coordination could result in different properties.

Here we report the synthesis, crystal structure, transport, and magnetic properties of single crystals of a novel layered iridate Ba₂₁Ir₉O₄₃. It consists of layers of a triangular lattice of Ir₂O₉ dimers, much alike in Ba₃ZnIr₂O₉, that are intercalated by another layer of a triangular lattice containing three different iridium environments: two regular octahedra and a triangular pyramid (see Fig. 4.8(a-c) for the structure). We conclude that the triangular pyramid represents a novel environment for an Ir⁴⁺ ion with a high-spin state $J_{\text{eff}} = 5/2$.

4.2.2 Synthesis and Crystal Structure

Single crystals of Ba₂₁Ir₉O₄₃ were grown in two steps. Firstly, a mixture of powders with the molar ratio of BaCO₃ : IrO₂ = 13 : 2 was heated for 2 days at 1000 °C and cooled down slowly (2 °C/h) to 700 °C in Al₂O₃ crucible. After the reaction, black powder was obtained and pressed into a pellet. Secondly, the mixture of the weight ratio of the pellet : K₂CO₃ powder flux = 1 : 20 was heated for 2 days at 1150 °C and cooled down to 800 °C at 2 °C/h in Al₂O₃ crucible. Black-colored single crystals of Ba₂₁Ir₉O₄₃ were obtained with plate-like shape after the reaction, as shown in Fig. 4.8(d), where the maximum dimensions were 2 × 2 × 0.1 mm³. The direction perpendicular to the plate coincides with the crystallographic c axis of the hexagonal system. The chemical composition was determined using an Energy Dispersive X-Ray detector (EDX,

Chapter 4. Synthesis, Structure, Transport and Magnetic Properties of 5d Transition Metal Compounds—Iridates

Oxford Instruments EDX X-MAX), which yielded the molar ratios Ba : Ir of 69.5(4) : 30.6(7).

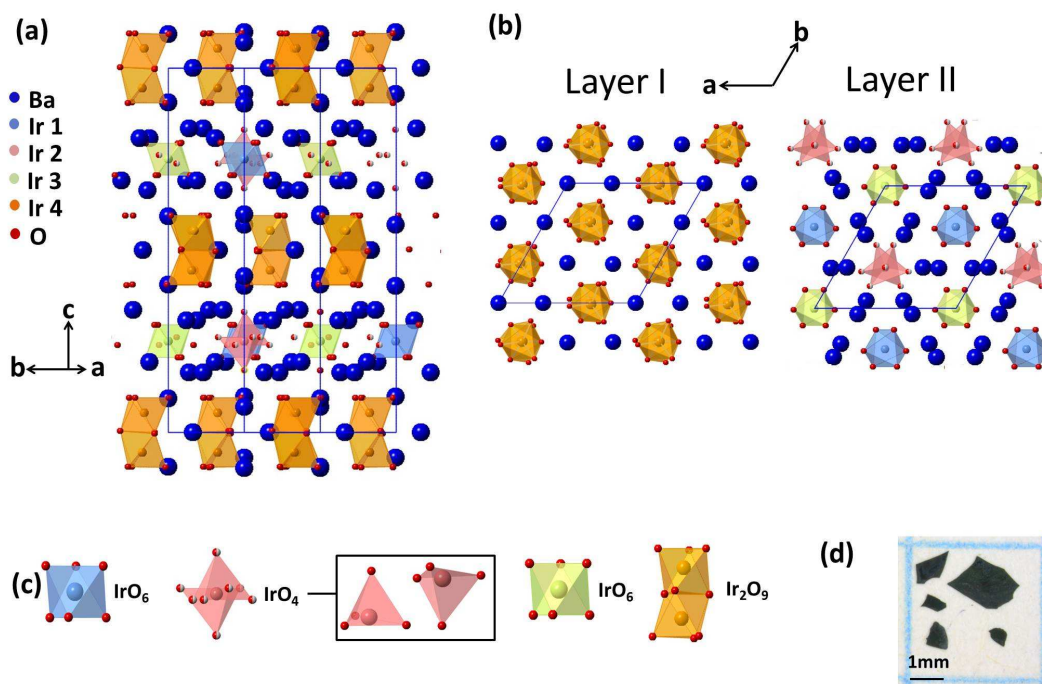


Figure 4.8: (a) Crystal structure of $\text{Ba}_{21}\text{Ir}_9\text{O}_{43}$ where a unit cell is drawn by solid line. (b) Two different layers of triangular lattice Ir-O polyhedra, labeled as Layer I $[\text{Ba}_9\text{Ir}_6\text{O}_{27}]^{-6}$ (left) and Layer II $[\text{Ba}_{12}\text{Ir}_3\text{O}_{16}]^{+6}$ (right). (c) The Ir-O polyhedra: blue and green IrO_6 octahedra are geometrically identical within one standard deviation; face-sharing orange octahedra form a Ir_2O_9 dimer; red polyhedron is shown as a statistical superposition of two possible IrO_4 triangular pyramid, having the same geometry but opposite in orientation along c direction, with 50 % occupancy on every oxygen sites. (d) Representative single crystals of $\text{Ba}_{21}\text{Ir}_9\text{O}_{43}$.

A. Arakcheeva and S. Katrych had determined the crystal structure of the novel iridate $\text{Ba}_{21}\text{Ir}_9\text{O}_{43}$ [70].

Figure 4.8(a) shows the crystal structure which belongs to the hexagonal system. The details of the data collection and structure refinement are listed in Tables 4.6-4.9. The structure consists of two different layered blocks. For the layer I, the central structural feature is the formation of Ir_2O_9 dimers composed of two face-sharing IrO_6 octahedra (Ir4), as shown in Fig. 4.8(b) and (c). Such dimers are typical for 6H-perovskite-type oxides [47, 94]. Layer II consists of isolated IrO_6 octahedra (Ir1 and Ir3) and IrO_4 triangular pyramid (Ir2). The IrO_4 pyramids appear in two possible orientations, that is, an apical oxygen pointing either upward or downward, in statistically equal distribution. The chemical formula of $\text{Ba}_{21}\text{Ir}_9\text{O}_{43}$ was obtained from the fully occupied positions for all sites of all Ir atoms with the accuracy 1.00(1). The molar ratio of Ba/Ir from the formula $21/9=2.33$ is close to the value $69.5(4)/30.6(7) = 2.27(7)$ from the EDX analysis.

4.2. Possible unusual spin state of Ir⁴⁺ in Ba₂₁Ir₉O₄₃ single crystal

Table 4.6: Details of the data collection and structure refinement for Ba₂₁Ir₉O₄₃ obtained at room temperature using Mo *K* α radiation with $\lambda = 0.71073$ Å.

| Empirical formula | Ba ₂₁ Ir ₉ O ₄₃ |
|---|--|
| Formula weight (g/mol) | 5302.07 |
| space group | P6 ₃ 22 |
| Unit cell parameters (Å) | $a = b = 10.5102(9)$ $c = 25.1559(19)$ |
| Volume (Å ³) | 2406.5 |
| number of twins | 2 |
| Twin coefficients | 0.77(6), 0.23(6) |
| Calculated density (g/cm ³) | 7.317 |
| Reflections collected/unique | 6486/1188 |
| Data/restraints/parameters | 1188/0/81 |
| Final <i>R</i> indices [$I > 3\sigma(I)$] | $R = 0.0629$, $wR = 0.0586$ |
| Goodness-of-fit | 1.46 |

Table 4.7: Atomic coordinates and equivalent isotropic displacement parameters for Ba₂₁Ir₉O₄₃.

| Atom | Site | Occupancy | <i>x</i> | <i>y</i> | <i>z</i> | <i>U</i> _{iso} |
|------|------|-----------|-------------|-------------|-------------|-------------------------|
| Ir1 | 2c | 1 | 0.3333 | 0.6667 | 0.25 | 0.0075(7) |
| Ir2 | 2d | 1 | 0.6667 | 0.3333 | 0.25 | 0.0105(7) |
| Ir3 | 2b | 1 | 0 | 0 | 0.25 | 0.0088(7) |
| Ir4 | 12i | 1 | 0.32168(12) | 0.33190(13) | 0.05428(4) | 0.0136(5) |
| Ba1 | 6g | 1 | 0.3266(3) | 0 | 0 | 0.0171(9) |
| Ba2 | 4f | 1 | 0.3333 | 0.6667 | 0.09830(14) | 0.0257(10) |
| Ba3 | 12i | 1 | 0.6644(2) | 0.0629(2) | 0.33549(8) | 0.0193(8) |
| Ba4 | 4e | 1 | 0 | 0 | 0.09392(16) | 0.0259(10) |
| Ba5 | 12i | 1 | 0.0445(2) | 0.3305(3) | 0.30746(8) | 0.0280(9) |
| Ba6 | 4f | 1 | 0.6667 | 0.3333 | 0.07024(15) | 0.0331(11) |
| O1 | 6g | 1 | 0.180(3) | 0.180(3) | 0 | 0.024(8) |
| O2 | 12i | 1 | 0.348(2) | 0.825(2) | 0.2052(8) | 0.025(5) |
| O3 | 12i | 1 | 0.325(2) | 0.476(2) | -0.0029(8) | 0.028(5) |
| O4 | 12i | 1 | 0.351(3) | 0.192(2) | 0.0956(8) | 0.030(6) |
| O5 | 12i | 1 | 0.4676(19) | 0.498(2) | 0.0948(7) | 0.012(4) |
| O6 | 12i | 1 | 0.151(2) | 0.312(2) | 0.0946(7) | 0.016(4) |
| O7 | 4f | 0.5 | 0.6667 | 0.3333 | 0.330(3) | 0.022(16) |
| O8 | 12i | 1 | 0.142(3) | -0.010(3) | 0.2058(11) | 0.043(7) |
| O9 | 12i | 0.5 | 0.817(5) | 0.518(6) | 0.239(3) | 0.063(19) |

Chapter 4. Synthesis, Structure, Transport and Magnetic Properties of 5d Transition Metal Compounds—Iridates

Table 4.8: ADP atomic parameters in $\text{Ba}_{21}\text{Ir}_9\text{O}_{43}$.

| Atom | U_{11} | U_{22} | U_{33} | U_{23} | U_{13} | U_{12} |
|------|------------|------------|------------|------------|------------|------------|
| Ir1 | 0.0080(8) | 0.0080(8) | 0.0066(13) | 0.0040(4) | 0 | 0 |
| Ir2 | 0.0109(8) | 0.0109(8) | 0.0097(13) | 0.0054(4) | 0 | 0 |
| Ir3 | 0.0078(8) | 0.0078(8) | 0.0106(14) | 0.0039(4) | 0 | 0 |
| Ir4 | 0.0146(6) | 0.0166(6) | 0.0113(5) | 0.0091(6) | -0.0032(5) | -0.0016(5) |
| Ba1 | 0.0177(9) | 0.0118(13) | 0.0198(12) | 0.0059(7) | 0.0004(5) | 0.0007(10) |
| Ba2 | 0.0211(11) | 0.0211(11) | 0.035(2) | 0.0106(5) | 0 | 0 |
| Ba3 | 0.0145(8) | 0.0217(10) | 0.0180(9) | 0.0065(9) | 0.0014(11) | 0.0016(9) |
| Ba4 | 0.0185(11) | 0.0185(11) | 0.041(2) | 0.0092(5) | 0 | 0 |
| Ba5 | 0.0362(13) | 0.0163(9) | 0.0227(11) | 0.0065(10) | 0.0041(9) | 0.0000(11) |
| Ba6 | 0.0313(13) | 0.0313(13) | 0.037(2) | 0.0157(6) | 0 | 0 |

Table 4.9: Selected interatomic distances (Å) for $\text{Ba}_{21}\text{Ir}_9\text{O}_{43}$.

| | |
|---|---|
| Ir1 – octahedron: Ir1 – O2 $6 \times 1.95(3)$ | Ir3 – octahedron: Ir3 – O8 $6 \times 1.90(3)$ |
| Ir2 – triangular pyramid: Ir2 – O7 $1 \times 2.02(6)$ Ir2 – O9 $3 \times 1.81(6)$ | Ir4 – octahedron: Ir4 – O1 $1 \times 2.06(2)$ Ir4 – O3 $1 \times 2.08(3)$ Ir4 – O3 $1 \times 2.10(3)$ Ir4 – O4 $1 \times 1.94(3)$ Ir4 – O5 $1 \times 1.94(2)$ Ir4 – O6 $1 \times 1.98(2)$ Ir4 – O $2.02(3)$ (average distance) |
| Ir4 - couple octahedron shared a common face: Ir4 – Ir4 $2.7371(14)$ | |

4.2.3 Transport Properties

The in-plane electrical resistivity ρ was measured on a plate of single crystal in the 30 – 300 K temperature range using a standard four-probe configuration with DC current and the out-of-plane ρ was measured in the 150 – 300 K temperature range using a point-circle configuration method. Seebeck coefficient S was obtained in the 5–300 K temperature range. ρ as a function

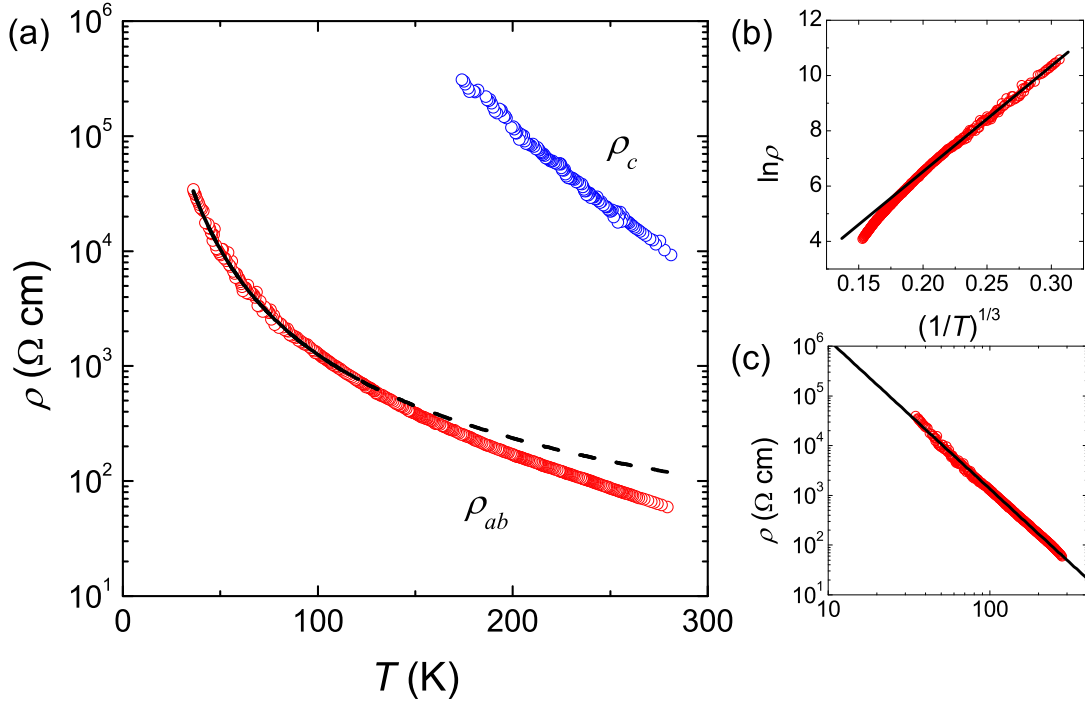


Figure 4.9: (a) In-plane (ρ_{ab}) and out-of-plane (ρ_c) resistivity as a function of temperature where solid and dotted lines represent the two-dimensional VRH model and $\rho \propto T^{-3}$ behavior. (b) $\ln \rho_{ab}$ versus $T^{1/3}$ where solid line is a fit to the VRH model. (c) Log-log plot of $\rho_{ab}(T)$ where dotted line represents T^{-3} dependence.

of temperature along the in-plane (ρ_{ab}) and the out-of-plane (ρ_c) directions are shown in Figure 4.9(a). At room temperature the magnitudes are $\rho_{ab} = 60 \text{ } \Omega\text{cm}$ and $\rho_c = 10^4 \text{ } \Omega\text{cm}$, respectively. Both ρ_{ab} and ρ_c increase monotonically as temperature decreases, revealing the insulating nature of this compound. ρ_c was measured only above 150 K due to high resistance. If we do the detailed analysis, the first thing what we should notice, that ρ_{ab} and ρ_c differ by 2 orders of magnitude, so the electronic system is 2 dimensional (2D).

For ρ_c the temperature range is narrow to perform a reliable fitting. The ρ_{ab} could not be fitted by a thermally activated exponential behavior. On the other hand, we note that the resistivity in a number of iridates such as $\text{Sr}_3\text{Ir}_2\text{O}_7$ [35], NaIrO_3 [79, 95], Ba_2IrO_4 [96], and Sr_2IrO_4 [97] has been found to fit to a variable range hopping (VRH) model. Indeed, the low-temperature

Chapter 4. Synthesis, Structure, Transport and Magnetic Properties of 5d Transition Metal Compounds—Iridates

resistivity below 120 K can be fitted to

$$\rho(T) = \rho_0 \exp(-T_0/T)^{1/3}, \quad (4.7)$$

which is known as the two-dimensional VRH model, and the result is shown by solid lines in Figure 4.9(a) and (b). 2D VRH model works in a limited range of temperature, therefore a refinement is need.

We also discover that ρ_{ab} follows remarkably well to a power law as

$$\rho_{ab} \propto T^{-3}, \quad (4.8)$$

as shown by dotted lines in a log-log plot of Figure 4.9(c), and also in Figure 4.9(a). While this could be a coincidence, it could also suggest that ρ is controlled by unconventional scaling. However, the mathematical fit does not bring much insight due to the absence of a physical picture.

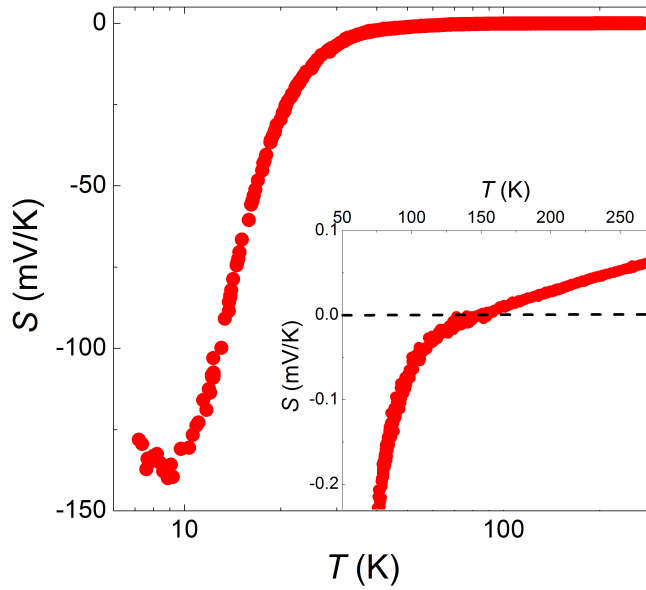


Figure 4.10: Seebeck coefficient S as a function of temperature. The inset shows p -type to n -type crossover with decreasing temperature around 150 K.

The Seebeck coefficient S measured parallel to the ab direction at room temperature is positive, as shown in Figure 4.10, suggesting p -type conduction. The large $S = 70 \mu\text{V/K}$ value at room temperature is consistent with $\text{Ba}_{21}\text{Ir}_9\text{O}_{43}$ being an insulator. With decreasing temperature S decreases linearly down to 150 K, below which it changes sign to n -type conductivity. $\text{Ba}_{21}\text{Ir}_9\text{O}_{43}$ exhibits a colossal S value of -0.14 V/K at 9 K where S shows a broad dip. The S for a nondegenerate semiconductor in a two-band model, consisting of electron e and hole h

4.2. Possible unusual spin state of Ir⁴⁺ in Ba₂₁Ir₉O₄₃ single crystal

bands, can be given by:

$$S(T) = -\frac{k_B}{e} \left(\frac{\mu_e - \mu_h}{\mu_e + \mu_h} \right) \left(\frac{E_g}{k_B T} + \text{const.} \right), \quad (4.9)$$

in which e is the electron charge, μ_e and μ_h are the mobility of electron and hole, respectively, and E_g is the activation energy. Considerable changes in the sign and behavior of S can be caused by a small change of the balance between the temperature-dependent mobility of the two carriers.

We can now turn our attention to the analysis of the T dependence of ρ_{ab} . If we plot it in 2D or 3D VRH model, one can observe that both show deviation at high T , as shown in Figure 4.11. In VRH the electron can choose to hop close in space to higher difference in energy or to hop long distance but paying less in energy. The necessary energy is supplied by the phonon bath. In this model the conductivity is given by the hopping rate, and the formula, known as Mott's VRH in 1,2 or 3D takes this form,

$$1/\rho = \sigma \propto \exp[-(T_0/T)^{1/(D+1)}], \quad (4.10)$$

where the D parameter expresses the dimensionality of the system, $D=3, 2, 1$. However

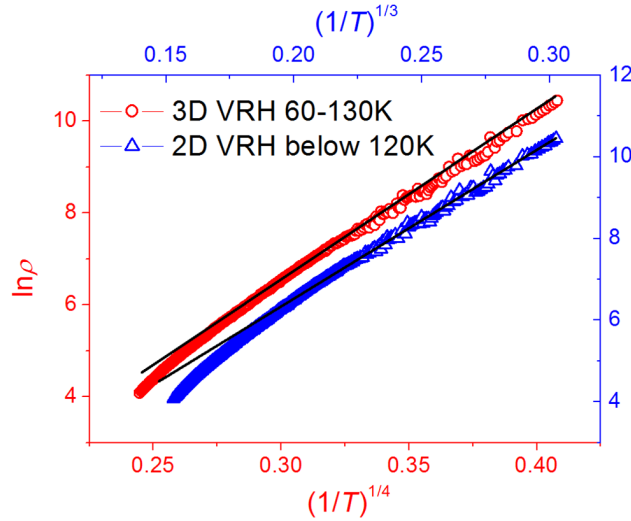


Figure 4.11: $\ln \rho_{ab}$ versus $T^{1/3}$ (blue curve) and $T^{1/4}$ (red curve) where black solid lines are the fits to the 2D and 3D VRH model, respectively.

the above equation is determined in single phonon assisted case therefore at relatively low temperatures. In our case, when we observe the downward deviation from the VRH model in 2D it is likely due to the multiphonon assisted hopping. Since we have many phonons at high

Chapter 4. Synthesis, Structure, Transport and Magnetic Properties of 5d Transition Metal Compounds—Iridates

T , it is easier to hop for the charges.

$$1/\rho = \sigma \propto \gamma t_{ij} \exp[-(T_0/T)^{1/(D+1)}], \quad (4.11)$$

where t_{ij} is the transfer integral and γ is the phonon population.

However, we found this model is not fully satisfactory. The reason is that the Seebeck coefficient would be small if the conduction happens only in the impurity band. Since S is large, there should be a transport over the bandgap. Our data in the narrow range of high temperature part can be fitted by thermally activated behavior,

$$\rho(T) = \rho_0 \exp(E_a/k_B T), \quad (4.12)$$

yielding for $E_g = 2E_a = 60$ meV. So the model which we can compose for the electrical transport is that at high T one has a semiconductor with a band gap of 60 meV, and at low temperatures one gradually shifts over to VRH in 2D.

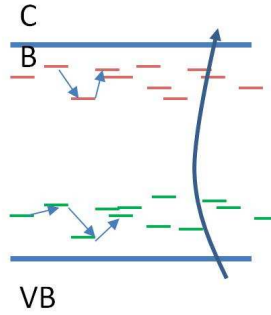


Figure 4.12: A possible schematic of the electronic model.

4.2.4 Magnetic Properties

Bulk magnetic measurements were measured using SQUID in the 2 – 300 K temperature range and up to 5 T. A dozen of plate-like crystals with total mass of 9.4 mg were stacked with common c axis but random orientation in their ab plane.

The susceptibility $\chi = M/H$ for $H = 1$ T parallel (square) and perpendicular (circles) to the c axis are shown in Figure 4.13(a). The high temperature part follows Curie-Weiss behavior while a maximum indicative of magnetic transition is observed at 9 K. Overall, the magnetic behavior appears qualitatively similar between $H \parallel c$ and $H \perp c$.

4.2. Possible unusual spin state of Ir⁴⁺ in Ba₂₁Ir₉O₄₃ single crystal

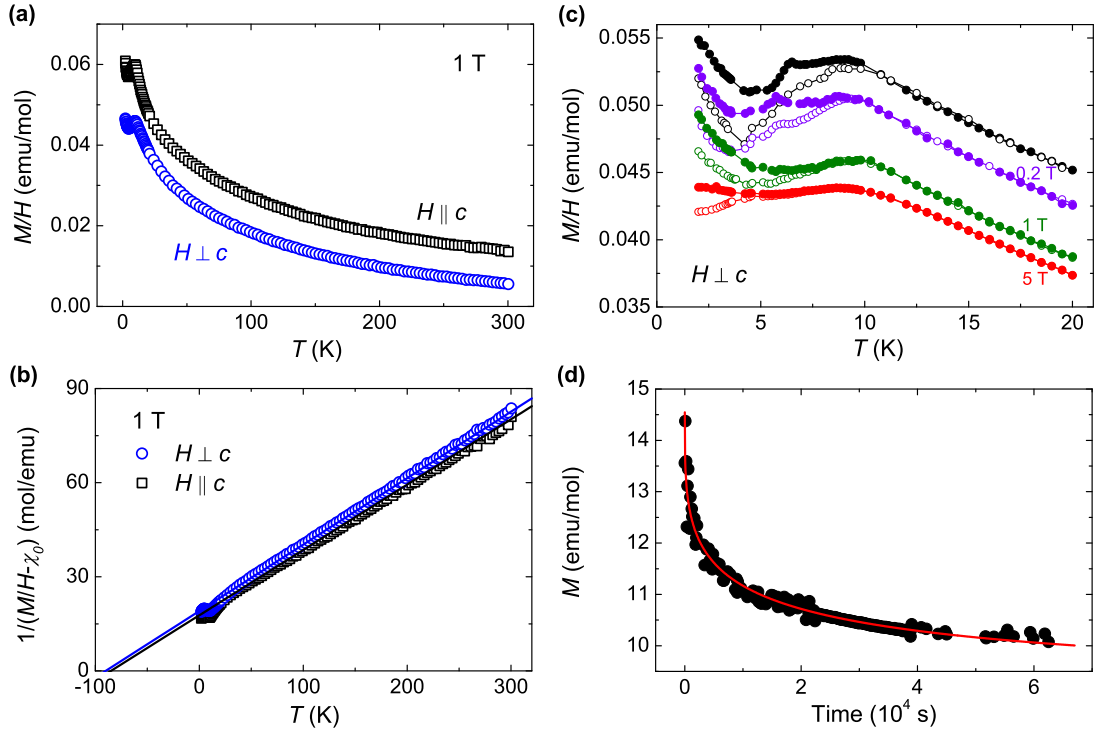


Figure 4.13: (a) Magnetic susceptibility M/H as a function of temperature under $H = 1$ T applied perpendicular and parallel to the c axis, respectively. (b) Inverse magnetic susceptibility $1/(M/H - \chi_0)$ versus temperature in $H = 1$ T. (c) The susceptibility as a function of temperature in various applied fields. (d) The decay of thermoremanent magnetization as a function of time at 5 K.

The data above 100 K was fitted by a Curie-Weiss law,

$$\chi(T) = C/(T - \Theta_{\text{CW}}) + \chi_0, \quad (4.13)$$

yielding for $H \perp c$ a Curie constant $C = 4.72(9)$ emu/mol K, corresponding to an effective moment $\mu_{\text{eff}} = 2.05(2)\mu_{\text{B}}/\text{Ir}$, $\Theta_{\text{CW}} = -90(2)$ K and a temperature independent term $\chi_0 = -6.4 \times 10^{-3}$ emu/mol. For $H \parallel c$ the fit gave $C = 4.8(1)$ emu/mol K, $\mu_{\text{eff}} = 2.07(3)\mu_{\text{B}}/\text{Ir}$, $\Theta_{\text{CW}} = -85(3)$ K and $\chi_0 = 1.2(3) \times 10^{-3}$ emu/mol. Figure 4.13(b) plots $1/(\chi - \chi_0)$ versus T where solid line represents the Curie-Weiss fits. The negative Θ_{CW} suggests dominant antiferromagnetic coupling. The temperature independent term χ_0 is rather large and anisotropic, but similar large and anisotropic values have been reported for other iridates, such as NaIrO₃ [79], Pr₂Ir₂O₇ [78], and Ba₈Al₂IrO₁₄ [69].

The low temperature behavior of $\chi(T)$ in different fields is shown in Fig. 4.13(c). Most notably, a bifurcation for zero-field-cooled (ZFC) and field-cooled (FC) is observed below the 9 K peak while the bifurcation point shifts to lower temperature as the field strength is increased, e.g.,

Chapter 4. Synthesis, Structure, Transport and Magnetic Properties of 5d Transition Metal Compounds—Iridates

the ZFC and FC data split at 5 K in 5 T. A Curie-like tail is observed at lowest temperatures which is substantially suppressed by the field as large as 5 T. Additional small peak is observed in the FC 0.1 T and 0.2 T data around 6 K, which disappears in stronger fields. At low temperatures, relaxation of thermoremanent magnetization is observed as shown in Figure 4.13(d): the sample was cooled to 5 K in 1 T, after which the field was removed and the magnetization was continuously recorded in time t for 18 hours. The decay of thermoremanent magnetization could be fitted to a stretched exponential of the form,

$$M(t) = M_0 \exp(-\alpha t^{1-n}) + M_{\text{bgd}}, \quad (4.14)$$

where M_{bgd} refers to a constant background. The stretch exponent is found to be $n = 0.67$, which is close to that for an ideal spin glass, $n = 2/3$ [98].

Fig. 4.14(a) shows the magnetization as a function of field for $H \perp c$ at different temperatures. The $M(H)$ curve becomes linear with H above 1.5 T in the measured temperature range. A hysteresis loop is barely visible at 5 K, as shown in Fig. 4.14(b) and its inset.

It is surprising that this compound displays an average effective moment of $2.1 \mu_B$, when similar compounds have been reported to exhibit effective moments from 0.2 to $1.3 \mu_B$ [10, 99]. One possible scenario would be that all 4 iridium sites exhibit unusually high moments of $\sim 2 \mu_B$. Below we present another possible interpretation, which merits further experimental and theoretical consideration. Let us start from considering possible valence states for the different iridium environments in $\text{Ba}_{21}\text{Ir}_9\text{O}_{43}$. The most common valence states for Ir ions in oxides are Ir^{3+} , Ir^{4+} , Ir^{5+} , and Ir^{6+} , which may apply to Ir1, Ir2, and Ir3 sites. For the Ir4 sites with the dimers of face-sharing octahedra, one can make reference to the data from a large family of $\text{Ba}_3\text{M}\text{Ir}_2\text{O}_9$, where $M = \text{Mg, Ca, Sc, Ti, Zn, Sr, Zr, Cd}$ and In [99, 10], which have structurally very similar dimer units. In this family, a systematic relation is found between the valence state and Ir-Ir as well as Ir-O distances of the face-sharing octahedra, i.e., larger Ir-Ir and smaller Ir-O distances for higher valence states [99]. For instance, the Ir^{5+} states are stabilized in $\text{Ba}_3\text{ZnIr}_2\text{O}_9$ with the Ir-Ir distance of 2.75 \AA , and similarly for others with $M = \text{Mg, Cd, and Sr}$ [99, 10]. The very similar Ir-Ir distance of 2.74 \AA in $\text{Ba}_{21}\text{Ir}_9\text{O}_{43}$ indicate that Ir^{5+} states are realized on Ir4 sites.

Next we can list possible valence states for Ir ions by imposing the charge neutrality condition for the overall system. For the given chemical formula $\text{Ba}_{21}\text{Ir}_9\text{O}_{43}$, we find that only three valence configurations are possible (see below), which are listed in Table 4.11.

- (1) The most common valence state of Ir ions: Ir^{3+} , Ir^{4+} , Ir^{5+} , Ir^{6+}
- (2) The total number of Ir ions is 9 and the total valence of Ir ions is +44 (in $\text{Ba}_{21}\text{Ir}_9\text{O}_{43}$, Ba ions are +2 and O ions are -2)

4.2. Possible unusual spin state of Ir^{4+} in $\text{Ba}_{21}\text{Ir}_9\text{O}_{43}$ single crystal

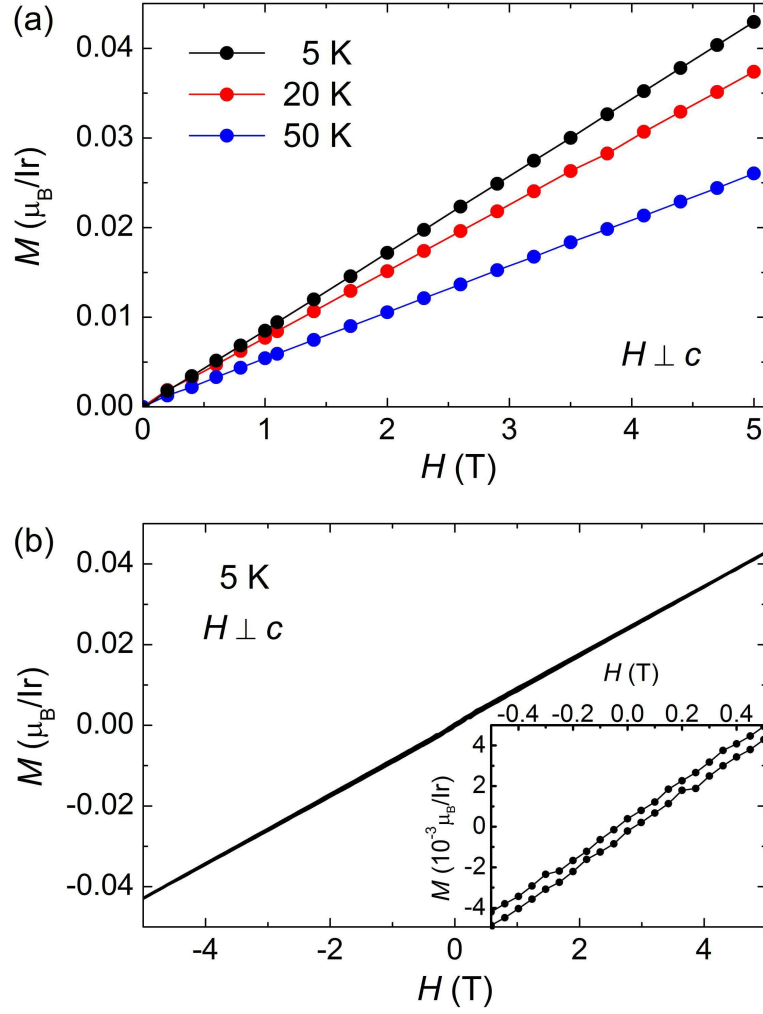


Figure 4.14: (a) Isothermal magnetization as a function of field for different temperatures. (b) Magnetization loop measurement at 5 K with barely visible hysteresis, where a zoom-in is shown in the inset.

(3) Wyckoff Symbol: Ir1 – 2c, Ir2 – 2d, Ir3 – 2b, Ir4 – 12i, so the number of each Ir ion: $N(\text{Ir1}) = 1$, $N(\text{Ir2}) = 1$, $N(\text{Ir3}) = 1$, $N(\text{Ir4}) = 6$

Based on above three conditions, we obtained,

$$3N(\text{Ir}^{3+}) + 4N(\text{Ir}^{4+}) + 5N(\text{Ir}^{5+}) + 6N(\text{Ir}^{6+}) = 44, \quad (4.15)$$

$$N(\text{Ir}^{3+}) + N(\text{Ir}^{4+}) + N(\text{Ir}^{5+}) + N(\text{Ir}^{6+}) = 9, \quad (4.16)$$

Chapter 4. Synthesis, Structure, Transport and Magnetic Properties of 5d Transition Metal Compounds—Iridates

For the two regular octahedral sites, Ir1 and Ir3, it is found that their Ir-O distances are very similar, 1.95(3) Å and 1.90(3) Å, respectively. This indicates that they likely adopt the same valence state, excluding the combination A. To discriminate between combinations B and C, we consider the charge balance within the layer II. As can be seen from Fig. 4.8, there are no shared oxygens between neighbouring iridium ions within a layer, with Ba²⁺ ions being found between Ir-O clusters. For both the Ir1 and Ir3 octahedral units in combination B, each Ir⁵⁺ ions are surrounded by six O²⁻ ions so that the total charge ($Q_{\text{oct}}^{\text{B}}$) sums up as $5 + 6 \times (-2) = -7$. Likewise, for the Ir2 triangular pyramidal unit, each Ir⁴⁺ ions surrounded by four O²⁻ ions provide the total charge ($Q_{\text{pyr}}^{\text{B}}$) of $4 + 4 \times (-2) = -4$. However, for C these values become much more disproportionate, $Q_{\text{oct}}^{\text{C}} = -8$ and $Q_{\text{pyr}}^{\text{C}} = -2$, which appears rather unlikely. Therefore, we conclude that the combination B is the most likely valence configurations.

We can now turn our attention to the consideration of magnetic moments residing on individual iridium sites. The values of effective moments for the case B, for instance, are calculated by using

$$(\mu_{\text{eff}}/\mu_{\text{B}})^2 N_{\text{Ir}} = \mu_{\text{pyr}}^2 N_{\text{pyr}} + \mu_{\text{oct}}^2 N_{\text{oct}} + \mu_{\text{dim}}^2 N_{\text{dim}}, \quad (4.17)$$

where N_{Ir} is the total number of Ir sites, $N_{\text{pyr}} = 1$, $N_{\text{oct}} = 2$, and $N_{\text{dim}} = 6$ are respectively the numbers of sites for Ir⁴⁺ in triangular pyramid, Ir⁵⁺ in octahedra, and Ir⁵⁺ in dimer. If as predicted octahedrally coordinated Ir⁵⁺ is in a spin-orbit coupled non-magnetic state [49], all the magnetic moment deduced from the Curie constant must be assigned to the Ir⁴⁺ ions on Ir2 site. This would lead to a rather large effective moment of $6.15 \mu_{\text{B}}$. This value is only slightly reduced by adopting the more likely literature values for Ir⁵⁺ discussed above. For instance,

Table 4.10: Calculation of valence state of Ir ions.

| | Ir1 ($N=1$) | Ir2 ($N=1$) | Ir3 ($N=1$) | Ir4 ($N=6$) |
|---|--|---------------|--------------------------|------------------|
| 1 | $Q(\text{Ir1}+\text{Ir2}+\text{Ir3})=26$ | | no solution | Ir ³⁺ |
| 2 | $Q(\text{Ir1}+\text{Ir2}+\text{Ir3})=20$ | | no solution | Ir ⁴⁺ |
| 3 | $N(\text{Ir}^{5+}) = 2,$ | | $N(\text{Ir}^{4+}) = 1$ | Ir ⁵⁺ |
| 4 | $N(\text{Ir}^{4+}) = 2,$ | | $N(\text{Ir}^{6+}) = 1$ | Ir ⁵⁺ |
| 5 | $N(\text{Ir}^{3+}) = 1,$ | | $N(\text{Ir}^{5+}) = 1,$ | Ir ⁵⁺ |
| 6 | $Q(\text{Ir1}+\text{Ir2}+\text{Ir3})=8$ | | no solution | Ir ⁶⁺ |

Table 4.11: Valence states in octahedral and triangular pyramid environment for the different Ir ions.

| | Ir1 | Ir2 | Ir3 | Ir4 |
|---|-----|-----|-----|-----|
| A | 3+ | 5+ | 6+ | 5+ |
| B | 5+ | 4+ | 5+ | 5+ |
| C | 4+ | 6+ | 4+ | 5+ |

4.2. Possible unusual spin state of Ir^{4+} in $\text{Ba}_{21}\text{Ir}_9\text{O}_{43}$ single crystal

when $0.2 \mu_B/\text{Ir}$ for the dimers [10] and $0.91 \mu_B/\text{Ir}$ for the regular octahedra [51] are used, the moment expected for each Ir^{4+} becomes $6.0 \mu_B$ which is still fairly large. Interestingly it is close to the expected value of $5.9 \mu_B$ for a state $S = 5/2$.

To the best of our knowledge, Ir^{4+} within the triangular pyramid environment has not yet been reported or considered theoretically. V. M. Katukuri, N. E. Shaik and O. V. Yazyev [70] performed the preliminary *ab initio* many-body configuration interaction calculations [100] on IrO_4 unit to understand the electronic multiplet structure of the Ir^{4+} ion at Ir2 site. The calculations indicate an orbitally nondegenerate low-spin ground state. As a result, the spin-orbit coupling in the $5d$ Ir atom, though strong, has little effect on the ground state - less than 20% contribution from the excited orbital states. However, a distortion, e.g., the Ir^{4+} atom moving towards the tetrahedral position of the triangular pyramid, could help result in a high-spin $S = 5/2$ ground state. In fact, our calculations on an ideal IrO_4 tetrahedra with Ir-O bond lengths of 1.9 \AA (\approx average of the Ir-O bond lengths at the Ir2 site) show that the 6A_1 ($S = 5/2$) state is rather close, $\sim 0.33 \text{ eV}$, to the low-spin 2T_2 ground state of the tetrahedral point group symmetry. The high-spin state could then be stabilized by further distortion, interactions, or other correlated effects, which we leave for future work.

4.2.5 Electron Spin Resonance

B. Nafradi et al. performed the Electron spin resonance (ESR) measurements on the stacked crystals using a Bruker Elexys E500 continuous wave spectrometer at 9.4 GHz, equipped with a He-gas flow cryostat. At room temperature, a single paramagnetic ESR line was observed. The g factor and its anisotropy were obtained by recording the line position as the applied field orientation was varied with respect to the crystallographic axes. Figure 4.15(a) shows the obtained g factor anisotropy, which exhibits a characteristic $\cos^2 \theta$ angular dependence as the field orientation varies from $H \parallel c$ to $H \perp c$. The principal values of the g factor are found as $g_{\parallel c} = 2.37$ and $g_{\perp c} = 2.24$. The g factor anisotropy in the ab plane was smaller than the ESR linewidth of 20 mT which gives an upper bound of 0.05 for the ab plane anisotropy.

The low temperature ESR reveals strong dependence on field strength, direction, and history in magnetic behavior. For instance, a rather strong ESR signal is observed at 6 K when cooled in a field $H \parallel c$, while no ESR response is observed in ZFC procedure, as shown in the upper panel of Fig. 4.15(b). The ESR signal amplitude is further found to increase with the applied field strength: red and blue lines for 0.33 and 1.5 T, respectively, in the upper panel of Fig. 4.15(b). Similar behavior was also observed for $H \perp c$ while only 1.5 T FC data is shown in the lower panel of Fig. 4.15(b). Interestingly, the ESR signal becomes lost when the measurement field is rotated away by 90° from the poling direction in the FC procedure, as shown in the lower panel of Fig. 4.15.

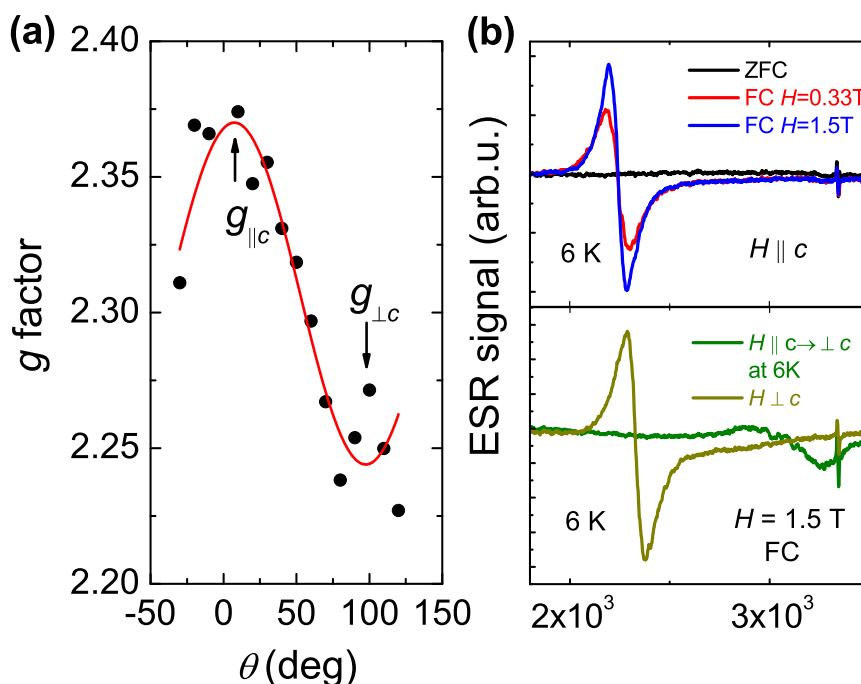


Figure 4.15: (a) Angular dependence of the g factor at room temperature. (b) Upper: ESR spectra at 6 K measured in ZFC and FC conditions for $H \parallel c$. Lower: FC ESR spectra at 6 K where the field has been either applied along c axis then rotated toward ab plane, or applied from the beginning into the ab plane.

The strong field dependence in the ESR results, which might be explained by the presence of magnetic domains of small volume. For instance, ZFC procedure would result in a random arrangement of the domains where the paramagnetic spins in the vicinity of domain walls could couple to inhomogeneous stray field. Cooling the sample in a poling field instead would result in a development of domains with sublattice magnetization pointing perpendicular to the poling field. These Bloch domain walls will not induce stray fields parallel to the poling field, thus the regions without inhomogeneous broadening will give rise to an ESR line. Increasing the magnetic field of the FC procedure shifts the domain imbalance [101], increasing the domain size and thus the signal. The Bloch walls, however, induce inhomogeneous fields in the direction perpendicular to the poling field. Rotating the magnetic field perpendicular to the poling direction results in the disappearance of the ESR due to the inhomogeneous broadening. This scenario is also compatible with the difference in FC and ZFC susceptibility results.

4.2.6 Conclusion

We synthesized single crystals of a novel iridate $\text{Ba}_{21}\text{Ir}_9\text{O}_{43}$ which contains two different Ir layers of triangular lattice. One layer consists of Ir_2O_9 dimers while the other is made of two regular Ir-O octahedra and one triangular pyramid. The triangular pyramids with presumably Ir^{4+} is suggested to carry substantial magnetic moments as large as $\sim 6\mu_B/\text{Ir}$, while the dimers and octahedra with Ir^{5+} may hold only small moments. The compound is an insulator with antiferromagnetic Curie-Weiss behavior, where a magnetic transition is suppressed down to low temperature of 9 K despite the large Curie-Weiss temperature of -90 K. The difference between field-cooled and zero-field cooled susceptibility and ESR data may suggest the presence of magnetic domains.

4.3 Pressure induced two-dimensional superconductivity in $\text{Ir}_{0.95}\text{Pt}_{0.05}\text{Te}_2$

4.3.1 Motivation for This Work

Recently, more and more studies have been focused on transition-metal dichalcogenides because of their interesting quasi two-dimensional electronic properties. Superconductivity and charge-density-wave order are often found in these systems either co-existing or as neighbors in the phase diagram. In heavy element dichalcogenides spin-orbit interaction is expected to add an additional component to define the electronics. In this context, IrTe_2 has been studied intensively recently. IrTe_2 crystallizes in a trigonal structure with the space group

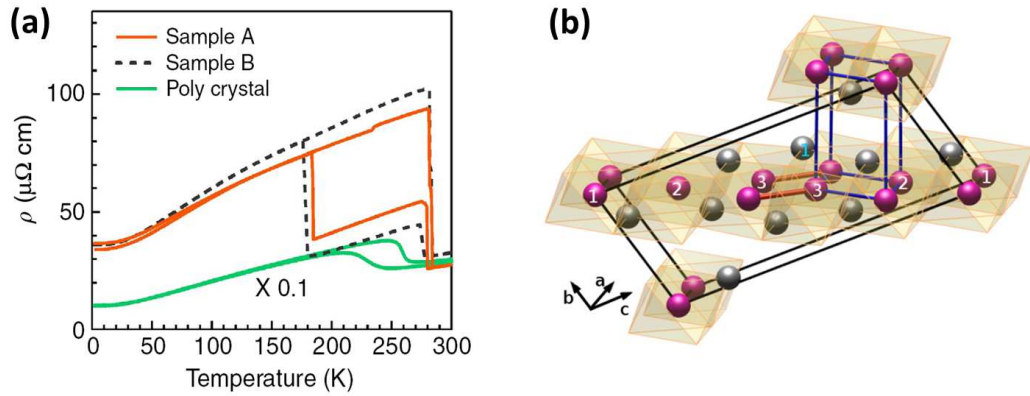


Figure 4.16: (a) The comparison of the resistivity as a function of temperature between single crystals and polycrystal of IrTe_2 . (b) The structure of IrTe_2 at room temperature and low temperature. The high temperature and low temperature unit cells are drawn by blue and black solid lines, respectively, cited from [22, 23].

$P\bar{3}m1$ at room temperature, where the formation of Ir triangular lattice appears and the three

Chapter 4. Synthesis, Structure, Transport and Magnetic Properties of 5d Transition Metal Compounds—Iridates

Ir-Ir bonds are equivalent [24, 102]. At 250 K, IrTe₂ undergoes a first-order phase transition and crystallizes in a monoclinic structure with the space group $C2/m$ [103, 104], as shown in Figure 4.16. At low temperature IrTe₂ shows superconductivity with a $T_{sc} = 3.1$ K.

Subsequently, Pyon et al. reported Ir_{1-x}Pt_xTe₂ single crystals. The first-order transition temperature in IrTe₂ decreases and a new superconducting phase appears with more Pt doping, as shown in Figure 4.18[24]. Kiswandhi et al. reported the transport measurements of Ir_{1-x}Pt_xTe₂ under pressure. The first-order transition temperature increases while the superconducting transition temperature decreases with applying pressure [105]. Just as in high-temperature superconductor systems (cuprate and pnictides) a key question is how and why these materials can tuned from their parent compound to the superconducting state.

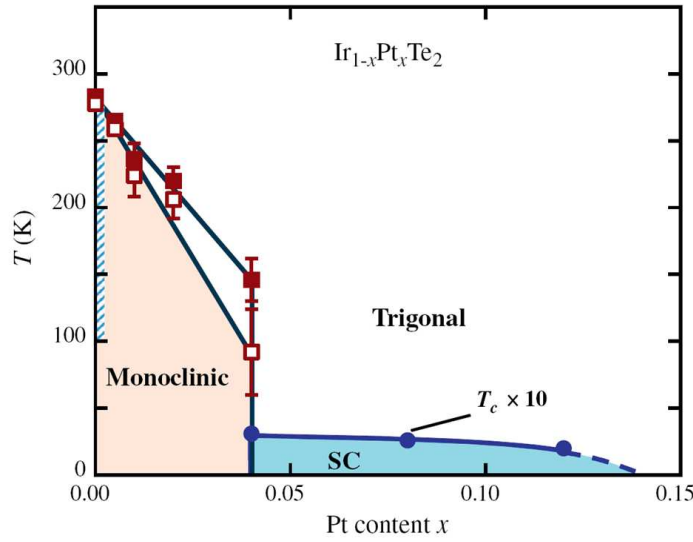


Figure 4.17: Phase diagram of Ir_{1-x}Pt_xTe₂ [24].

Here we present resistivity study of Ir_{1-x}Pt_xTe₂ ($x = 0.04$ and $x = 0.05$) under hydrostatic pressure. The Ir_{0.95}Pt_{0.05}Te₂ is a pure superconductor without any signs of charge order, and near the quantum critical point of the Ir_{1-x}Pt_xTe₂ phase diagram, as shown in Figure 4.17. We show that under pressure, the Ir dimer configuration is stabilized. Once this charge order is introduced, superconductivity undergoes a dimensionality cross-over from 3D to 2D. It is furthermore demonstrated that exactly this phenomenon is present in Ir_{0.96}Pt_{0.04}Te₂ under ambient pressure condition.

4.3.2 Synthesis and Crystal Structure

Single crystals of Ir_{0.95}Pt_{0.05}Te₂ were grown by Pyon et.al using a self-flux technique [106, 105]. Representative single crystals of Ir_{0.95}Pt_{0.05}Te₂ is shown in Figure 4.18.

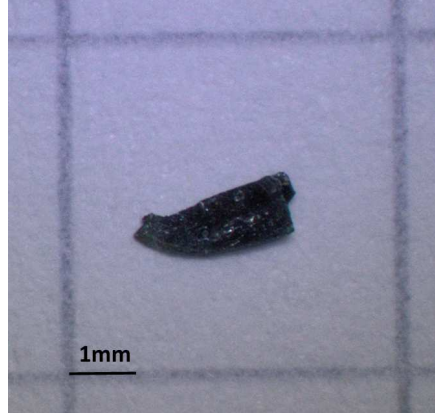


Figure 4.18: Representative single crystals of $\text{Ir}_{0.95}\text{Pt}_{0.05}\text{Te}_2$.

4.3.3 Resistivity for $\text{Ir}_{0.95}\text{Pt}_{0.05}\text{Te}_2$

In plane resistivity of $\text{Ir}_{0.95}\text{Pt}_{0.05}\text{Te}_2$ has been measured as a function of temperature T and hydrostatic pressure p . The crystals were mounted in a pistoncylinder-type pressure cell with Daphne 7373 as the pressure transmitting medium to achieve a nearly hydrostatic pressure up to 2.3 GPa. The pressure at low temperature was determined from the resistive superconducting transition of Pb. The electrical resistivity was measured by four-probe method using Quantum Design PPMS-14T in a temperature range of 2 to 300 K.

Figure 4.19 shows temperature dependence of resistivity ρ for $\text{Ir}_{0.95}\text{Pt}_{0.05}\text{Te}_2$ at various pressures. The crystal shows no detectable anomaly or hysteresis for $P < 10.0$ kbar, as shown in Figure 4.19(a). However, for pressures greater the critical pressure of structural phase transition P_c , i.e. 10.0 kbar, the thermal hysteresis reappeared at T_{sp} . The high-temperature resistivity is measured upon heating and cooling. The difference between the curves clearly shows the presence of hysteresis associated with the anomaly at T_{sp} . First at $P = 12.1$ kBar, a clear hysteresis loop is observed (Figure 4.19(b)). We define T^w and T^c as the temperature scales below which the warming and cooling curves differs from resistivity versus temperature measured for $P < P_c$. At this particular pressure (12.1 kBar), $T^w = 170$ K and $T^w - T^c = 60$ K. Increasing the pressure to 17.0 kBar, the hysteresis loop moves upward in temperature ($T^w = 205$ K). Furthermore, the hysteresis loop at this pressure has a fundamentally different shape. Even the loop area has increased significantly, $T^w - T^c$ is diminished to just 15 K. At the maximum of pressure we applied, 23.0 kbar, T^w increases to 225 K, as shown in Figure 4.19(b).

The insets of Figure 4.19 show that T_{sc} decreases with increasing pressure. Crossing the critical pressure p_c , superconductivity initially appears to maintain the $dT_c/dp =$ tendency. However, as the pressure is increased from 12 to 17 kBar, the superconducting transition is significantly broader. In addition, the pressure dependence of the residual resistivity ρ_0 in the normal state

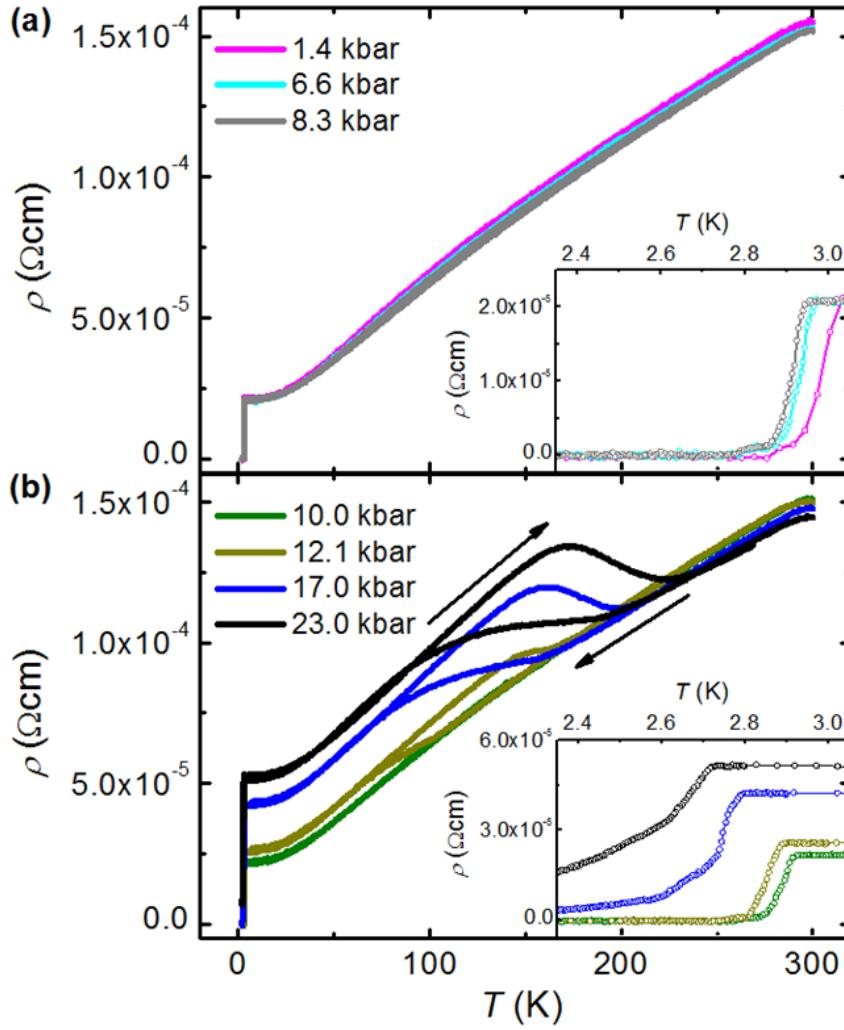


Figure 4.19: (a) Temperature dependence of resistivity for $\text{Ir}_{0.95}\text{Pt}_{0.05}\text{Te}_2$ at various pressures. (a) The pressures are below the critical pressure for structure phase transition. (b) The pressures are above the critical pressure. The insets show the superconducting transition part of each corresponding figure.

also exhibits a distinct change between 10.0 and 12.1 kbar. Below $P_c = 10.0$ kbar there is no significant change for ρ_0 and the normal state resistivity that for our sample display a residual value of $20 \mu\Omega\text{cm}$. However for $P > P_c$, ρ_0 increases upon applying pressure and at 23 kBar ρ_0 is more than twice the value at $P = P_c$.

Figure 4.20 shows temperature dependence of ρ_0 and A for $\text{Ir}_{0.95}\text{Pt}_{0.05}\text{Te}_2$ at various pressures. The low-temperature ($T < 40$ K) ρ can be fitted to $\rho(T) = \rho_0 + AT^n$. The coefficient A and exponent n which represent the inelastic scattering, as well as the residual resistivity ρ_0 characterizing the elastic scattering have been plotted as functions of pressure. We found that:

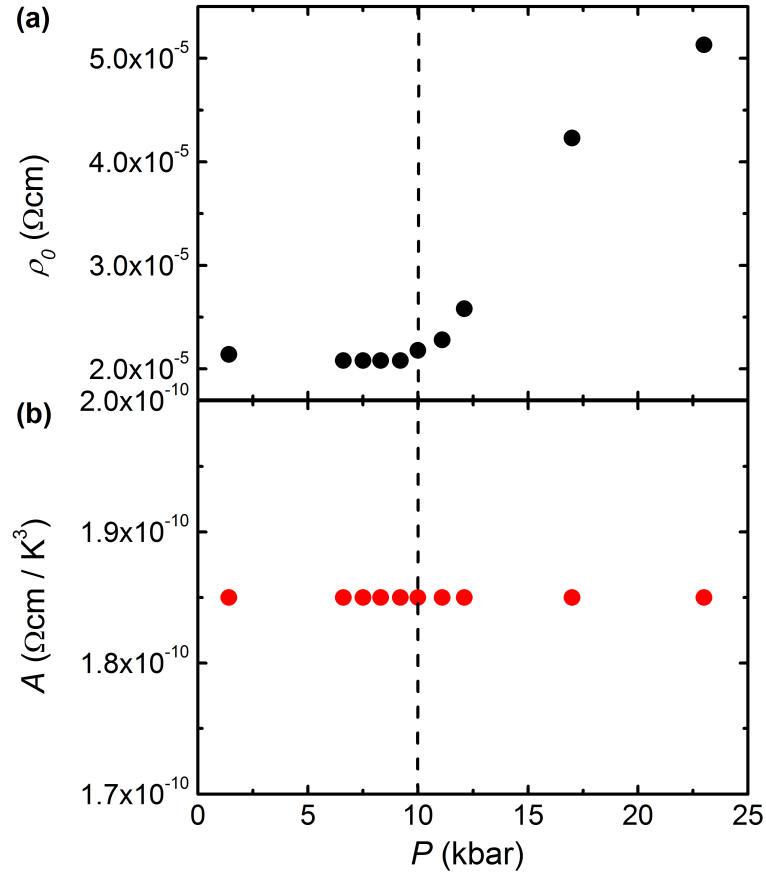


Figure 4.20: (Color online) (a) Residual resistivity $\rho_0 = \rho(0)$ versus applied pressure. (b) Inelastic component of the resistivity versus applied pressure.

(1) The inelastic part of the resistivity follows a power law AT^n in which $A = 1.85 \times 10^{-10} \text{ } \Omega\text{cm}/\text{K}^3$ and $n = 3$. There is no significant change at various pressures which indicates the inelastic scattering part does not change across P_c .

(2) Using pressure as controlled parameter, ρ_0 is pressure-independent below the critical pressure and increases with increasing pressure above P_c , which indicates the elastic scattering part changes across P_c .

Things get more interesting when we found the non-zero resistivity state below T_c^{2D} , as shown in the inset of Figure 4.21 (b). At high-pressure $p = 17 \text{ kBar}$, the resistive transition however broadens. This effect resembles that of a Kosterlitz-Thouless transition where

$$\rho(T) = a \exp \left(\frac{-b}{\sqrt{(T - T_c^{3D})/T_c^{3D}}} \right) \quad (4.18)$$

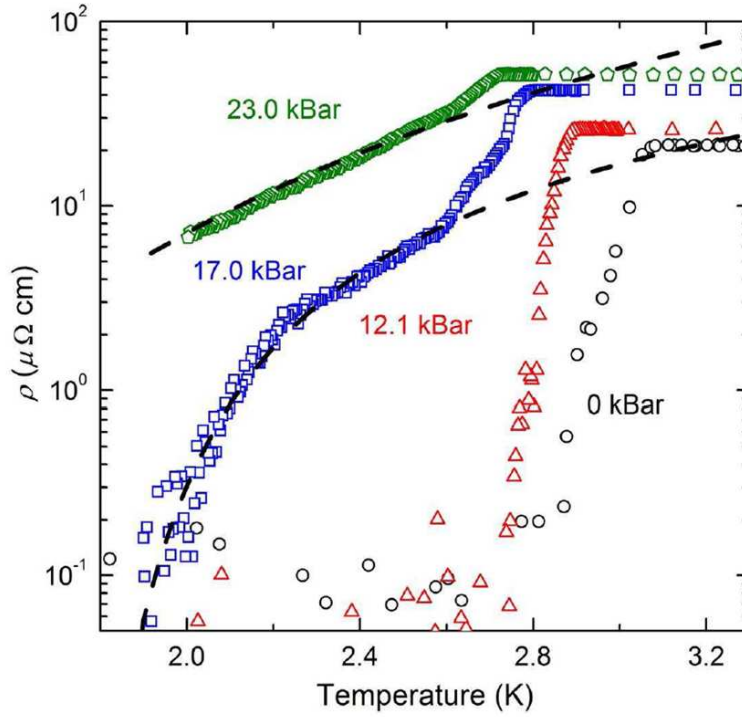


Figure 4.21: (Color online) The superconducting transition as a function of temperature under different pressures. The black dashed lines correspond to fits to Eq. 4.14.

where a and b are constants and T_c^{3D} is the transition temperature of 3D superconductivity. The above equation [107] explains that the ρ of a two-dimensional superconductor above the BKT transition temperature, where true superconductivity is destroyed by phase fluctuations because the thermally-excited vortex-antivortex pairs are unbound [108, 109]. For $\text{Ir}_{0.95}\text{Pt}_{0.05}\text{Te}_2$, the fits yield $T_c^{3D} = 1.7$ K at $P = 17$ kBar and $T_c^{3D} = 0.3$ K at $p = 23$ kBar, as shown in Figure 4.21, this provide a good description of the low-temperature part of the transition. The implication of the interpretation is that (for $p = 17$ kBar) two-dimensional superconductivity appears between the $T_c(\text{onset})$ and T_c^{3D} . Only below T_c^{3D} , the complete three-dimensional superconducting state is obtained.

The overall behavior of $\text{Ir}_{0.95}\text{Pt}_{0.05}\text{Te}_2$ are summarized in Figure 4.22. The structural transition temperature is enhanced and the superconducting transition temperature is reduced, as shown in Figure 4.22 (a). In Figure 4.22 (b), we thus propose a superconducting phase diagram where the three-dimensional superconducting phase is gradually suppressed as a function of pressure but replaced by two-dimensional superconductivity.

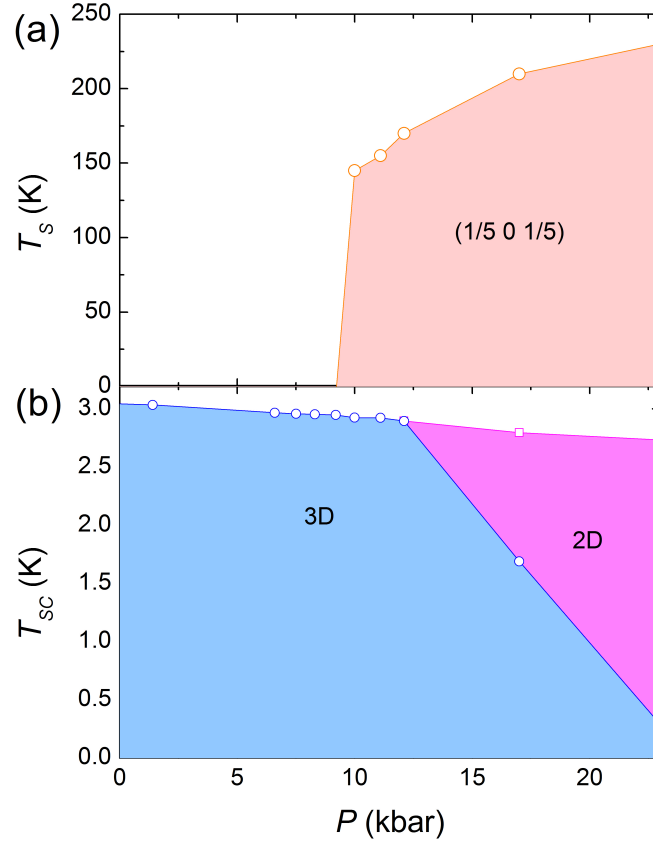


Figure 4.22: (Color online) Pressure - temperature phase diagrams of the (a) Ir-dimerization and (b) superconductivity.

4.3.4 Resistivity for $\text{Ir}_{0.96}\text{Pt}_{0.04}\text{Te}_2$

In plane resistivity of $\text{Ir}_{0.96}\text{Pt}_{0.04}\text{Te}_2$ has been measured as a function of temperature T . Figure 4.23 shows temperature dependence of resistivity ρ for $\text{Ir}_{0.96}\text{Pt}_{0.04}\text{Te}_2$ and $\text{Ir}_{0.95}\text{Pt}_{0.05}\text{Te}_2$ under ambient pressure.

$\text{Ir}_{0.95}\text{Pt}_{0.05}\text{Te}_2$ shows no detectable anomaly or hysteresis under ambient pressure. For $\text{Ir}_{0.96}\text{Pt}_{0.04}\text{Te}_2$, the difference between the curves clearly shows the presence of hysteresis associated with the anomaly at T_{sp} . At this particular component ($x = 0.04$), $T^w = 140$ K and $T^w - T^c = 60$ K, as shown in Figure 4.23(a). D. Destraz and J. Chang performed the resistivity measurement at low temperature down to 0.3 K. $\text{Ir}_{0.95}\text{Pt}_{0.05}\text{Te}_2$ shows very sharp superconductivity transition around 2.9 K and the resistive transition broadens for $\text{Ir}_{0.96}\text{Pt}_{0.04}\text{Te}_2$. This effect of $\text{Ir}_{0.96}\text{Pt}_{0.04}\text{Te}_2$ can also be fitted by Kosterlitz-Thouless transition and the fit yields $T_c^{3D} = 0.15$ K, as shown in Figure 4.23 (b). The implication of the interpretation is that three-dimensional superconductivity appears below 0.15 K for $\text{Ir}_{0.96}\text{Pt}_{0.04}\text{Te}_2$.

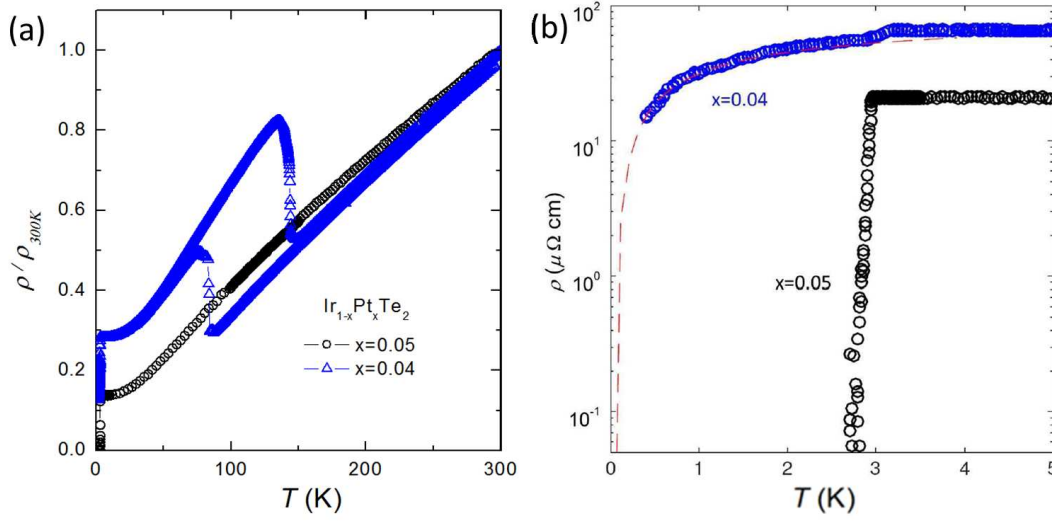


Figure 4.23: (Color online) The resistivity as a function of temperature for $\text{Ir}_{0.96}\text{Pt}_{0.04}\text{Te}_2$ and $\text{Ir}_{0.95}\text{Pt}_{0.05}\text{Te}_2$ under ambient pressure.

The overall behavior of $\text{Ir}_{1-x}\text{Pt}_x\text{Te}_2$ revealed by pressure effects and by doping effects are summarized in Figure 4.24. The structural transition temperature is enhanced and the three-dimensional superconducting phase is gradually suppressed but replaced by two-dimensional superconductivity as a function of pressure P . On the other hand, the structural transition temperature is reduced and the two-dimensional superconducting phase is gradually suppressed but replaced by three-dimensional superconductivity as a function of Pt doping x .

4.3.5 Conclusion

We report the pressure-dependent resistivity measurements of $\text{Ir}_{0.95}\text{Pt}_{0.05}\text{Te}_2$ and the ambient pressure resistivity measurements of $\text{Ir}_{0.96}\text{Pt}_{0.04}\text{Te}_2$. After applying the pressure, the structural phase transition temperature increases and the superconducting transition temperature decreases. The results reveal that the competition between the high T structural phase transition and the low T superconductivity. The residual resistivity ρ_0 is pressure-independent below the critical pressure and increases with increasing pressure above P_c . The low temperature superconductivity undergoes a dimensionality cross-over from 3D to 2D.

4.3. Pressure induced two-dimensional superconductivity in $\text{Ir}_{0.95}\text{Pt}_{0.05}\text{Te}_2$

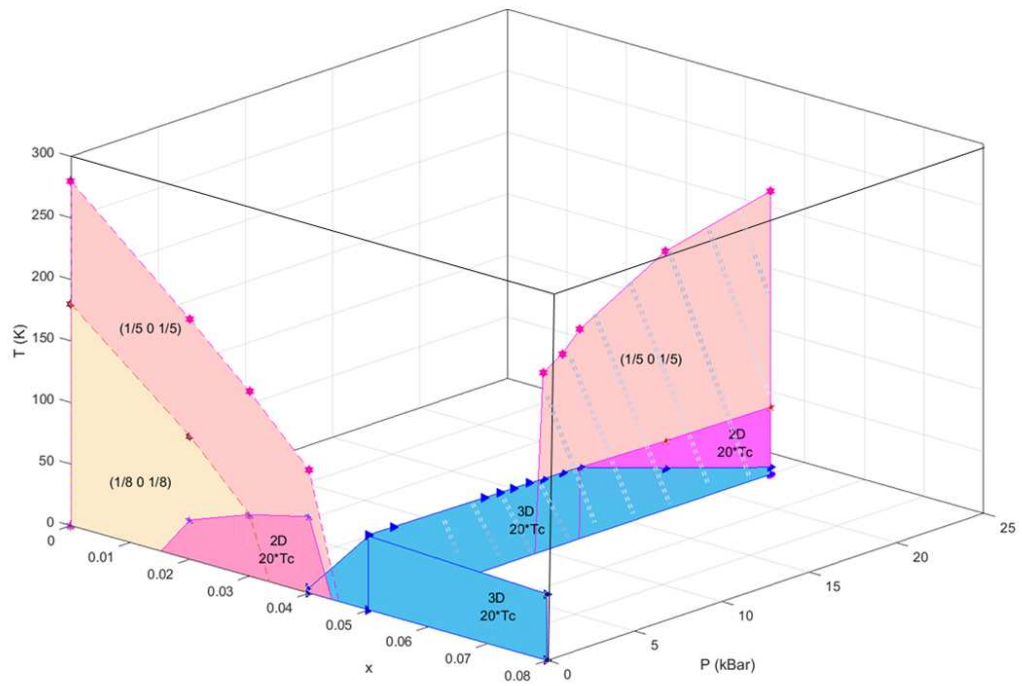


Figure 4.24: (Color online) Three dimensional phase diagrams of the (a) Ir-dimerization and (b) superconductivity.

5 Orbitally quenched $S = 1/2$ magnetic insulator MoPO_5

The results of this chapter are partly copies from the one paper below: L. Yang, M. Jeong, P. Babkevich, et al, Orbitally quenched $S = 1/2$ magnetic insulator MoPO_5 , in preparation.

5.1 Motivation for This Work

The $4d$ transition-metal oxides naturally bridge two different regimes of the strongly correlated $3d$ compounds and the $5d$ compounds with strong spin-orbit coupling [49]. To what extent the $4d$ compounds represent the either regime or display original properties are largely open questions of current interest [83]. Most notably, for instance, it is intriguing that seemingly similar Ca_2RuO_4 and Sr_2RuO_4 display totally different behavior: the former is a Mott insulator [31, 32, 33] while the latter is metallic and becomes superconducting at low temperature [33, 34]. Despite such interest, however, purely $4d$ quantum magnets, especially other than ruthenates, without a complication by other types of magnetic orbitals, e.g., $3d$ or $4f$, are relatively rare.

Among a few known $4d^1$ magnets is a molybdenum phosphate MoPO_5 [110]. The MO_6 octahedra with Mo^{5+} ions are connected via corner sharing to form a chain along the crystallographic c axis of the tetragonal structure (Figure 5.1(a)), and these chains are further coupled next to each other via corner sharing of PO_4 tetrahedra (Figure 5.1(b)) [110, 111]. Previous susceptibility data on a powder shows a Curie-Weiss behavior with $\theta_{\text{CW}} = 8$ K without a sign of low-dimensionality and a magnetic transition at 18 K [112]. ^{31}P NMR on a powder shows a substantial exchange through the PO_4 tetrahedra while a sharp powder ESR line infers rather isotropic g factor [112]. However, no study on the magnetic properties of a single crystal as well as the magnetic structure in the ordered phase have been reported. In addition, discussion on the possible spin-orbit coupling effects is absent.

Here we report the synthesis of large single crystals of MoPO_5 , and present their magnetic

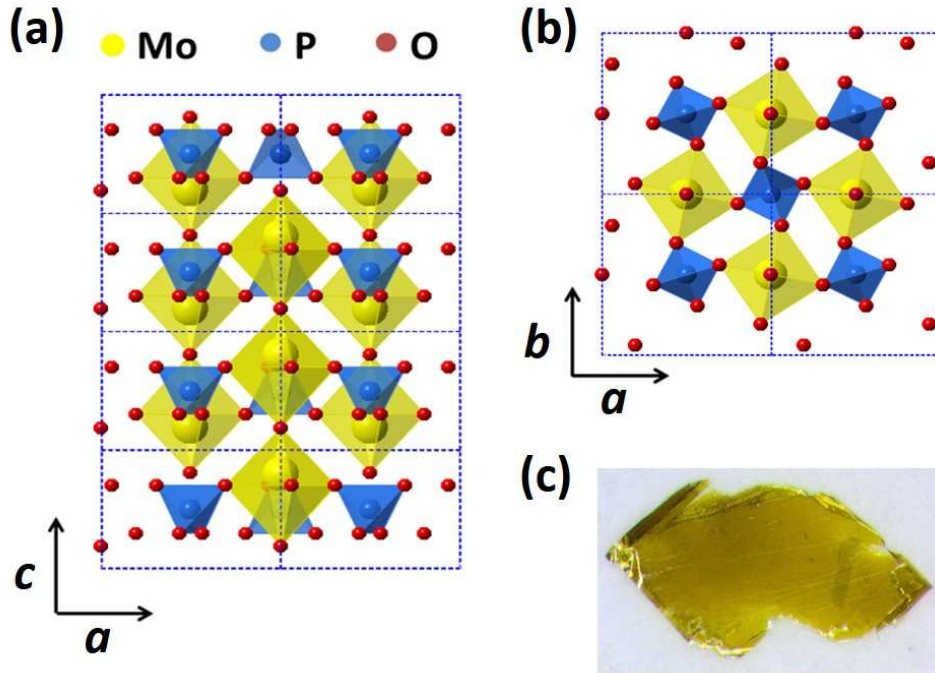


Figure 5.1: (a) Crystal structure projected onto the ac planes showing a chain-like arrangement of MoO_6 octahedra (yellow) and (b) onto the ab planes showing the coupling between the chains via PO_4 tetrahedra (blue). Dashed lines represent the unit cells. (c) Photograph of a representative single crystal.

and thermodynamic properties using specific heat, susceptibility, magnetization, and ESR measurements.

5.2 Synthesis and Crystal Structure

High-quality single crystals of MoPO_5 were synthesized following the procedure described in Ref. [110]. By using H_3PO_4 Orthophosphoric acid 85% Carlo Erba liquid and MoO_3 basis Molybdic acid $\geq 85\%$ Sigma-Aldrich powder as source, a viscous mixture of 13.1 g powder and 6 ml liquid was heated at 1000°C in Al_2O_3 crucible for 20 min and then rapidly cooled down. After being cooled to room temperature, the resulting dark-blue solid was dissolved in hot water. The mixture was heated at 200°C . After 2 hours the tiny yellow transparent crystals were obtained in a plate-like shape. Heating the mixture at 200°C for 1 month by filling the hot water, large-sized crystals were obtained with a typical dimension of $3 \times 2 \times 0.4 \text{ mm}^3$.

Single-crystal x-ray diffraction data was collected at room temperature. The crystal belongs to a space group of $P4/n$ with the lattice parameters of $a = b = 6.2044 \text{ \AA}$ and $c = 4.3003 \text{ \AA}$ in agreement with Ref. [110]. The direction normal to the plate was found to coincide with the c

axis.

5.3 Specific heat

Specific heat was measured by M. Kriener using a QuantumDesign PPMS in the temperature range of 2 – 150 K in zero field and 14 T. Figure 5.2(a) presents the specific heat C_p from 150 K

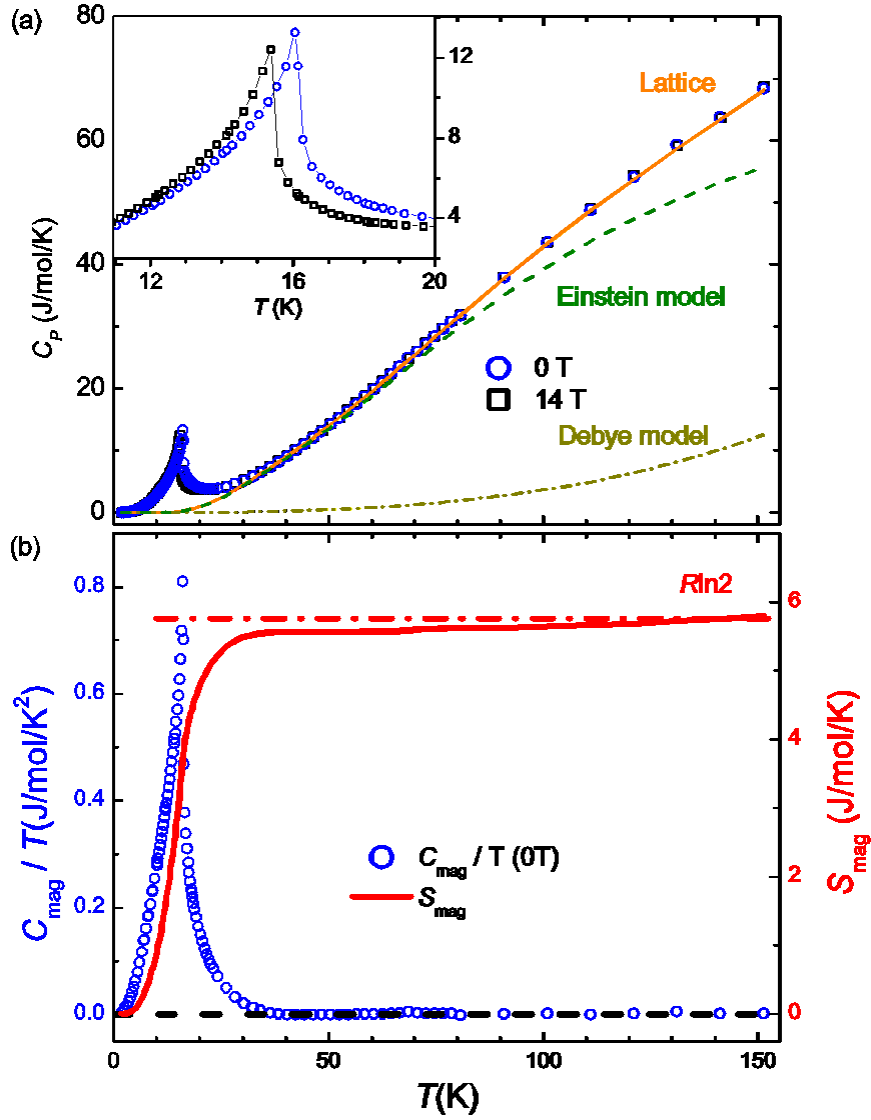


Figure 5.2: (a) Specific heat C_p as a function of temperature in zero field (circle) and in 14 T (square). Solid line represents the best fit of the simulated lattice contribution using the Debye (dash-dotted line) and Einstein (dashed line) terms. Inset provides an enlarged view of the low temperature region. (b) Left axis: magnetic part of the specific heat, C_{mag} , divided by temperature (circle). Right axis: solid line is the entropy calculated from the C_{mag} .

down to 2 K in zero field (circle) and 14 T (square). In both cases, C_p decreases monotonically with lowering temperature down to 25 K where the two appear indistinguishable. In zero field a pronounced peak is found at 16 K, while the peak appears at a slightly lower temperature of 15.4 K in 14 T. These peaks correspond to a transition into a long range ordered phase, as will be shown in later sections.

In order to extract the magnetic part of the specific heat, C_{mag} , and deduce the corresponding entropy S_{mag} , we simulate the lattice contribution using high temperature data by taking into account the Debye and Einstein contributions. We fit the C_p data above 30 K by a lattice-only model

$$C_p = C_D + \sum_i C_{E,i}, \quad (5.1)$$

where C_D and $C_{E,i}$ represent the Debye and Einstein terms, respectively. The Debye term is expressed as

$$C_D = 9n_D R \left(\frac{T}{\Theta_D} \right)^3 \int_0^{\Theta_D/T} \frac{x^4 e^x}{(e^x - 1)^2} dx, \quad (5.2)$$

and the Einstein term as

$$C_E = 3n_E R \frac{y^2 e^y}{(e^y - 1)^2}, \quad y \equiv \Theta_E/T, \quad (5.3)$$

where Θ_D and Θ_E are the Debye and Einstein temperatures, respectively, and the sum $n_D + n_E$ is the total number of atoms per formula unit. The best fit, using one Debye and two Einstein terms, yields the characteristic temperatures $\Theta_D = 1177$ K, $\Theta_{E,1} = 372$ K, and $\Theta_{E,2} = 154$ K, and the numbers $n_D = 4$, $n_{E,1} = 2$, $n_{E,2} = 1$. Solid line in Figure 5.2 is the best fit result for the total lattice contribution while dash-dotted and dashed lines are the corresponding Debye and Einstein contributions, respectively.

Figure 5.2(b) shows the resulting C_{mag} in zero field (circle, left axis) obtained by subtracting the lattice contribution from the measured C_p . Solid line in Figure 5.2(b) plots the $S_{\text{mag}}(T)$ obtained by integrating C_{mag}/T over temperature (right axis). The $S_{\text{mag}}(T)$ is found to reach and stay at $R \ln 2$ at high temperatures, indicating two-level degrees of freedom.

5.4 Susceptibility and magnetization

Magnetic susceptibility and magnetization were measured using a QuantumDesign SQUID in the 2 – 300 K range in a field up to 5 T. Figure 5.3(a) shows the magnetic susceptibility $\chi = M/H$, where M is magnetization, in a field of $H = 0.1$ T applied parallel and perpendicular

5.4. Susceptibility and magnetization

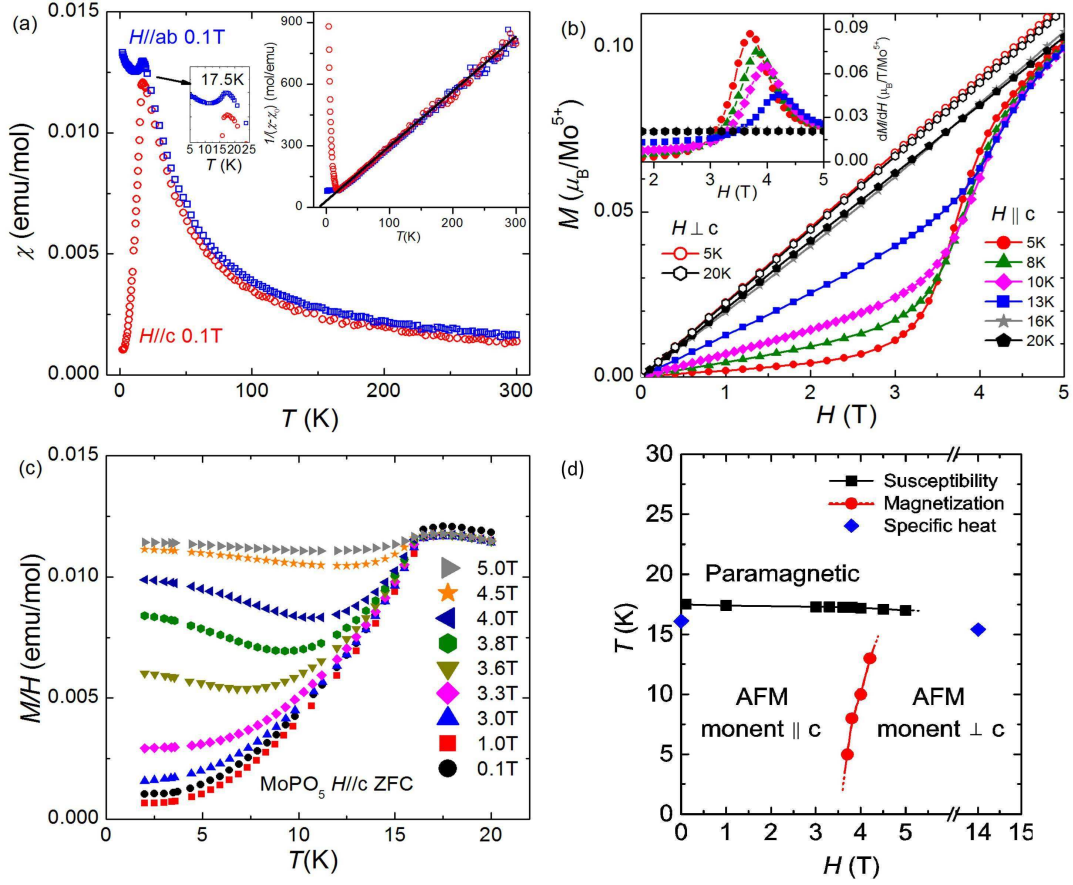


Figure 5.3: (a) Magnetic susceptibility $\chi(T)$ in a field $H = 0.1$ T applied in parallel (circle) and perpendicular (square) to the c axis. Inset shows the inverse susceptibility $1/(\chi - \chi_0)$ against temperature where solid line is a fit to the Curie-Weiss formula. (b) Isothermal magnetization $M(H)$ for $H \parallel c$ (filled symbol) and $H \perp c$ (open symbol) at various temperatures. Inset plots the field derivative dM/dH for $H \parallel c$. (c) M/H as a function of temperature in different magnetic fields applied along c axis. (d) Magnetic phase diagram from the susceptibility (square), specific heat (diamond), and magnetization (circle) data. Lines are guides to the eye.

to the c axis. The $\chi(T)$ for both cases show almost identical behavior from 300 K down to 20 K. However, the $\chi(T)$ for $H \parallel c$ exhibits a sharp drop toward zero as temperature is decreased across 17 K, while the one for $H \perp c$ remains only weakly temperature dependent. This is indicative of antiferromagnetic transition where the ordered moments at low temperatures are collinear to each other, and parallel to the c axis.

The nearly isotropic, high-temperature part of $\chi(T)$ could be well fit by the Curie-Weiss formula,

$$\chi(T) = C/(T - \theta_{\text{CW}}) + \chi_0, \quad (5.4)$$

where θ_{CW} is the Curie-Weiss temperature and χ_0 a temperature-independent diamagnetic and background term. The best fit, as shown in the inset of Figure 5.3(a), yields the effective moment $\mu_{\text{eff}} = 1.71(1)\mu_{\text{B}}$ per Mo^{5+} ion, $\theta_{\text{CW}} = -8.3(3)$ K, and $\chi_0 = 1.5 \times 10^{-4}$ emu/mol for $H \parallel c$, and $\mu_{\text{eff}} = 1.75(1)\mu_{\text{B}}$, $\theta_{\text{CW}} = -8.0(5)$ K, and $\chi_0 = 3.6 \times 10^{-4}$ emu/mol for $H \perp c$. The negative θ_{CW} indicates that antiferromagnetic interactions are dominant.

The isothermal magnetization $M(H)$ for $H \parallel c$ and $H \perp c$ at several temperatures are shown in Figure 5.3(b). At 5 K, the $M(H)$ increases only slowly with the field $H \parallel c$ up to 3 T, but then sharply increases in a narrow field range of 3 – 4 T until it eventually converges to the high temperature $M(H)$ data obtained at 16 K or 20 K. This stepwise increase of $M(H)$ becomes smeared out as temperature is increased. On the other hand, no such stepwise behavior was observed at any temperatures for $H \perp c$. These are typical for systems with spin-flop transition which occurs when the field is applied along an easy axis along which the ordered moments align.

The magnetic susceptibility parallel to the c -axis of MoPO_5 , measured in different magnetic fields, is shown in Figure 5.3(c). A further increase in the susceptibility was noted below 12 K, which is ascribed to the spin-flop transition under a strong magnetic field. Below the critical magnetic field $H_c 3.3$ T, the susceptibility data show no anomalies. For $H = 3.6$ T, a cusplike minimum around is observed around 7 K and shifts to 13 K under $H = 5$ T. The minima T_{min} are due to the spin-flop transitions, because these occur only for H applied (nearly) parallel / anti-parallel to the direction of the magnetic moments (μ) of an antiferromagnet with low anisotropy and not for $H \perp \mu$.

We summarize the results from the thermodynamic and bulk magnetic measurements by drawing the magnetic phase diagram in Figure 5.3(d): square and triangle respectively correspond to the peaks in $\chi(T)$ and $C_p(T)$ for the antiferromagnetic transition while circle corresponds to the peak position in the dM/dH (see inset of Figure 5.3(b)) representing the spin-flop transition for $H \parallel c$.

5.5 Electron spin resonance

B. Nafradi et al. performed the Electron spin resonance (ESR) measurements using a Bruker X-band spectrometer with a TE102 resonant cavity around 9.4 GHz in the 4 to 300 K range.

In order to gain a microscopic insight into the magnetic properties, we have performed ESR measurements as a function of field orientation and temperature. Figure 5.4 plots the obtained room-temperature g factor as the field direction is rotated by ϕ in ab and ac planes. The g factor in ac plane shows a ϕ -variation as large as 2 % with characteristic $\cos^2 \phi$ angular dependence. On the other hand, the g factor in ab plane remains constant within less than

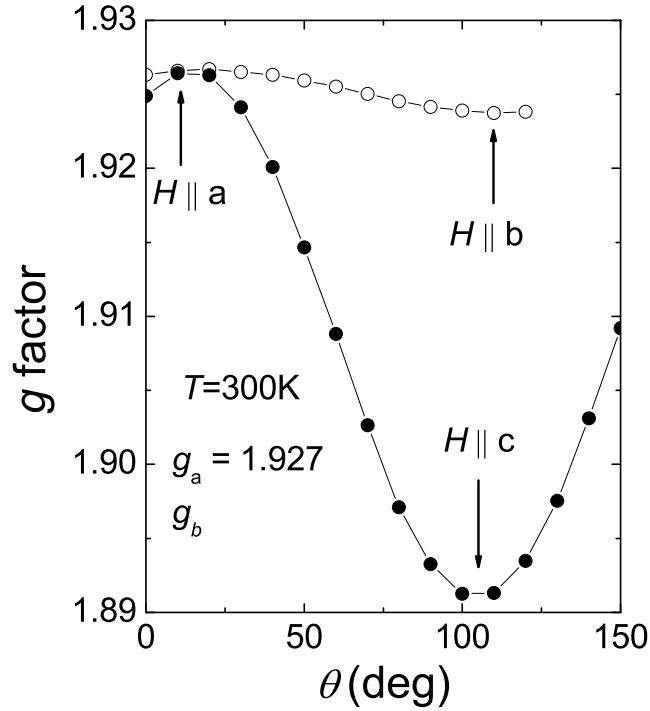


Figure 5.4: Angular dependence of the g factor at room temperature, where filled symbols are for the field varied on the ac plane while open symbols on the ab plane.

0.08 %, as expected from the tetragonal symmetry. We obtain the g factor along the principal axes as $g_a = 1.9255(15)$ and $g_c = 1.889$, of which the average value $g = (2g_a + g_c)/3 = 1.913$ agrees with the one previously obtained by the powder ESR.

Figure 5.5(a) shows the temperature dependence of the resonance field B_0 (circle) and line width ΔH_0 (square) of the spectrum. No field-orientation dependence was observed (not shown). B_0 slowly decreases as temperature is lowered from 300 K down to 24 K, which may be attributed to lattice contraction. As temperature is further lowered below 24 K, B_0 starts to increase sharply reflecting critical fluctuations close to the transition. Similarly, ΔH_0 slowly decreases as temperature is lowered. The spectral line starts to broaden significantly as temperature is lowered from 25 K down to 15 K, also by critical fluctuations. Inset of Figure 5.5(a) plots local spin susceptibility as a function of temperature, obtained by integrating the spectral line normalized by the spectral area at 300 K, $\chi_s(T)/\chi_s(300\text{ K})$. The data could be fit to the Curie-Weiss formula with $\theta_{CW} = -8.9$ K, which agrees with the bulk susceptibility result shown in Figure 5.4.

Temperature evolution of the ESR line across the transition is shown Figure 5.5(b). The line sustains a perfect Lorentzian shape down to 16 K. On the other hand, the line below 16 K close to the transition fits better to a sum of two Lorentzian: one corresponds to the intrinsic

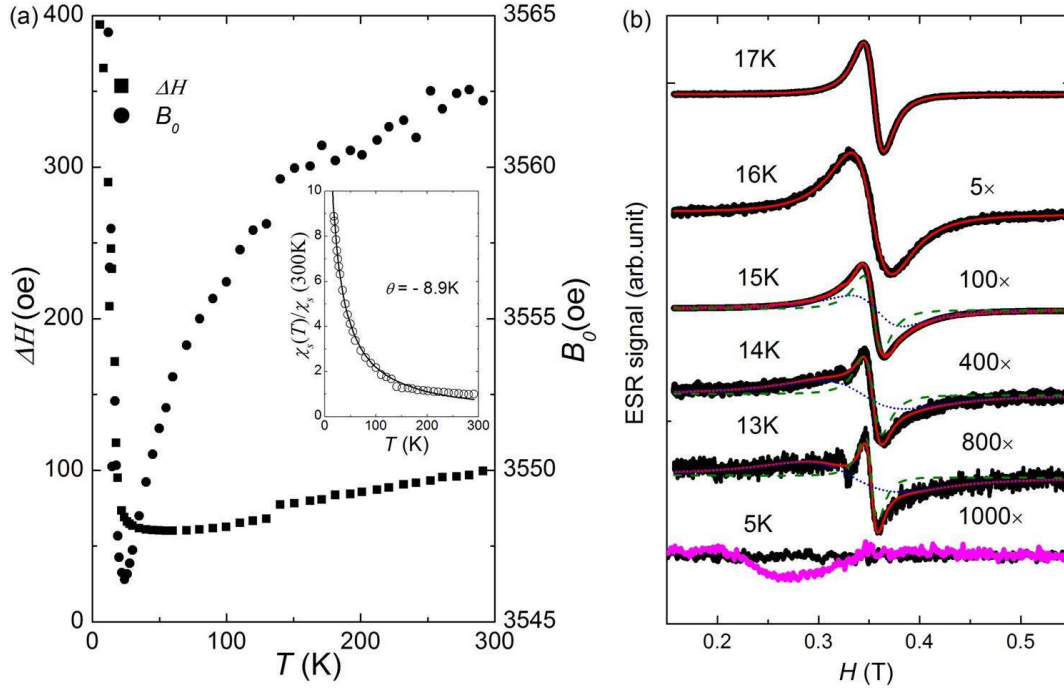


Figure 5.5: (a) Resonance field shift B_0 (circle, right axis) and line width (square, left axis) of the spectrum as a function of temperature. Inset plots normalized spin susceptibility $\chi(T)/\chi(300\text{K})$ as a function of temperature. (b) Temperature evolution of the spectrum for $H \parallel c$ across the transition (black filled circles). Solid line is a sum of two contributions from intrinsic (dotted line) and defect (dashed line) susceptibility. At 5 K, the data for $H \perp c$ (pink filled circles) are overlaid.

sample susceptibility while the other may correspond to some defects. Indeed, the ESR signal at the paramagnetic position below 15 K corresponds to the paramagnetic impurities about 0.1 % concentration. The response below 15 K becomes dominated by the possible defect contribution while a small part may still come from the intrinsic susceptibility. This small intrinsic response below the transition temperature may represent MoPO_5 clusters of which spins remain fluctuating within the ESR time window, which disappears at lower temperatures below 14 K. At 5 K, a broad hump of weak signal was observed around 0.27 T for $H \parallel c$, which was absent for $H \perp c$. This signal may correspond to an antiferromagnetic resonance.

5.6 Neutron diffraction

To determine the microscopic magnetic structure, we have performed neutron diffraction measurements on a single-crystal of MoPO_5 shown in Figure 5.6. Substantial increase of scattering from commensurate long-range magnetic order appears at the (100) position at 5 K, as shown in the rotation scan in Figure 5.6(a). No appreciable change in scattering is

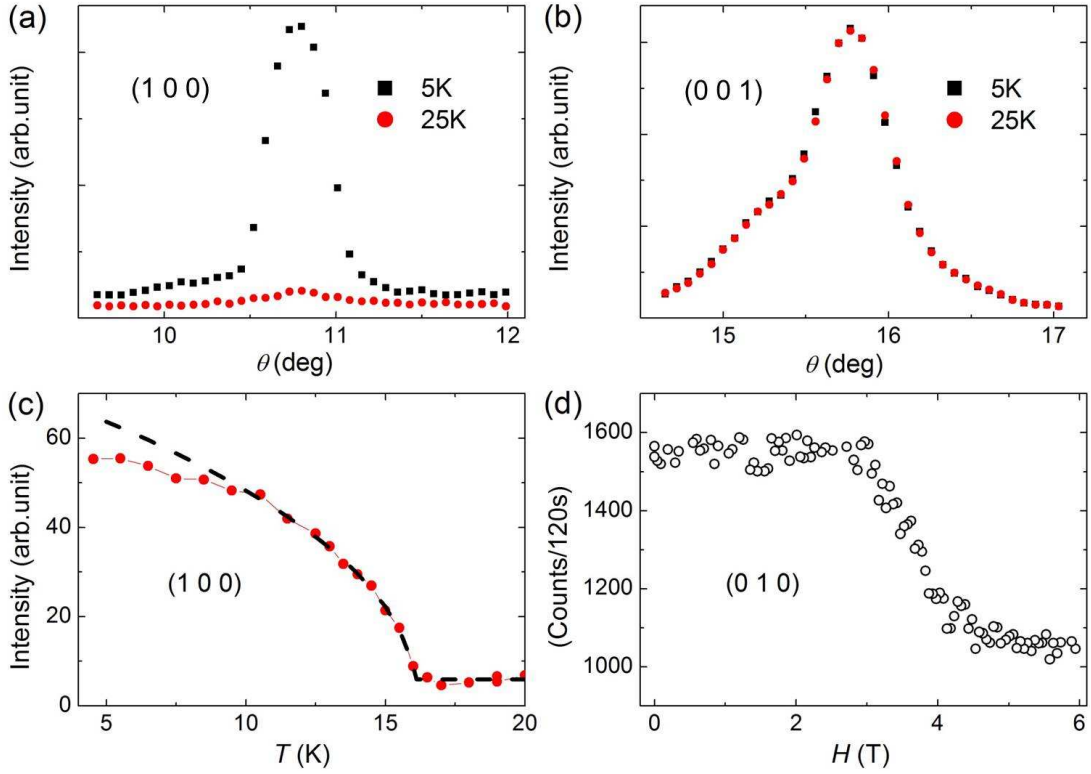


Figure 5.6: Neutron diffraction measurements of rotation scans through (a): (100) and (b): (001) reflections recorded at 5 and 25 K. (c) Temperature evolution of the Bragg peak intensity. The solid line is a power-law fit $I(T) \propto (T_N - T)^{2\beta}$ with the parameters $\beta = 0.23$ and $T_N = 16.17 \pm 0.06$ K. (d) (010) peak intensity as a function of magnetic field.

found close to (001) between 5 and 25 K. A small shoulder of the (001) reflection is likely to originate from a closely orientated secondary grain. Due to the irregular shape of the crystal that results in inconsistent reflection intensities, we cannot refine the magnetic moment from our measurements. Nevertheless, we can elucidate that the magnetic moments of Mo are aligned along the c axis. In addition, magnetization measurements clearly indicate that MoPO_5 is antiferromagnetic. Hence, we conclude that the two equivalent Mo ions in the crystallographic unit cell are aligned anti-parallel. To verify that this is consistent with the symmetry of the lattice and rule out any other magnetic structures, P. Babkevich et. al utilize BasiReps and outline the results here [113].

The magnetic representation is decomposed into six one-dimensional irreducible representations Γ_ν whose resulting basis functions are shown in Table 5.1. Examining the results of the irreducible magnetic representations, we find that only Γ_2 is consistent with our observations. These results are in contrast to the closely related $\text{AMoO}(\text{PO}_4)\text{Cl}$ ($A = \text{K}$ and Rb) materials [114]. Unlike the distorted arrangement of MoO_6 octahedra and PO_4 tetrahedra in MoOPO_4 , $\text{AMoO}(\text{PO}_4)\text{Cl}$ possesses a higher symmetry where the octahedra and tetrahedra are uniformly

| ν | | Mo_1 | Mo_2 |
|-------|----|--------------------|---------------------|
| 1 | Re | (0, 0, 1) | (0, 0, 1) |
| 2 | Re | (0, 0, 1) | (0, 0, $\bar{1}$) |
| 3 | Re | (1, 0, 0) | (1, 0, 0) |
| 3 | Im | (0, $\bar{1}$, 0) | (0, $\bar{1}$, 0) |
| 4 | Re | (1, 0, 0) | ($\bar{1}$, 0, 0) |
| 4 | Im | (0, $\bar{1}$, 0) | (0, 1, 0) |
| 5 | Re | (1, 0, 0) | (1, 0, 0) |
| 5 | Im | (0, 1, 0) | (0, 1, 0) |
| 6 | Re | (1, 0, 0) | ($\bar{1}$, 0, 0) |
| 6 | Im | (0, 1, 0) | (0, $\bar{1}$, 0) |

Table 5.1: Basis functions of irreducible representation Γ_ν separated into real and imaginary components and resolved along the crystallographic axes. The two equivalent Mo ions are related by an inversion through the origin.

arranged in the ab plane. Powder neutron diffraction measurements on $\text{AMoO}(\text{PO}_4)\text{Cl}$ reveal an antiferromagnetic structure where Mo moments are instead confined to the ab plane [115].

Figure 5.6(c) shows the temperature dependence of the (100) Bragg peak, which can be fitted by a power-law below T_N . The dashed line in Figure 5.6(c) is a fit of the data from 5–16 K, to a power-law,

$$I(T) \propto (T_N - T)^{2\beta}. \quad (5.5)$$

β is the exponent from the temperature dependence of the atomic displacement δ since $I(T) \propto (\delta)^2$. The fit demonstrates that $\beta = 0.23$. We also find $T_N = 16.17 \pm 0.06$ K – consistent with the magnetization and specific heat measurements. In Figure 5.6(d) we show the magnetic Bragg peak intensity as a function of applied field along the c axis recorded at 2 K. Above 3 T, we find a sharp decrease in intensity which then appears to saturate above 5 T. The change the the Bragg peak intensity is consistent with a spin-flop transition that is observed in the magnetization measurements shown in Figure 5.3(b). This corresponds to a tilt of the moments by approximately 35° away from the c axis.

5.7 Conclusion

In summary we have established that the $4d^1$ compound MoPO_5 is orbitally quenched and orders into an antiferromagnet with the moments along c axis. Spin-flop transition is observed which indicates magnetic anisotropy. Yet the g factor is only slightly anisotropic and somewhat less than the spin-only value. Magnetic susceptibility and ESR support only a minute mixing of orbital moment, and more definitely, specific heat data suggests effectively a spin-1/2

degree of freedom. Experimentally, the magnetic ground state supports a Néel type collinear order along the stacking axis. Our results suggest that molybdates may provide an alternative playground to search for model quantum magnets other than $3d$ compounds.

6 Kagome-like planar compound

Cu_2OSO_4

6.1 Motivation for This Work

Low dimensional geometrically frustrated systems, based on triangles of interacting spins with antiferromagnetic (AFM) interaction, for example the chain antiferromagnetic compounds [116, 117] and the kagome lattice compounds [28, 29, 30], are at the forefront of condensed matter research. Among them, kagome lattice represents an especially interesting example because of the stronger geometrical frustration. Recent experimental and theoretical advances have shown that a long sought-after spin-liquid state might have been realized in materials like herbertsmithite $\text{ZnCu}_3(\text{OH})_6\text{Cl}_2$ [28] and vorborthite $\text{Cu}_3\text{V}_2\text{O}_7(\text{OH})_2 \cdot 2\text{H}_2\text{O}$ [118, 29].

The actual realization of a kagome lattice is difficult to achieve in real materials. The presence of magnetic interactions that go beyond nearest neighbour, non-negligible out-of-plane coupling or a significant antisymmetric Dzyaloshinskii-Moriya (DM) interaction lift the degeneracy of an ideal spin-liquid and drive the system into a long-range magnetic order. Thus, investigation of various realizations of kagome-like lattices is crucial to understand how a particular set of microscopic parameters leads to the observed ground state.

Here we investigated a novel compound, Cu_2OSO_4 , which resembles some features of the kagome lattice. The magnetic and thermodynamic properties of a Cu_2OSO_4 single crystal have been reported using specific heat, susceptibility and magnetization.

6.2 Synthesis and Crystal Structure

High-quality single crystals of Cu_2OSO_4 were grown in two steps by H. Berger. Firstly, Dolerophanite Cu_2OSO_4 powder has been successfully synthesized by using CuSO_4 anhydrous 98% Alfa Aesar powder as source.

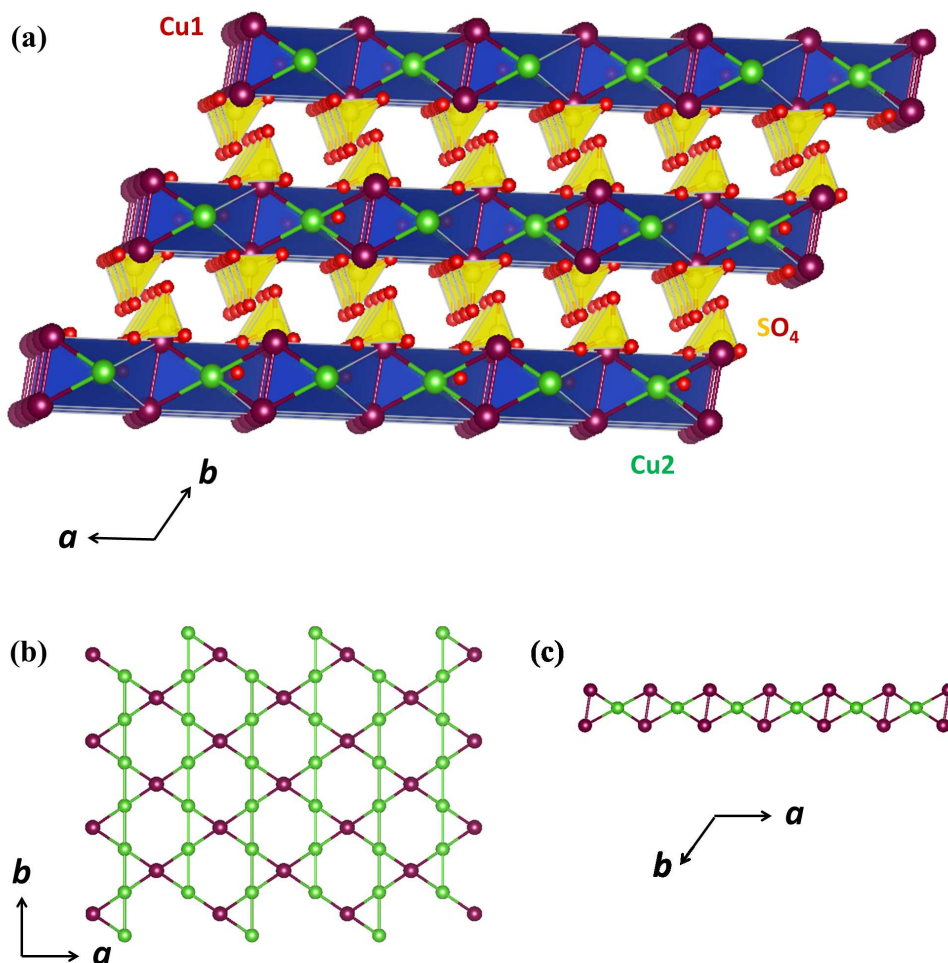


Figure 6.1: (a) crystal structure of Cu_2OSO_4 ; (b) a single layer of copper ions forming a kagome-like structure where only Cu^{2+} ions are shown for simplicity in the ab plane; (c) perpendicular view of the copper layer, showing two Cu2 sites between Cu1 chains.



A quartz crucible is then filled with 60 grams of standard commercially available CuSO_4 anhydrous powder (98% Aesar) without further purification and placed in the center of a muffle furnace and heated at 740°C in air atmosphere for 20 min, the milling and firing procedures was repeated 3 times. After each firing procedure, the black surface layer of CuO was removed completely by mechanical finishing. Synthetic orange-brown powder of Cu_2OSO_4 as final stable product were obtained. The fine particulate powder was then used

in the described experiments and analyses. Secondly, single crystals of Cu_2OSO_4 were grown with three different transport agents: Cl_2 , Br_2 and NiBr_2 . A portion (about 10–30 grams) of the stoichiometric powder was placed in a quartz ampoule ($l = 250$ mm, $d = 40$ mm) and evacuated to 10^{-6} Torr. In the next step, the transport agent of Cl_2 , Br_2 and NiBr_2 was introduced at room temperature into the ampoule. The ampoules were put into a two zone gradient furnace. The best charge and growth-zone temperatures were 650°C and 550°C , respectively. After 5 weeks, the dark brown colored semitransparent crystals were obtained. Large-sized crystals had a typical dimension of $4 \times 4 \times 1$ mm³ and large mass of 0.1 g, as shown in Figure 6.2. For the Cu_2OSO_4 good results are found using Cl_2 and NiBr_2 . The shape of the crystal is irregular, but, at least one smooth surface, corresponding to the layers of ab -plane could be found.

Single-crystal x-ray diffraction data was collected at room temperature. The crystal belongs to a space group of $C12/m1$ with the lattice parameters of $a = 9.3818$ Å, $b = 6.3393$ Å, $c = 7.6545$ Å and $\beta = 122.206^\circ$ and in agreement with Ref. [119]. It consists of layers of interconnected copper ions ($S=1/2$), separated by layers of SO_4 tetrahedra (Figure 6.1(a)). Copper ions form a distorted kagome lattice (Figure 6.1(b)) in ab -plane with two nonequivalent copper environments. Additional feature is the presence of two Cu2 ions (red) that bridge chains of Cu1 ions (green) (Figure 6.1(c)).

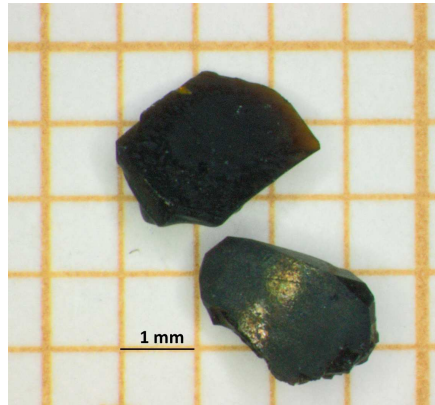


Figure 6.2: Photograph of a representative single crystal of Cu_2OSO_4 .

6.3 Susceptibility and magnetization

Magnetization were measured using a QuantumDesign SQUID in the 2 – 300 K range in a field up to 5 T. The low temperature $\chi(T)$ perpendicular to the ab plane of Cu_2OSO_4 , measured in different magnetic fields, is shown in Figure 6.3. An increase was noted below 20 K, which is ascribed to a magnetic transition T_c . Most notably, a splitting for ZFC and FC is observed below $T_c=20.5$ K under low field $H < 0.1$ T, indicating a canted-AFM ground state with a weak ferromagnetic component. The bifurcation point shifts to lower temperature with the field

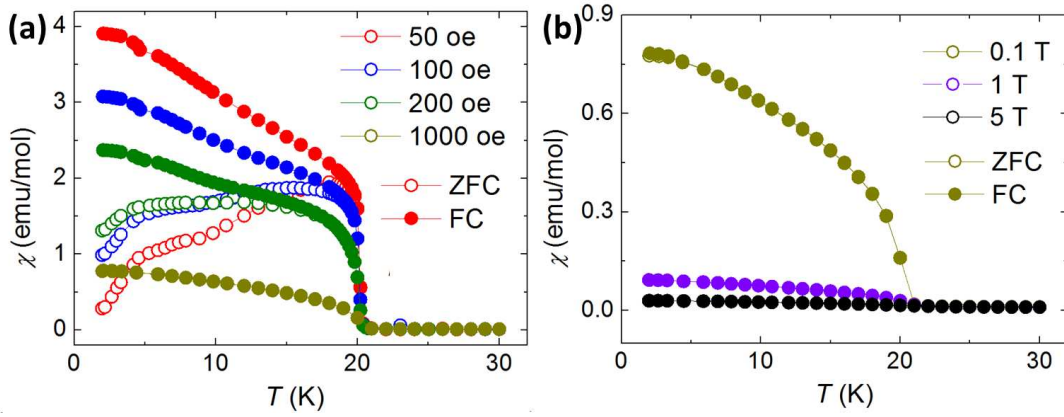


Figure 6.3: Susceptibility as a function of temperature in different magnetic fields applied perpendicular to the ab plane of the crystal. (a) Under low field $H \leq 0.1$ T; (b) under high field $0.1 \text{ T} \leq H \leq 5$ T.

increasing, e.g., the ZFC and FC data split at 20 K in 50 Oe and at 17 K in 200 Oe. The splitting disappears in stronger fields, i.e., $H \geq 0.1$ T. The ZFC and FC data completely overlay at all temperatures down to 2 K.

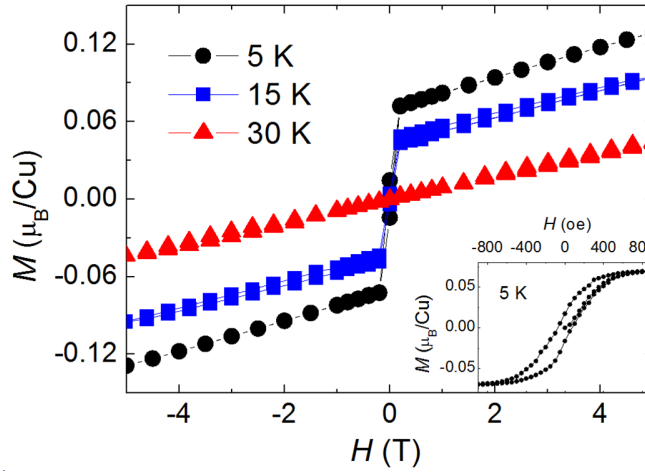


Figure 6.4: Isothermal magnetization as a function of magnetic field applied perpendicular to the ab plane of the crystal for different temperatures. Inset: magnetization loop measurement at 5 K where a zoom-in is shown.

The isothermal magnetization $M(H)$ for $H \perp ab$ at several temperatures are shown in Figure 6.4. Above the transition temperature $T_c = 20.5$ K the $M(H)$ curve is linear. A hysteresis loop is clearly visible at 5 K, as shown in the inset of Fig. 6.4(b). The $M(H)$ curve becomes linear with H above 0.1 T in the measured temperature range. This behavior is consistent with the low temperature susceptibility results which show no splitting between ZFC and FC under $H \geq 0.1$ T. These are typical for the canted-AFM ground state with a weak ferromagnetic

component.

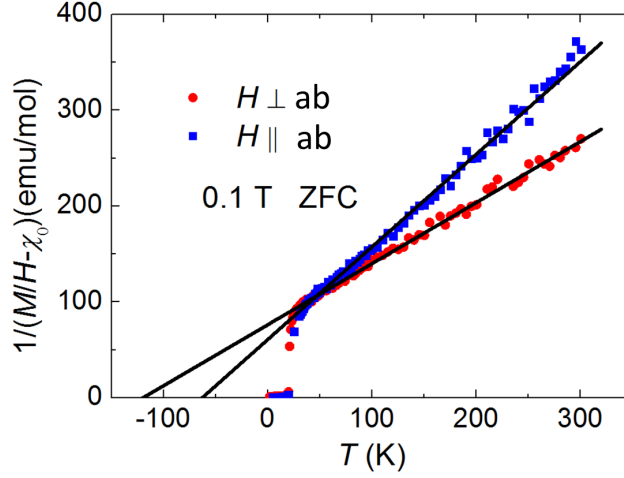


Figure 6.5: Inverse magnetic susceptibility $1/(M/H - \chi_0)$ versus temperature in $H = 0.1$ T for $H \parallel ab$ and $H \perp ab$.

The high-temperature part of $\chi(T)$ could be well fit by the Curie-Weiss formula,

$$\chi(T) = C/(T - \theta_{CW}) + \chi_0, \quad (6.1)$$

where C is the Curie constant, θ_{CW} is the Curie-Weiss temperature and χ_0 a temperature-independent diamagnetic and background term. The best fit, as shown in Figure 6.5, yields $C = 1.04(5)$ emu/molK, the effective moment $\mu_{\text{eff}} = 2.04(5)\mu_B$ per Cu^{2+} ion, $\theta_{CW} = -63(4)$ K, and $\chi_0 = 4.6 \times 10^{-4}$ emu/mol for $H \parallel ab$ plane, and $C = 1.57(10)$ emu/molK, $\mu_{\text{eff}} = 2.51(9)\mu_B$, $\theta_{CW} = -120(7)$ K, and $\chi_0 = 4.0 \times 10^{-5}$ emu/mol for $H \perp ab$. The negative θ_{CW} indicates that antiferromagnetic interactions are dominant. The anisotropic C and θ_{CW} indicate the existence of anisotropic exchange interactions of this compound. θ_{CW} for both direction are much larger than T_c , indicating a significant geometrical frustration.

The anisotropic exchange interactions of Cu_2OSO_4 are also revealed by Fig. 6.6. Quantitatively similar behavior is seen from the low temperature susceptibility in $H = 50$ oe and the magnetic isotherm at 5 K with the field applied for $H \parallel ab$ and $H \perp ab$, respectively. However, the magnetic moment for $H \parallel ab$ plane is around 3 times larger than that for $H \perp ab$.

Figure 6.7(a) presents the magnetization of Cu_2OSO_4 vs. temperature in 50 Oe and 1 T magnetic fields measured in the field cooled cooling (FCC), and field cooled warming (FCW) processes. In the FCC process, the measurement is performed during the cooling process. After reaching 5 K, the measurement is continued during warming up process under the same H . This last process is the so called FCW. In Figure 6.7(a), the $M_{FCC}(T)$ and $M_{FCW}(T)$ curves overlap above T_c . Below T_c , a small thermal hysteresis is observed and suppressed

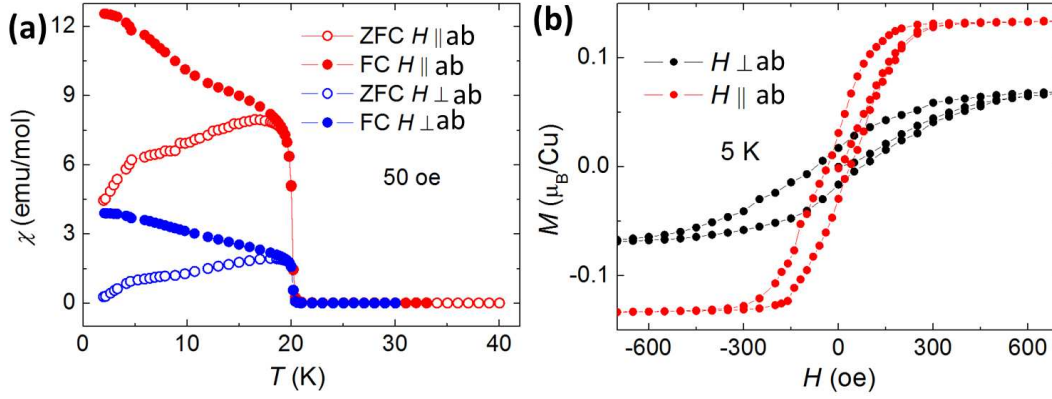


Figure 6.6: (a) Magnetic susceptibility versus temperature in $H = 50$ oe for $H \parallel ab$ and $H \perp ab$. (b) Magnetic isotherm at 5 K with the field applied for $H \parallel ab$ and $H \perp ab$.

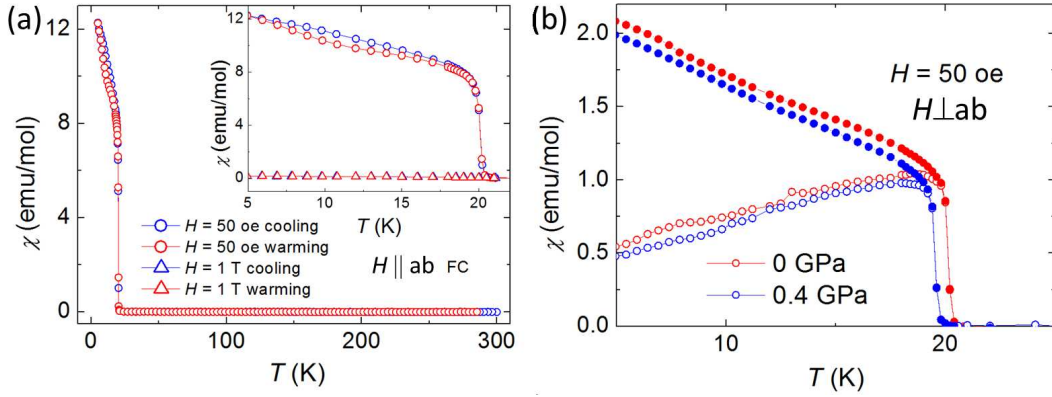


Figure 6.7: (a) Magnetic susceptibility versus temperature in the FCC and FCW protocols. Thermal hysteresis observed in the susceptibility of Cu_2OSO_4 indicating the first order transition in $H = 50$ oe for $H \parallel ab$. (b) Magnetic isotherm at 5 K with the field applied for $H \parallel ab$ and $H \perp ab$.

by high magnetic field, indicating the weak first order transition. Figure 6.7(b) shows the magnetic susceptibility curves for $H \perp ab$ under different pressures. Under ambient pressure a pronounced peak is found at 20.5 K, while the peak appears at a slightly lower temperature of 19.5 K under 0.4 GPa.

6.4 Specific heat

Specific heat was measured by M. Kriener using a QuantumDesign PPMS in the temperature range of 2 – 250 K in zero field 1 T, 5 T and 14 T for $H \perp ab$. Figure 6.8(a) presents the specific heat C_p from 250 K down to 2 K in zero field. C_p decreases monotonically with lowering temperature down to 20 K. Corresponding to the magnetic phase transition, C_p exhibits a

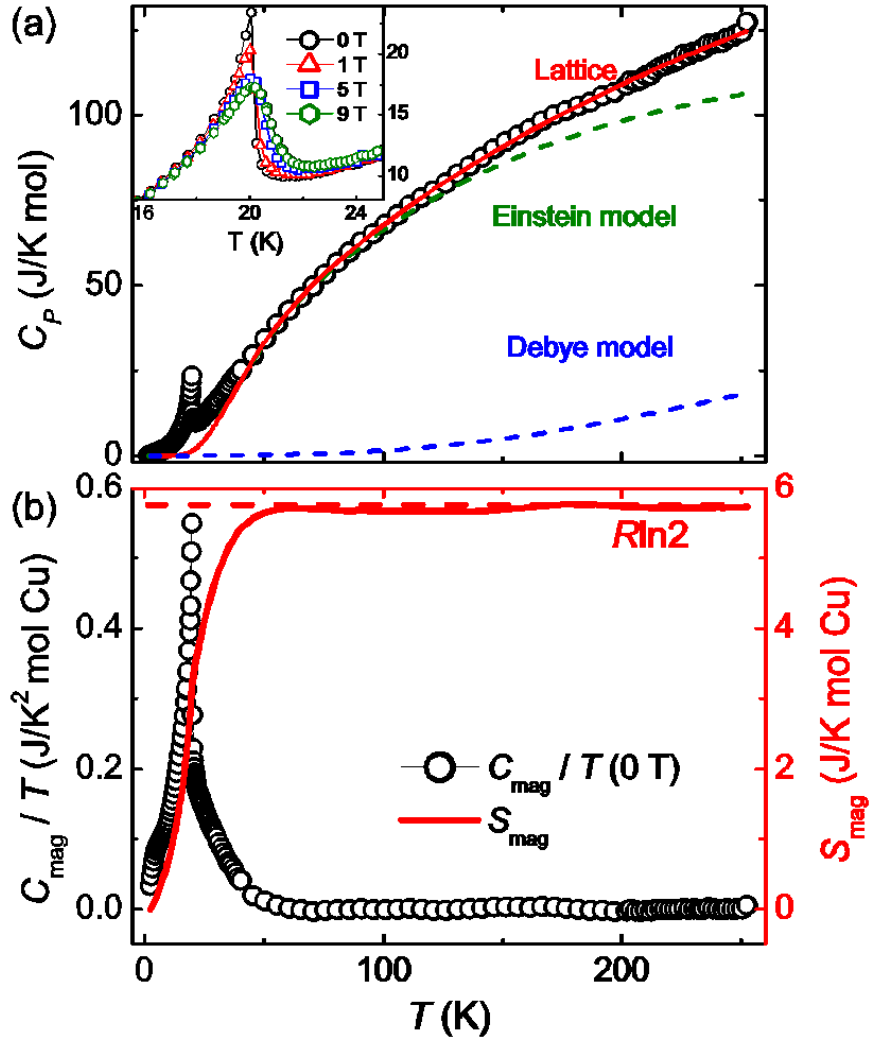


Figure 6.8: (a) Specific heat C_p as a function of temperature in zero field (black circle). Red solid line represents the best fit of the simulated lattice contribution using the Debye (blue dashed line) and Einstein (green dashed line) terms. Inset provides an enlarged view of the low temperature region in zero field, 1 T, 5 T and in 14 T. (b) Left axis: magnetic part of the specific heat, C_{mag} , divided by temperature (black circle). Right axis: solid line is the entropy calculated from the C_{mag} .

sharp lambda-shape peak near the transition temperature T_c , which is slightly increased and broadened with the increase in the magnetic field, as shown in the inset of Figure 6.8(a). These peaks correspond to a transition into a long range ordered phase.

In order to extract the magnetic part of the specific heat, C_{mag} , and deduce the corresponding entropy S_{mag} , we simulate the lattice contribution using high temperature data by taking into account the Debye and Einstein contributions. We fit the C_p data above 100 K by a lattice-only

model

$$C_p = C_D + \sum_i C_{E,i}, \quad (6.2)$$

where C_D and $C_{E,i}$ represent the Debye and Einstein terms, respectively. The Debye term is expressed as

$$C_D = 9n_D R \left(\frac{T}{\Theta_D} \right)^3 \int_0^{\Theta_D/T} \frac{x^4 e^x}{(e^x - 1)^2} dx, \quad (6.3)$$

and the Einstein term as

$$C_E = 3n_E R \frac{y^2 e^y}{(e^y - 1)^2}, \quad y \equiv \Theta_E/T, \quad (6.4)$$

where Θ_D and Θ_E are the Debye and Einstein temperatures, respectively, and the sum $n_D + n_E$ is the total number of atoms per formula unit. The best fit, using one Debye and two Einstein terms, yields the characteristic temperatures $\Theta_D = 1577$ K, $\Theta_{E,1} = 548$ K, and $\theta_{E,2} = 165$ K, and the numbers $n_D = 3$, $n_{E,1} = 2$, $n_{E,2} = 3$. Solid line in Figure 6.8 is the best fit result for the total lattice contribution while blue-dashed and green-dashed lines are the corresponding Debye and Einstein contributions, respectively.

Figure 6.8(b) shows the resulting C_{mag} in zero field (circle, left axis) obtained by subtracting the lattice contribution from the measured C_p . Solid line in Figure 6.8(b) plots the $S_{\text{mag}}(T)$ obtained by integrating C_{mag}/T over temperature (right axis). Above T_c magnetic correlations exist up to 50 K. The $S_{\text{mag}}(T)$ is found to reach and stay at $R \ln 2$ at high temperatures which is consistent with $S=1/2$ magnetic moments, indicating two-level degrees of freedom.

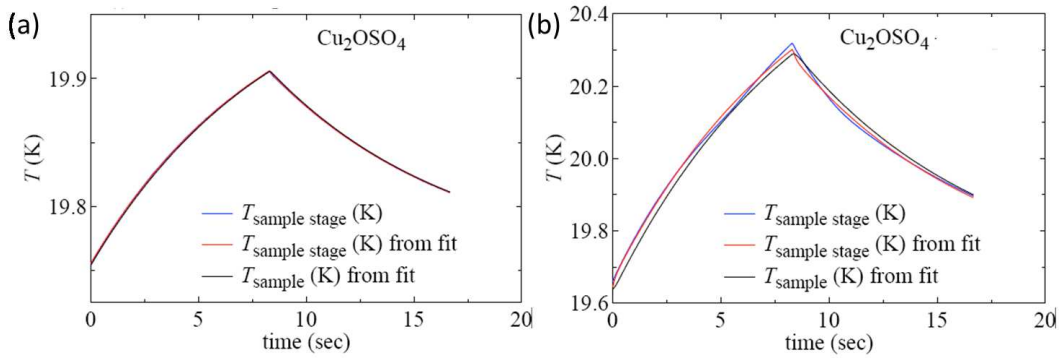


Figure 6.9: The temperature versus time relaxation at $T \sim 20$ K. (a) Time scan below T_c ; (b) time scan across T_c .

The λ -like shape transition indicates the second order phase transition. Simulating by the difference between FCC and FCW data indicating the weak first order phase transition nature,

the temperature-time relaxation curves are presented in Figure 6.9. For the time scan below T_c , the temperature arrest was not observed in both of warming and cooling part. For the time scan across T_c , a temperature arrest around 20.1 K (warming process) was observed, indicating the weak first-order phase transition nature.

6.5 Conclusion

We synthesized the single crystals of Kagome-like compound Cu_2OSO_4 and systematically reported the magnetic and specific heat behaviors. The lattice geometry is potentially interesting from a theoretical point of view and the stronger geometrical frustration is expected.

The existence of a magnetic phase transition around 20 K indicates an ordered ground state. However, the transition temperature is much lower than curie temperatures ($\theta_{\text{CW}} = -63(4)$ K for $H \parallel ab$ plane and $\theta_{\text{CW}} = -120(7)$ K for $H \perp ab$) indicating low dimensionality and/or frustration. Magnetic measurements show typical signatures for a canted-AFM ground state with a weak ferromagnetic component. Canted moments and the different curie temperatures for different orientations indicate significant anisotropy.

Specific heat shows the corresponding anomaly at 20 K in zero field, but at slightly increased temperature 20.5 K in a magnetic field as high as $H = 14$ T. Analysis of specific heat is compatible with all of Rln2 being released at the transition. The time scans across the transition temperature shows very weak first order, which is consistent with the hysteresis loop upon field cooled warming and cooling of susceptibility.

6.6 Future work

Results obtained so far indicate that Cu_2OSO_4 deserves a closer attention. Future measurements could be performed, as following:

- 1, Determine the magnetic structure below the transition with neutron diffraction.
- 2, Check whether there is a structural distortion which would explain the first order nature with synchrotron X-ray diffraction.
- 3, Determine the magnetic excitations which would allow to detect the magnetic interactions and exchange energies in the system with inelastic neutron spectroscopy.

We already applied the beam time for D20, which is ideally suited for this study due to the high-flux/high-resolution and small magnetic moment considerations.

7 Conclusions

The work presented in this thesis focused on the synthesis and characterization of the physical Properties of $3d$, $4d$ and $5d$ transition metal compounds.

In particular I studied the $5d$ Ir-based compounds. Two novel iridates $\text{Ba}_8\text{Al}_2\text{IrO}_{14}$ and $\text{Ba}_8\text{Al}_2\text{IrO}_{14}$ were synthesized and characterized for the first time. $\text{Ba}_8\text{Al}_2\text{IrO}_{14}$ has been prepared as single crystals which provides a rare example of a full-Ir(VI) compound that can be grown under ambient pressure. Our experiment shows $\text{Ba}_8\text{Al}_2\text{IrO}_{14}$ has monoclinic crystal structure with the space group of $C2/m(12)$. It is a p -type band insulator with a narrow band gap of approximately 0.6 eV, and these are confirmed by the optical measurements. Furthermore, $\text{Ba}_8\text{Al}_2\text{IrO}_{14}$ shows antiferromagnetic couplings but display no order down to 2 K. $\text{Ba}_{21}\text{Ir}_9\text{O}_{43}$ was also synthesized as single crystals using self-flux method. It contains two different Ir layers of triangular lattice. One layer consists of Ir_2O_9 dimers while the other is made of two regular Ir-O octahedra and one triangular pyramid. The triangular pyramids with presumably Ir^{4+} is suggested to carry substantial magnetic moments as large as $\sim 6\mu_B/\text{Ir}$, while the dimers and octahedra with Ir^{5+} may hold only small moments. The compound is an insulator with antiferromagnetic Curie-Weiss behavior, where a magnetic transition is suppressed down to low temperature of 9 K despite the large Curie-Weiss temperature of -90 K. The difference between field-cooled and zero-field cooled susceptibility and ESR data may suggest the presence of magnetic domains. I also performed the pressure-dependent resistivity measurements of $\text{Ir}_{0.95}\text{Pt}_{0.05}\text{Te}_2$. With applying pressure, the high T structural transition appears and the low T superconductivity is depressed. The residual resistivity ρ_0 is pressure-independent below the critical pressure and increases with increasing pressure above P_c . The low temperature superconductivity undergoes a dimensionality cross-over from 3D to 2D. I hope these work will stimulate more studies on Ir-based compounds that offer a wide window into the research of spin-orbit interactions and the strength of electronic correlations.

The magnetic properties and specific heat of $3d$ and $4d$ transition metal oxides were also

investigated. The $4d$ transition-metal oxides naturally bridge two different regimes of the strongly correlated $3d$ compounds and the $5d$ compounds with strong spin-orbit coupling. We found that the $4d^1$ compound MoPO_5 is orbitally quenched and orders into an antiferromagnet with the moments along c axis. Spin-flop transition is observed which indicates magnetic anisotropy. Yet the g factor is only slightly anisotropic and somewhat less than the spin-only value. Magnetic susceptibility and ESR support only a minute mixing of orbital moment, and more definitely, specific heat data suggests effectively a spin-1/2 degree of freedom. For $3d$ transition metal oxides, their low dimensional magnetism draw our attention. We systematically reported the physical properties of the single crystals of Kagome-like compound Cu_2OSO_4 and. Magnetic susceptibility shows typical signatures for a canted-AFM ground state with a weak ferromagnetic component. Specific heat shows the corresponding anomaly at 20 K in zero field, but at slightly increased temperature 20.5 K in a magnetic field as high as $H = 14$ T. I hope these work will stimulate more investigations on these $3d$ and $4d$ transition-metal oxides.

Bibliography

- [1] G. Kotliar and D. Vollhardt. Strongly correlated materials: Insights from dynamical mean-field theory. *Physics Today*, 57(3):53, 2004.
- [2] K. Prsa. Neutron scattering investigations of weakly coupled and weakly connected antiferromagnets. *PhD thesis*, ETH Zurich and Paul Scherrer Institute, 2010.
- [3] S. J. Moon J.-Y. Kim B.-G. Park C. S. Leem Jaejun Yu-T. W. Noh C. Kim S.-J. Oh J.-H. Park V. Durairaj G. Cao E. Rotenberg B. J. Kim, Hosub Jin. Novel $J_{eff} = 1/2$ Mott State Induced by Relativistic Spin-Orbit Coupling in Sr_2IrO_4 . *Phys. Rev. Lett.*, 101:076402, 2008.
- [4] O. Korneta. A systematic study of transport, magnetic, and thermal properties of layered Iridates. *PhD thesis*, University of Kentucky, 2012.
- [5] J. Stohr and H. C. Siegmann. Magnetism: From Fundamentals to Nanoscale Dynamics. *Springer*, 2006.
- [6] S. Blundell. Magnetism in Condensed Matter. *Oxford Master Series in Condensed Matter Physics*, 2001.
- [7] G. Jackeli and G. Khaliullin. Mott Insulators in the Strong Spin-Orbit Coupling Limit: From Heisenberg to a Quantum Compass and Kitaev Models. *Phys. Rev. Lett.*, 102: 017205, 2009.
- [8] L. Pan and G. Zhu. Perovskite Materials - Synthesis, Characterisation, Properties, and Applications. *InTech*, 2016.
- [9] K. W. Kim W. S. Choi Y. S. Lee J. Yu G. Cao A. Sumi H. Funajubo C. Bernhard S. J. Moon, H. Jin and T. W. Noh. Dimensionality-controlled insulator-metal transition and correlated metallic state in 5d transition metal oxides $\text{Sr}_{n+1}\text{Ir}_n\text{O}_{3n+1}$ ($n = 1, 2$, and ∞). *Phys. Rev. Lett.*, 101:226402–4, 2008.
- [10] S. Bhowal S. K. Panda R. Mathieu J. C. Orain F. Bert P. Mendels P. G. Freeman M. Mansson H. M. Ronnow M. Telling-P. K. Biswas D. Sheptyakov S. D. Kaushik Vasudeva Siruguri

Bibliography

- C. Meneghini D. D. Sarma I. Dasgupta A. Nag, S. Middey and S. Ray. Origin of the Spin-Orbital Liquid State in a Nearly $J = 0$ Iridate $\text{Ba}_3\text{ZnIr}_2\text{O}_9$. *Phys. Rev. Lett.*, 116:097205, 2016.
- [11] APEX2 User Manual. *Bruker Advanced X-ray Solutions*, Version 1.22.
- [12] K. Hasegawa. Introduction to single crystal X-ray analysis. *The Rigaku Journal*, 28(1), 2012.
- [13] S. J.B. Reed M. R. Cave P. J. Potts, J. F.W. Bowles. Microprobe Techniques in the Earth Sciences. *The Mineralogical Society of Great Britain and Ireland*, 1995.
- [14] A. LaLonde S. Iwanaga, E. S. Toberer and G. Jeffrey Snyder. A high temperature apparatus for measurement of the Seebeck coefficient. *Rev. Sci. Instrum.*, 82:063905, 2011.
- [15] I. Kezsmarki. Phase Diagram of a Correlated d-electron System: Experimental Study of BaVS_3 . *PhD thesis*, Budapest University, 2003.
- [16] I. R. Walker. Considerations on the selection of alloys for use in pressure cells at low temperatures. *Cryogenics*, 45(2):87, 2005.
- [17] A. Avella and F. Mancini. Strongly Correlated Systems: Experimental Techniques. *Springer*, 180, 2014.
- [18] Quantum Design. Magnetic Property Measurement System MPMS XL. Hardware Reference Manual. *San Diego, CA*, 2000.
- [19] Almax-easylab. Mcell 10, High-pressure Cell.
- [20] Quantum Design. Physical Property Measurement System-Heat Capacity Option User's Manual. *San Diego, USA*, 2004.
- [21] Y. K. Luo. *PhD thesis*, Zhejiang University, 2012.
- [22] D.-H. Kim J.-J. Yang S.-W. Cheong M. J. Eom J. S. Kim R. Gammag K.-S. Kim H.-S. Kim T.-H. Kim H.-W. Yeom T.-Y. Koo H.-D. Kim K.-T. Ko, H.-H. Lee and J.-H. Park. Charge-ordering cascade with spin-orbit Mott dimer states in metallic iridium ditelluride. *Nature Communications*, 6:7342, 2015.
- [23] K.-T. Ko-Hwangho Lee J.-H. Park J.J. Yang S.-W. Cheong Kyoo Kim, Sooran Kim and B.I. Min. Origin of First-Order-Type Electronic and Structural Transitions in IrTe_2 . *Phys. Rev. Lett.*, 114:136401, 2015.
- [24] K. Kudo S. Pyon and M. Nohara. Emergence of superconductivity near the structural phase boundary in Pt-doped IrTe_2 single crystals. *Physica C*, 494:80, 2013.

- [25] K. Byrappa and D. Y. Pushcharovsky. Crystal chemistry and its significance on the growth of technological materials. *Prog. Cryst. Growth Charact. Mater.*, 24:269, 1992.
- [26] C. N. R. Rao and B. Raveau. *Transition Metal Oxides*, 1995.
- [27] A. Fujimori M. Imada and Y. Tokura. Metal-insulator transitions. *Rev. Mod. Phys.*, 70:1039, 1998.
- [28] B. M. Bartlett M. P. Shores, E. A. Nytko and D. G. Nocera. A Structurally Perfect $S = 1/2$ Kagome Antiferromagnet. *J. Am. Chem. Soc.*, 127:13462, 2005.
- [29] N. Kobayashi M. Nohara H. Takagi-Y. Kato Z. Hiroi, M. Hanawa and M. Takigawa. Spin- $1/2$ Kagome-Like Lattice in Volborthite $\text{Cu}_3\text{V}_2\text{O}_7(\text{OH})_2 \cdot 2\text{H}_2\text{O}$. *J. Phys. Soc. Jpn.*, 70:3377, 2001.
- [30] H. Yoshida Y. Okamoto and Z. Hiroi. Vesignieite $\text{BaCu}_3\text{V}_2\text{O}_8(\text{OH})_2$ as a Candidate Spin- $1/2$ Kagome Antiferromagnet. *J. Phys. Soc. Jpn.*, 78:033701, 2009.
- [31] S. Ikeda S. Nakatsuji and Y. Maeno. Ca_2RuO_4 : New Mott Insulators of Layered Ruthenate. *J. Phys. Soc. Jpn.*, 66:1868, 1997.
- [32] M. Shepard J. E. Crow R. P. Guertin G. Cao, S. McCall. Magnetic and transport properties of single-crystal Ca_2RuO_4 : Relationship to superconducting Sr_2RuO_4 . *Phys. Rev. B*, 56:R2916, 1997.
- [33] S. Nakatsuji and Y. Maeno. Quasi-Two-Dimensional Mott Transition System $\text{Ca}_{2-x}\text{Sr}_x\text{RuO}_4$. *Phys. Rev. Lett.*, 84:2666, 2000.
- [34] K. Yoshida S. Nishizaki T. Fujita J. G. Bednorz Y. Maeno, H. Hashimoto and F. Lichtenberg. Superconductivity in a layered perovskite without copper. *Nature*, 372:532, 1994.
- [35] G. Cao, Y. Xin, C. S. Alexander, J. E. Crow, P. Schlottmann, M. K. Crawford, R. L. Harlow, and W. Marshall. Anomalous magnetic and transport behavior in the magnetic insulator $\text{Sr}_3\text{Ir}_2\text{O}_7$. *Phys. Rev. B*, 66:214412, 2002.
- [36] Y. Singh and P. Gegenwart. Antiferromagnetic Mott insulating state in single crystals of the honeycomb lattice material Na_2IrO_3 . *Phys. Rev. B*, 82:064412, 2010.
- [37] A. S. Erickson, S. Misra, G. J. Miller, R. R. Gupta, Z. Schlesinger, W. A. Harrison, J. M. Kim, and I. R. Fisher. Ferromagnetism in the Mott Insulator $\text{Ba}_2\text{NaOsO}_6$. *Phys. Rev. Lett.*, 99:016404, 2007.
- [38] B. J. Yang and Y. B. Kim. Topological insulators and metal-insulator transition in the pyrochlore iridates. *Phys. Rev. B*, 82:085111, 2010.

Bibliography

- [39] D. A. Pesin and L. Balents. Mott physics and band topology in materials with strong spin-orbit interaction. *Nat. Phys.*, 6:376, 2010.
- [40] F. Wang and T. Senthil. Twisted Hubbard Model for Sr_2IrO_4 : Magnetism and Possible High Temperature Superconductivity. *Phys. Rev. Lett.*, 106:136402, 2011.
- [41] S. E. Barnes S. Ishihara W Koshibae G. Khaliullin S. Maekawa, T. Tohyama. *Physics of Transition Metal Oxides*, Springer Berlin Heidelberg, 2010.
- [42] K. Lefmann. Neutron Scattering: Theory, Instrumentation, and Simulation. *University of Copenhagen*, 2012.
- [43] A. Kitaev. Anyons in an exactly solved model and beyond. *Ann. Phys.*, 321:2, 2006.
- [44] S. McCall J. E. Crow G. Cao, J. Bolivar and R. P. Guertin. Weak ferromagnetism, metal-to-nonmetal transition, and negative differential resistivity in single-crystal Sr_2IrO_4 . *Phys. Rev. B*, 57:R11039, 1998.
- [45] T. Komesu S. Sakai T. Morita H. Takagi B. J. Kim, H. Ohsumi and T. Arima. Phase-sensitive observation of a spin-orbital Mott state in Sr_2IrO_4 . *Science*, 323:1329, 2009.
- [46] S. Boseggia L. Simonelli A. Al-Zein J. G. Vale-L. Paolasini E. C. Hunter R. S. Perry D. Prabhakaran A. T. Boothroyd M. Krisch-G. Monaco H. M. Ronnow D. F. McMorrow M. Moretti Sala, V. Schnells and F. Mila. Evidence of quantum dimer excitations in $\text{Sr}_3\text{Ir}_2\text{O}_7$. *Phys. Rev. B*, 92:024405, 2015.
- [47] Y. Doi and Y. Hinatsu. The structural and magnetic characterization of 6H-perovskite-type oxides $\text{Ba}_3\text{LnIr}_2\text{O}_9$ (Ln = Y, lanthanides). *J. Phys.: Condens. Matter*, 16:2849, 2004.
- [48] T. Dey, S. K. Panda, A. V. Mahajan, I. Dasgupta, B. Koteswararao, F. C. Chou, A. A. Omrani, and H. M. Ronnow. Realization of a spin-liquid ground state in the high-pressure phase of $\text{Ba}_3\text{YIr}_2\text{O}_9$. *arXiv*, page 1210.4355v1, 2012.
- [49] D. I. Khomskii. *Transition Metal Compounds*. Cambridge University Press, Cambridge, 2014.
- [50] D. V. Efremov O. Kataeva S. Gass-C. G. F. Blum-F. Steckel D. Gruner T. Ritschel A. U. B. Wolter J. Geck C. Hess K. Koepf J. van den Brink S. Wurmehl T. Dey, A. Maljuk and B. Buchner. Ba_2YIrO_6 : A cubic double perovskite material with Ir^{5+} ions. *Phys. Rev. B*, 93:014434, 2016.
- [51] G. Cao, T. Qi, L. Li, J. Terzic, S. Yuan, L. DeLong, G. Murthy, and R. Kaul. Novel Magnetism of Ir^{5+} ($5d^4$) Ions in the Double Perovskite Sr_2YIrO_6 . *Phys. Rev. Lett.*, 112:056402, 2014.

- [52] K. Watanabe. An approach to the growth of $\text{YBa}_2\text{Cu}_3\text{O}_{7-x}$ single crystals by the flux method. *Journal of Crystal Growth*, 100:293, 1990.
- [53] P. F. S. Rosa E. M. Bittar L. Bufaical R. L. de Almeida E. Granado T. Grant Z. Fisk M. A. Avila R. A. Ribeiro P. L. Kuhns A. P. Reyes R. R. Urbano T. M. Garitezi, C. Adriano and P. G. Pagliuso. Synthesis and Characterization of BaFe_2As_2 Single Crystals Grown by In-flux Technique. *Braz J. Phys*, 43:223, 2013.
- [54] L. Li J. Terzic V. S. Cao S. J. Yuan M. Tovar G. Murthy G. Cao, T. F. Qi and R. K. Kaul. Evolution of magnetism in the single-crystal honeycomb iridates $(\text{Na}_{1-x}\text{Li}_x)_2\text{IrO}_3$, pages = 220414R, volume = 88, year = 2013. *Phys. Rev. B*.
- [55] L. Zhang Y. B. Chen J. Zhou S. T. Zhang Z. B. Gu S. H. Yao Y. F. Chen S. T. Dong, B. B Zhang. Growth, structure and physical properties of gadolinium doped Sr_2IrO_4 single crystal. *Journal of Crystal Growth*, 378-37:2777, 2014.
- [56] W. L. Bragg. The Structure of Some Crystals as Indicated by Their Diffraction of X-rays. *Proc. R. Soc. London, Sec. A*, 89:246, 1913.
- [57] A. M. M. Schreurs A. J. M. Duisenberg, L. M. J. Kroon-Batenburg. An intensity evaluation method: EVAL-14. *J. Appl. Crystallogr.*, 36:220, 2003.
- [58] R. H. Blessing. An empirical correction for absorption anisotropy. *Acta Cryst.*, A51:33, 1995.
- [59] G. M. Sheldrick. A short history of SHELX. *Acta Cryst.*, A64:112, 2008.
- [60] K. H. Butrouna. A Systematic Transport and Thermodynamic Study of Heavy Transition Metal Oxides with Hexagonal Structure. *PhD thesis*, University of Kentucky, 2014.
- [61] M. Geoghegan and G. Hadziioannou. Polymer Electronics. *Oxford Master Series in Physics*, 2013.
- [62] Y. Singh. Electrical resistivity measurements: a review. *Int. J. Mod. Phys: Conf. Ser.*, 22: 745, 2013.
- [63] S. O. Kasap. Thermoelectric Effects in Metals: Thermocouples. *Web-Material*, 2001.
- [64] J. S. Schilling A. Eiling. Pressure and temperature dependence of electrical resistivity of Pb and Sn from 1-300K and 0-10 GPa-use as continuous resistive pressure monitor accurate over wide temperature range; superconductivity under pressure in Pb, Sn and In. *J. Phys. F: Met. Phys.*, 623:11, 1981.
- [65] J. Wittig B. Bireckoven. A diamond anvil cell for the investigation of superconductivity under pressures of up to 50 GPa: Pb as a low temperature manometer. *J. Phys. E: Sci. Instrum.*, 21:841, 1988.

Bibliography

- [66] M. McElfresh. Fundamentals of magnetism and magnetic measurements featuring Quantum Design's magnetic property measurement system. *Quantum Design*, 1994.
- [67] M. Mihalik M. Mihalik-A. Zentko J. Kamarad Z. Mitroova S. Matas M. Zentkova, Z. Arnold. Magnetic measurement under pressure. *Journal of ELECTRICAL ENGINEERING*, 57(8/S): 29, 2006.
- [68] Z. Machatova J. Kamarad and Z. Arnold. High pressure cells for magnetic measurements- Destruction and functional tests. *Rev. Sci. Instrum.*, 75:5022, 2004.
- [69] L. Yang, A. Pisoni, A. Magrez, S. Katrych, A. Arakcheeva, B. Dalla Piazza, K. Prsa, J. Jacimovic, A. Akrap, J. Teyssier, L. Forro, and H. M. Ronnow. Crystal Structure, Transport, and Magnetic Properties of an Ir⁶⁺ Compound Ba₈Al₂IrO₁₄. *Inorg. Chem.*, 54(9):4371–4376, 2015.
- [70] L. Yang, M. Jeong, A. Arakcheeva, I. Zivkovic, B. Nafradi, A. Magrez, A. Pisoni, J. Jacimovic, V. M. Katukuri, S. Katrych, N. E. Shaik, O. V. Yazyev, L. Forro, and H. M. Ronnow. Possibility of an unconventional spin state of Ir⁴⁺ in Ba₂₁Ir₉O₄₃ single crystal. *Phys. Rev. B*, 94:104403, 2016.
- [71] D. Y. Jung, G. Demazeau, J. Etourneau, and M. A. Subramanian. Preparation and characterization of new perovskites containing Ir(VI) and Ir(V) [BaM_{0.50}Ir_{0.50}O_{2.75} and BaM_{0.25}Ir_{0.75}O₃ (M = Li or Na)]. *Mater. Res. Bull.*, 30:113, 1995.
- [72] D. Y. Jung, P. Gravereau, and G. Demazeau. Stabilization of six-coordinated iridium(VI) in a perovskite oxygen lattice Ba₂MIrO₆ (M=Ca, Sr). *Eur. J. Solid State Inorg. Chem.*, 30: 1025, 1993.
- [73] G. Demazeau, D. Y. Jung, J. P. Sanchez, E. Colineau, A. Blaise, and L. Fournes. Iridium(VI) stabilized in a perovskite-type lattice: Ba₂CaIrO₆. *Solid State Commun.*, 85:479, 1993.
- [74] J. H. Choy, D. K. Kim, S. H. Hwang, G. Demazeau, and D. Y. Jung. XANES and EXAFS Studies on the Ir-O Bond Covalency in Ionic Iridium Perovskites. *J. Am. Chem. Soc.*, 117: 8557, 1995.
- [75] J. Park, J. G. Park, I. P. Swainson, H. C. Ri, Y. N. Choi, C. Lee, and D. Y. Jung. Neutron diffraction studies of Ba₂CaIr(VI)O₆. *J. Korean Phys. Soc.*, 41:118, 2002.
- [76] W. S. Yoon H. C. Loye S. J. Mugavero, M. D. Smith. Nd₂K₂IrO₇ and Sm₂K₂IrO₇: Iridium(VI) Oxides Prepared under Ambient Pressure. *Angew. Chem. Int. Ed Engl.*, 48:215, 2009.
- [77] L. Stenberg. Structure of Sr₈Si₂PtO₁₄. *Acta Cryst. C*, 44:955, 1988.

- [78] Y. S. Lee F. C. Chou, J. H. Cho. Magnetic susceptibility study of hydrated and nonhydrated $\text{Na}_x\text{CoO}_2 \cdot y\text{H}_2\text{O}$ single crystals. *Phys. Rev. B*, 70:144526, 2004.
- [79] P. W. Stephens R. J. Cava M. Bremholm, S. E. Dutton. NaIrO_3 — A pentavalent post-perovskite. *J. Solid State Chem.*, 184:601, 2011.
- [80] H. Tonomura T. Tayama T. Sakakibara J. van Duijn C. Broholm Y. J. Maeno Y. Machida, S. Nakatsuji. Crystalline electric field levels and magnetic properties of the metallic pyrochlore compound $\text{Pr}_2\text{Ir}_2\text{O}_7$. *Phys. Chem. Solids*, 66:1435, 2005.
- [81] K. Miyake H. Matsuura. Effect of Spin–Orbit Interaction on $(4d)^3$ - and $(5d)^3$ -Based Transition-Metal Oxides. *J. Phys. Soc. Jpn.*, 82:073703, 2013.
- [82] R. Boca. Magnetic Parameters and Magnetic Functions in Mononuclear Complexes Beyond the Spin-Hamiltonian Formalism. *Struct Bond*, 117:1, 2005.
- [83] Y. B. Kim W. Witczak-Krempa, G. Chen and L. Balents. Correlated Quantum Phenomena in the Strong Spin-Orbit Regime. *Annu. Rev. Condens. Matter Phys.*, 5:57, 2014.
- [84] E. K.-H. Lee J. G. Rau and H.-Y. Kee. Spin-Orbit Physics Giving Rise to Novel Phases in Correlated Systems: Iridates and Related Materials. *Annu. Rev. Condens. Matter Phys.*, 7:195, 2016.
- [85] L. Siurakshina J. van den Brink L. Hozoi V. M. Katukuri, V. Yushankhai and I. Rousochatzakis. Mechanism of Basal-Plane Antiferromagnetism in the Spin-Orbit Driven Iridate Ba_2IrO_4 . *Phys. Rev. X*, 4:021051, 2014.
- [86] H. C. Walker R. Springell Z. Feng E. C. Hunter R. S. Perry D. Prabhakaran A. T. Boothroyd S. P. Collins H. M. Ronnow J. G. Vale, S. Boseggia and D. F. McMorrow. Importance of XY anisotropy in Sr_2IrO_4 revealed by magnetic critical scattering experiments. *Phys. Rev. B*, 92:020406(R), 2015.
- [87] J. Vale R. Springell Z. Feng R. S. Perry M. Moretti Sala H. M. Ronnow S. P. Collins S. Boseggia, H. C. Walker and D. F. McMorrow. Locking of iridium magnetic moments to the correlated rotation of oxygen octahedra in Sr_2IrO_4 revealed by x-ray resonant scattering. *J. Phys. Condens. Matter*, 25:422202, 2013.
- [88] P. Gegenwart and S. Trebst. Spin–orbit physics: Kitaev matter. *Nature Phys.*, 11:444, 2015.
- [89] T. H. Arima J. J. Ishikawa S. Nakatsuji H. Takagi M. Yoshida J. Mizuki D. Uematsu, H. Sagayama and K. Ishii. Large trigonal-field effect on spin-orbit coupled states in a pyrochlore iridate. *Phys. Rev. B*, 92:094405, 2015.

Bibliography

- [90] J. P. Clancy B.-G. Jeon B. Lee K. H. Kim V. Yushankhai P. Fulde D. Casa T. Gog J. Kim A. H. Said M. H. Upton Y.-J. Kim L. Hozoi, H. Gretarsson and J. van den Brink. Longer-range lattice anisotropy strongly competing with spin-orbit interactions in pyrochlore iridates. *Phys. Rev. B*, 89:115111, 2014.
- [91] P. Merz C. Felser S. Kanungo, B. Yan and M. Jansen. Na_4IrO_4 : Square-Planar Coordination of a Transition Metal in d^5 Configuration due to Weak On-Site Coulomb Interactions. *Angew. Chem.*, 127:5507, 2015.
- [92] G. Oszlányi and A. Sütö. Ab initio structure solution by charge flipping. *Acta Cryst. A*, 60: 134, 2004.
- [93] M. Dušek V. Petříček and L. Palatinus. Crystallographic computing system JANA2006: general features. *Z. Kristallogr.*, 229:345, 2014.
- [94] R. D. Burbank and H. T. Evans. The crystal structure of hexagonal barium titanate. *Acta Cryst.*, 1:330, 1948.
- [95] Z. P. Zhang-H. Frenzel M. Grundmann M. Jenderka, J. Barzola-Quiquia and M. Lorenz. Mott variable-range hopping and weak antilocalization effect in heteroepitaxial Na_2IrO_3 thin films. *Phys. Rev. B*, 88:045111, 2013.
- [96] E. Takayama-Muromachi N. Takeshita H. Okabe, M. Isobe and J. Akimitsu. Carrier doping effect for transport properties of a spin-orbit Mott insulator Ba_2IrO_4 . *Phys. Rev. B*, 88:075137, 2013.
- [97] H. Deniz-D. Preziosi D. Hesse C. Lu, A. Quindeau and M. Alexe. Crossover of conduction mechanism in Sr_2IrO_4 epitaxial thin films. *Appl. Phys. Lett.*, 105:082407, 2014.
- [98] I. A. Campbell. Critical exponents of spin-glass systems. *Phys. Rev. B*, 37:9800, 1988.
- [99] Y. Doi T. Sakamoto and Y. Hinatsu. Crystal structures and magnetic properties of 6H-perovskite-type oxides $\text{Ba}_3\text{M}\text{Ir}_2\text{O}_9$ ($\text{M}=\text{Mg}, \text{Ca}, \text{Sc}, \text{Ti}, \text{Zn}, \text{Sr}, \text{Zr}, \text{Cd}$ and In). *J. Solid State Chem.*, 179:2595, 2006.
- [100] J. van den Brink V. M. Katukuri, H. Stoll and L. Hozoi. Ab initio determination of excitation energies and magnetic couplings in correlated quasi-two-dimensional iridates. *Phys. Rev. B*, 85:220402(R), 2012.
- [101] M. Meven G. Roth A. Gukasov H. Murakawa Y. Tokura D. Szaller S. Bordacs I. Kezsmarki V. K. Guduru L. C. J. M. Peters U. Zeitler J. Romhányi V. Hutanu, A. P. Sazonov and B. Nafradi. Evolution of two-dimensional antiferromagnetism with temperature and magnetic field in multiferroic $\text{Ba}_2\text{CoGe}_2\text{O}_7$. *Phys. Rev. B*, 89:064403, 2014.

-
- [102] Y. S. Oh A. Hogan Y. Horibe K. Kim B. I. Min J. J. Yang, Y. J. Choi and S.-W. Cheong. Charge-Orbital Density Wave and Superconductivity in the Strong Spin-Orbit Coupled IrTe₂: Pd. *Phys. Rev. Lett.*, 108:116402, 2012.
- [103] R. Endoh H. Takano S. Nagata N. Matsumoto, K. Taniguchi. Resistance and Susceptibility Anomalies in IrTe₂ and CuIr₂Te₄. *J. Low Temp. Phys.*, 117-5:1129, 1999.
- [104] M.J. Gutmann S.A. Barnett A. Bombardi S. Artyukhin T. Birol D. Vanderbilt J.J. Yang S.-W. Cheong G.L. Pascut, K. Haule and V. Kiryukhin. Dimerization-Induced Cross-Layer Quasi-Two-Dimensionality in Metallic IrTe₂. *Phys. Rev. Lett.*, 112:086402, 2014.
- [105] H. B. Cao J. Q. Yan D. Mandrus Z. Jiang A. Kiswandhi, J. S. Brooks and H. D. Zhou. Competition between the structural phase transition and superconductivity in Ir_{1-x}Pt_xTe₂ as revealed by pressure effects. *Phys. Rev. B*, 87:121107(R), 2013.
- [106] T. Dong P. Zheng A. F. Fang, G. Xu and N. L. Wang. Structural phase transition in IrTe₂: A combined study of optical spectroscopy and band structure calculations. *Sci. Rep.*, 3: 1153, 2013.
- [107] B. I. Halperin and D. R. Nelson. Resistive transition in superconducting films. *J. Low Temp. Phys.*, 36:599, 1979.
- [108] V. L. Berezinskii. Destruction of long-range order in one-dimensional and two-dimensional systems possessing a continuous symmetry group. II. Quantum systems. *Zh. Eksp. Teor. Fiz.*, 61:1144, 1971.
- [109] J. M. Kosterlitz and D. J. Thouless. Ordering, metastability and phase transitions in two-dimensional systems. *J. Phys. C*, 6:1181, 1973.
- [110] P. Kierkegaard and M. Westerlund. The Crystal Structure of MoOPO₄. *Acta Chem. Scand.*, 18:2217, 1964.
- [111] A. Guesdon M. M. Borel E. Canadell, J. Provost and A. Leclaire. Magnetic Properties and New Structural Classification of Molybdenum Phosphates Containing Mo(V). *Chem. Mater.*, 9:68, 1997.
- [112] G. Villeneuve L. Lezama, K. S. Suh and T. Rojo. Magnetic properties and ³¹P NMR studies of superexchange mechanism in molybdenyl phosphate MoOPO₄. *Solid State Comm.*, 76:449, 1990.
- [113] J. Rodriguez-Carvajal. Magnetic X-ray diffraction from ferromagnets. *Physica B*, 192:55, 1993.

Bibliography

- [114] J. Chardon J. Provost M. Borel, A. Leclaire and B. Raveau. Molybdenum(V) Chloromonophosphates with a Layer Structure: $AMoO(PO_4)Cl$ ($A = K$ and Rb). *J. of Solid State Chem.*, 137:214, 1998.
- [115] H. Ishikawa. (*unpublished*).
- [116] M. Chiba S. Mitsudo T. Idehara T. Tonegawa K. Okamoto T. Sakai T. Kuwai H. Kikuchi, Y. Fujii and H. Ohta. Experimental Observation of the $1/3$ Magnetization Plateau in the Diamond-Chain Compound $Cu_3(CO_3)_2(OH)_2$. *Phys. Rev. Lett.*, 94:227201, 2005.
- [117] T. Kamikawa T. Kunimoto Y. Inagaki H. Kikuchi T. Saito M. Azuma H. Ohta, S. Okubo and M. Takano. High Field ESR Study of the $S=1/2$ Diamond-Chain Substance $Cu_3(CO_3)_2(OH)_2$ up to the Magnetization Plateau Region. *J. Phys. Soc. Jpn.*, 72:2464, 2003.
- [118] F. Bert P. Mendels. Quantum kagome frustrated antiferromagnets: One route to quantum spin liquids. *Comptes Rendus Physique*, 17(3-4):455, 2016.
- [119] H. Effenberger. $Cu_2O(SO_4)$, dolerophanite: Refinement of the crystal structure, with a comparison of $[OCu(II)_4]$ tetrahedra in inorganic compounds. *Monatshefte fur Chemie*, 116:927, 1985.



Acknowledgements

First and foremost, I would like to sincerely thank Prof. László Forró and Prof. Henrik M. Rønnow for providing this precious opportunity for me to do my Ph.D thesis under their supervision at LPMC and LQM. I'd like to thank my thesis supervisor Professor László Forró for his guidance, support and the encouragement to be independent. I express my gratitude to my thesis co-supervisor Professor Henrik M. Rønnow for his encouragement, structural, insightful discussions and suggestions on my Ph.D work. I am very grateful for his patience and all the time he spend on correcting and improving my papers.

Then, I would like to express my thanks to the committee members Prof. Romuald Houdre, Johan Chang, Oleg V. Yazyev and Kazimierz Conder for their valuable comments and suggestions on this thesis.

I appreciate the initial help from Dr. Arnaud Magrez when I started working on the sample growth. I would like to acknowledge Johan Chang since working with him is really encouraging and enjoyable. I'd like to thank my former colleague Dr. Andrea Pisoni and Jacim Jacimovic when I started working in transport lab, they provided me endless help and shared their comprehensive knowledge with me on my confusions. My special thanks go to Dr. Minki Jeong because his outstanding determination and hard work were always example to me. Many thanks to Helmuth Berger for all the high-quality single crystals that he always provided me. I am very thankful to Dr. Alla Arakcheeva and Sergiy Katrych for their help on crystal structure refinement and from whom I have learned the spirit of being helpful and sharing with others. I am also very thankful to Dr. Ivica Zivkovic for his time on correcting my paper, thesis and sharing the knowledge of different experimental techniques.

Of course, Iness and Ping cannot be missed in this list because they are the person who I have shared unforgettable moments with and provides with endless help during these years.

Acknowledgements

Thanks other colleagues at LPMC and LQM for the happy moments spent together, such as BBQs, party on the weekend, etc..

Last but not the least, I gratefully thank my parents for their continuous love and support.

Lausanne, 8 November 2016

Lin Yang

Personal information

| | |
|----------------|------------------------------|
| Name | Lin Yang |
| Date of birth | April 4 th , 1985 |
| Place of birth | Tianjin, China |
| Nationality | Chinese |

Education

| | |
|-----------|---|
| 2013–2016 | Ph.D in Physics, Laboratory of Physics of Complex Matter and Laboratory for Quantum Magnetism, Swiss Federal Institute of Technology Lausanne (EPFL), Switzerland |
| 2009-2012 | Master in Condensed Matter Physics, Zhejiang University (ZJU), China |
| 2003-2007 | Bachelor in Physical Science and Technology, Central China Normal University (CCNU), China |

Professional experience

| | |
|-----------|--|
| 2013–2016 | Swiss Federal Institute of Technology at Lausanne (EPFL), Laboratory of Physics of Complex Matter and Laboratory for Quantum Magnetism, doctoral assistant, teaching assistant, and laboratory research. |
| 2008–2012 | Zhejiang University (ZJU), China, research assistant and teaching assistant. |

Journal publications

1. F. Sousa, B. Sanavio, A. Saccani, Y. Tang, I. Zucca, T. M. Carney, A. Mastropietro, P. H. Jacob Silva, R. P. Carney, K. Schenk, A. O. Omrani, P. Huang, **L. Yang**, et. al., “Superparamagnetic Nanoparticles as High Efficiency Magnetic Resonance Imaging T_2 Contrast Agent”, *Bioconjugate Chem.* 28 (1), 161–170 (2017).
2. **L. Yang**, M. Jeong, A. Arakcheeva, et. al., “Possibility of an unconventional spin state of Ir^{4+} in $\text{Ba}_{21}\text{Ir}_9\text{O}_{43}$ single crystal”, *Phys. Rev. B* 94, 104403 (2016).
3. **L. Yang**, A. Pisoni, A. Magrez, et. al., “Crystal Structure, Transport, and Magnetic Properties of an Ir^{6+} Compound $\text{Ba}_8\text{Al}_2\text{IrO}_{14}$ ”, *Inorg. Chem.* 54 (9), 4371–4376 (2015).
4. W. B. Jiang, **L. Yang**, C. Y. Guo, et. al., “Crossover from a heavy fermion to intermediate valence state in noncentrosymmetric $\text{Yb}_2\text{Ni}_{12}(\text{P}, \text{As})_7$ ”, *Scientific Reports* 5, 17608 (2015).
5. L. Li, D. Parker, P. Babkevich, **L. Yang**, H. M. Ronnow, and A. S. Sefat, “Superconductivity in semimetallic $\text{Bi}_3\text{O}_2\text{S}_3$ ”, *Phys. Rev. B* 91, 104511 (2015).
6. T. Shang, **L. Yang**, Y. Chen, et. al., “Tunable interplay between $3d$ and $4f$ electrons in Co-doped iron pnictides”, *Phys. Rev. B* 87, 075148 (2013).

7. J. Chen, L. Jiao, J. L. Zhang, Y. Chen, **L. Yang**, M. Nicklas, F. Steglich, and H. Q. Yuan, “BCS-like superconductivity in the noncentrosymmetric compounds $\text{Nb}_x\text{Re}_{1-x}$ ($0.13 \leq x \leq 0.38$)”, *Physical Review B*, 88-14, 144510 (2013).
8. J. Chen, L. Jiao, J. L. Zhang, Y. Chen, **L. Yang**, M. Nicklas, F. Steglich, and H. Q. Yuan, “Evidence for two-gap superconductivity in the non-centrosymmetric compound LaNiC_2 ”, *New Journal of Physics*, 15-5, 053005 (2013).
9. J. Chen, L. Jiao, J. L. Zhang, Y. Chen, **L. Yang**, and H. Q. Yuan, “A study of London penetration depth for the non-centrosymmetric superconductor LaNiC_2 ”, *Journal of the Korean Physical Society*, 63-3, 463 (2013).
10. L. Jiao, Z. F. Weng, X. Y. Tang, L. K. Guo, T. Shang, **L. Yang**, H. Q. Yuan, Y. Y. Wu, and Z. C. Xia, “Anisotropic in-plane resistivity and magnetoresistance of the detwinned BaFe_2As_2 ”, *Journal of the Korean Physical Society*, 63-3, 453 (2013).
11. J. L. Zhang, Y. Chen, L. Jiao, R. Gumenuik, M. Nicklas, Y. H. Chen, **L. Yang**, et. al., “Multiband superconductivity in $\text{PrPt}_4\text{Ge}_{12}$ single crystals”, *Physical Review B*, 87-6, 064502 (2013).

Pending papers

1. **L. Yang**, M. Jeong, P. Babkevich, et. al., “Orbitally quenched $S = 1/2$ magnetic insulator MoPO_5 ”, submit to *Physical Review B* soon.
2. **L. Yang**, Y. Chen, J. Chang, et. al., “Pressure induced two-dimensional superconductivity and Ir-dimerization in $\text{Ir}_{0.95}\text{Pt}_{0.05}\text{Te}_2$ ”.
3. **L. Yang**, I. Živković, H. Berger, A. Magrez, L. Forro and H. M. Rønnow et.al, “Low dimensional magnetism of Kagome Like Substance Cu_2OSO_4 ”.
4. **L. Yang**, M. Jeong, A. Magrez, L. Forro and H. Rønnow, “Low dimensional magnetism of spin dimer compounds $\text{Cu}_2\text{P}_2\text{O}_7$ and $\text{Cu}_3\text{P}_2\text{O}_8$ ”.

Conference abstract

1. **Lin Yang**, “Pressure induced two-dimensional superconductivity and Ir-dimerization in $\text{Ir}_{0.95}\text{Pt}_{0.05}\text{Te}_2$ ”, MaNEP Workshop on Topological Quantum Phenomena, University of Zurich, Zurich, Switzerland, November 2016.

Posters

1. **Lin Yang**, “Transport and magnetic properties of a triangular-lattice $\text{Ba}_{21}\text{Ir}_9\text{O}_{43}$ single crystal”, Swiss Workshop on Material with Novel Electronic Properties, Les Diablerets, Switzerland, July 2016.
2. **Lin Yang**, “Synthesis, transport and magnetic properties of a new Ir-based compound $\text{Ba}_8\text{Al}_2\text{IrO}_{14}$ ”, Swiss Workshop on Material with Novel Electronic Properties, Les Diablerets, Switzerland, June 2013.

